Technology
Innovation
Institute

GlobalEM 2022

Abstract Book

Global Electromagnetics Conference
The St Regis Abu Dhabi
13th - 17th November 2022

tii.ae

High-Power Fiber Laser-Induced Damage on the Surface of a Quadcopter Drone

Reem Al Ameri, Antaryami Mohanta, Taif Alhmoudi, Guillaume Matras and Chaouki Kasmi
Directed Energy Research Center, Technology Innovation Institute,
Abu Dhabi, United Arab Emirates
Reem.AlAmeri@tii.ae

Abstract— Unmanned Aerial vehicles (UAVs), also known as drones, have been misused by unauthorized groups such as drug dealers. Therefore, many methods including the use of high-power lasers have been proposed to neutralize or damage the drones. In this study, several experiments were performed on the surface of a quadcopter drone using a high-power fiber laser. The laser power was fixed at 900 W, the laser irradiation time was 5 s and the distance between the laser head and the quadcopter drone was 4.4 m. Three different laser beam diameters such as 0.60, 0.74, and 1.02 cm were used in the experiment. The results have shown that the smallest beam diameter can lead to faster penetration through the surface of the drone in 0.375 s.

Keywords- Laser-material interaction, High-speed imaging, UAV, Drone

I. INTRODUCTION

Directed energy systems comprised of high-power lasers, microwave sources, or particle beams have been considered as potential weapon systems to neutralize or damage commercial UAVs/drones involved in malicious activities [1]. In such directed energy systems, focused electromagnetic energy or atomic or subatomic particles beam has been employed for degradation, damage, or complete destruction of the targets [2]. In this research, the effect of the interaction of a high-power fiber laser with the surface of a quadcopter drone is studied. An appropriate selection of laser parameters could result in efficient damage to drones, which requires a deep insight into the laser-material interaction process. An in-depth understanding of the thermal damage process caused by a high-power laser on the mechanical structure of a drone, which holds and protects the electronics, could help in identifying the laser parameters needed to disrupt the desired performance of the drone. Three experiments have been conducted to understand the high-power laser effect on the surface of a static quadcopter drone.

II. EXPERIMENT

A. Experiment Setup

A Continuous Wave (CW) fiber laser having a maximum power of 6 kW, and wavelength of 1080 nm was used to investigate its interaction with the surface of a quadcopter drone. The laser head was placed at 4.4 m from the body surface of the drone, which has an average thickness of 2 mm. The laser power and irradiation time were fixed at 900 W and 5 s, respectively. Three laser beam diameters were used, which are 0.60, 0.74, and 1.02 cm. A high-speed camera with an 850 nm band pass filter was used to capture the images from the laser-material interaction zone.

B. Experimental Results

Fig.1 shows the laser-irradiated surface of the drone at different laser beam diameters for a fixed laser power of 900 W. The decrease in laser beam diameter increases the power density, which results in increasing damage to the drone. High-speed camera images were used to determine the damage time, which is found to be the shortest, i.e., 0.375 s for the smallest beam diameter of 0.60 cm.

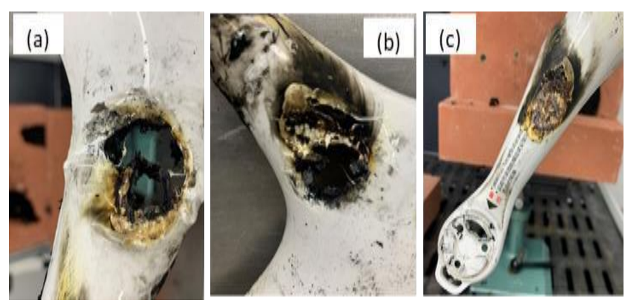

Figure 1. The drone surface after laser irradiation for a beam diameter and power density of (a) 0.60 cm and 3.18×10^3 W/cm^2 (b) 0.74 cm and 2.10×10^3 W/cm^2 (c) 1.02 cm and 1.10×10^3 W/cm^2, respectively.

REFERENCES

[1] J. L. Esteves, E. Cottais, and C. Kasmi, “Unlocking the Access to the Effects Induced by IEMI on a Civilian UAV,” *2018 International Symposium on Electromagnetic Compatibility (EMC EUROPE),* pp.48-52, Aug. 2018.

[2] Y. X. Zhang, Z. Zhu, R. Joseph, and I. J. Shihan, “Damage to aircraft composite structures caused by directed energy system: A literature review,” Defense Technology, vol. 17, pp. 1269-1288, Aug 2021.

Real-time Substation Shielding Compromise and HPEM Event detection

Eric Easton[1], Ph.D., P.E., Cyril Wafo[1], P.E., Richard Hoad[2], Ph.D. and Tim Rees[2]

[1] CenterPoint Energy
Houston, TX, United States
Eric.Easton@CenterPointEnergy.com
Cyril.Wafo@CenterPointEnergy.com

[2] QinetiQ Ltd.
Cody Technology Park
Farnborough, Hants, UK
rhoad@qinetiq.com

***Abstract*—**CenterPoint Energy completed an effective, cost-efficient solution for High-Power Electromagnetic (EM) mitigation [1] to be used in electric substations. The EM module design exceeds the shielding effectiveness test levels of MIL-188-125-1. Following the development of the EM mitigation module, efforts focused on real-time shielding compromise and event detection for EM threats. For threats, the HEMP/IEMI detector uses magnitude and frequency to determine the need and appropriate level of alert. Additionally, shielding compromise is evaluated using a differential measurement from an on-board tone generator. The detector allows for real-time detection and alerts, reduces the need for technician field visits by regularly testing for shielding compromise, as well as provides forensic data for post-event analysis.

I. INTRODUCTION

Based on a system-wide deployment strategy and an annual shielding effectiveness test per location, costs of an on-site IEEE std 299.1 testing program was determined cost and logistically prohibitive. The use of a once annual testing program may also leave extended time periods of ineffective shielding, diminishing EMP resiliency. Alternatively, EMP response and resiliency would be greatly improved by the situational awareness gained from event detection. For localized IEMI events, security and operational personnel can use alerts to initiate response plans for specific substations. In the event of wide-area HEMP effects, the detection would signal control room staff to initiate an appropriately scaled response. In order to meet all operational requirements, the device had to be capable of detecting external EM threats and compromised shielding, transmitting real-time alerts as well as capturing EMC waveform data. The development of a multi-function detection and alert solution was achieved in 2019 and has been successfully deployed in field applications.

II. DESIGN BASIS

QinetiQ Ltd. Were engaged by CenterPoint Energy to adapt their Totem® detector [2] to the dual purposes of HPEM event detection and the additional feature of Shielding compromise detection. The event detection aspect was already fully operational but the shielding compromise part created new design challenges. Given cyber, security and spectrum licensing considerations, the team opted to consider a conducted shielding compromise test method over a radiated test method. A prototype was built and demonstrated and found to be capable of detecting uncontrolled apertures (door ajar) and cable penetration shield violations.

III. OPERATIONAL DEPLOYMENT

Prior to substation deployment, testing was completed on a mock enclosure to ensure the differential method would meet all operational requirements. It was critical the tone generator did not disrupt substation protection and control equipment while testing was in progress. Testing proved the low-order signals used for testing were safe for both equipment inside and outside the EMP mitigation module with no anomalous events detected.

Figure 1. EM Module with Detector Installed

REFERENCES

[1] E. Easton, K. Bryant and W. Radasky, “Design Approach for HPEM Mitigation for Electrical Substations,” in press for APEMC 2020, Sydney Australia, May 2020.

[2] R. Hoad and D. Herke, ‘Electromagnetic Interference Indicator and Related Method’, Patent Application, International Publication Number: WO 2017/125465 A1, International Publication Date: 27th July 2017

Financial Comparative Analysis of Substation EMP Mitigation Approaches

Eric Easton, Ph.D., P.E.
Real-Time Operations
CenterPoint Energy
Houston, TX, United States
Eric.Easton@CenterPointEnergy.com

Cyril Wafo, P.E.
High Voltage Planning & Support
CenterPoint Energy
Houston, TX, United States
Cyril.Wafo@CenterPointEnergy.com

***Abstract*—The effective mitigation of high-level fields from EMPs requires mitigation of both radiated and conducted energy. Cost concerns are always central to the mitigation debate. This paper examines the financial costs of achieving various levels of shielding effectiveness (SE) from a range of implementation methods as compared to a module-based design [1]; using quantitative methods for costs and qualitative methods for mitigation effectiveness.

I. Mitigating EMP effects in power substations

The environments considered in this paper are HEMP (100 MHz to 1 GHz) and IEMI (up to 10 GHz). Radiated fields should be addressed using hardened enclosures, shielded control cables and addressing POEs. Conducted energy should be mitigated with surge suppression devices as well as high frequency grounding and bonding. Device power protection is accomplished with HEMP filtering. Below is an evaluation framework for assessing effectiveness versus costs in mitigation decisions.

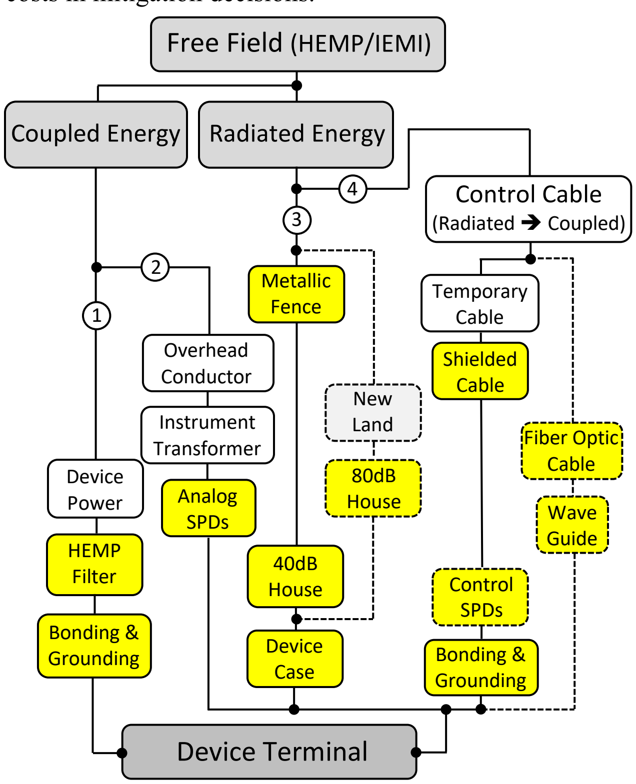

Figure 1: HEMP/IEMI Protection Diagram

II. HEMP/IEMI Protection Alternativities

Figure 1 represents four paths of mitigation including (1) device power, (2) overhead power conductor coupling, (3) direct radiation and (4) coupled energy resulting from radiated fields on metallic control cable. Based on Figure 1, ten configurations were identified for comparison to the module design. Initial implementation costs range from $0.5 M to $2.5M. Figure 2 represents the initial installation costs and qualitative assessment of mitigation effectiveness.

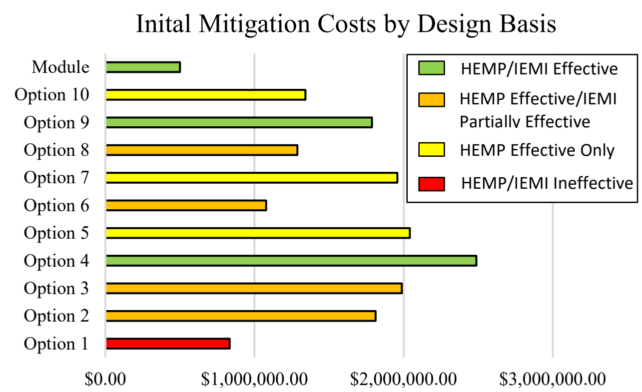

Figure 2: Quantitative Costs/Qualitative SE

Life-cycle costs associated with maintenance and inspection for SE were also considered. Maintenance associated with SPDs is assumed to be proportional to the number of SPDs installed. Door maintenance costs would be based on expected open/close cycles and SE testing costs proportional to enclosure size. Assumptions included an SPD failure rate of 1%, annual SE testing and a 20-year asset life.

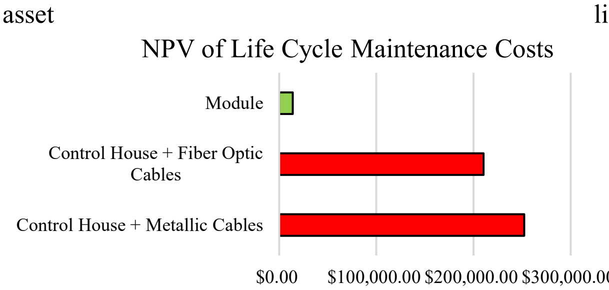

Figure 3: Maintenance Cost Comparison

[1] E. Easton, K. Bryant and W. Radasky, "Design Approach for HPEM Mitigation for Electrical Substations," in press for APEMC 2020, Sydney Australia, May 2020.

FDTD Simulation of Voltages Induced on Secondary Circuits in a Substation with a Grounding Grid

Akiyoshi Tatematsu
Electric Facility Technology Division
Central Research Institute of Electric Power Industry
Yokosuka, Kanagawa, Japan
akiyoshi@criepi.denken.or.jp

Akifumi Yamanaka
Electric Facility Technology Division
Central Research Institute of Electric Power Industry
Yokosuka, Kanagawa, Japan
yamanaka3929@criepi.denken.or.jp

Abstract—Voltages are induced on a secondary circuit in a substation owing to lightning impulse currents flowing into the grounding structure of a substation. The induced voltages may cause faults and malfunctions of sensitive electronic devices, and thus, to protect secondary circuits from lightning overvoltage, shielded control cables are employed. In this study, we simulate a test platform of primary and secondary circuits with an unshielded or shielded control cable in a substation using an electromagnetic transient analysis code developed on the basis of the hybrid technique of the three-dimensional finite-difference time-domain method and transmission-line theory. Then, we calculate voltages induced on the control cable when lightning impulse currents flow into a grounding grid, and compare the calculated results with measured waveforms for validation.

Keywords-FDTD method, lightning, secondary circuits, shielded control cable, substation

I. INTRODUCTION

When lightning strikes a substation and transmission line, lightning impulse currents flow into the grounding structure of the substation through lightning surge arresters, shield wires, and so forth. Then, voltages are induced on the secondary circuits in the substation owing to the effect of the ground potential rises of the grounding structure and electromagnetic coupling, which may cause malfunctions and faults of electronic devices in the secondary circuits. As countermeasures against lightning overvoltage, shielded control cables are installed in the secondary circuits, and thus, it is useful to evaluate the effectiveness of shielded control cables through simulations. In this study, using the hybrid technique of the finite-difference time-domain (FDTD) method [1] and transmission-line (TL) theory, we calculated voltages induced on a control cable in a test platform of primary and secondary circuits in a substation, and we compared the calculated results with measured waveforms for validation.

II. SIMULATED AND MEASURED RESULTS

Fig. 1 shows the test platform of primary and secondary circuits in a substation, which was mainly composed of a grounding grid, a gas-insulated switchgear (GIS) model comprising a gas-insulated bus model and voltage and current transformers (VT and CT), and a protection-relay unit. Here, the signal-output terminal of the CT was connected to the protection-relay unit via an unshielded or shielded control cable. In the case of the shielded control cable, the shield of the cable was grounded at both ends. Injecting a lightning impulse current into the grounding grid with a pulse generator placed near the grounding grid, we measured voltages induced on the control cable at the protection-relay unit (point A in Fig. 1). In the simulations, we modeled the grounding grid, gas-insulated bus model, shield of the control cable, and pulse generator by the three-dimensional FDTD method, whereas electromagnetic transient phenomena in the control cables were solved on the basis of the one-dimensional TL theory taking into account the effect of the surface transfer impedance of the shield of the control cable [2]. As shown in Fig. 2, we confirmed that the calculated induced voltages agree well with the measured waveforms. The hybrid technique is useful for evaluating the effectiveness of shielded control cables to suppress induced voltages.

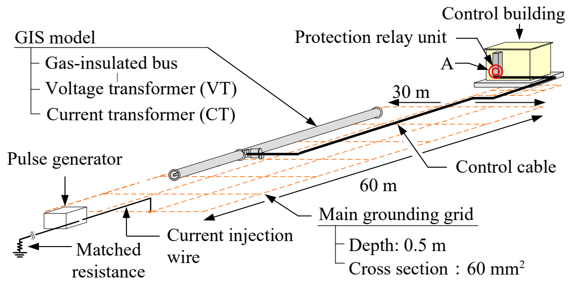

Fig. 1 Experimental setup of a test platform of primary and secondary circuits.

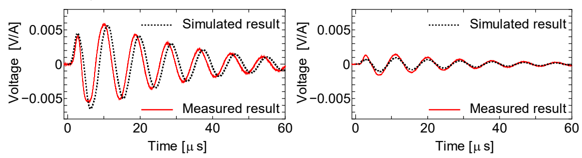

(a) Unshielded control cable (b) Shielded control cable

Fig. 2 Simulated and measured induced voltages at point A.

REFERENCES

[1] K. S. Yee, "Numerical solution of initial boundary value problems involving Maxwell's equations in isotropic media," IEEE Trans. Antennas and Propagation, vol. AP 14, no. 3, pp. 302–307, May 1966.

[2] E. F. Vance, Coupling to Shielded Cables. Hoboken, NJ, USA: Wiley, 1978.

High-Power Laser Diode Beam Shaping for Incoherent Combining

Juan Coronel, Giuseppe Scurria, Amit Dubey, Abdellatif Bouchalkha,
Layla Al Shehhi, Guillaume Matras, Asma Al Ahmadi, Reem Al Ameri, Chaouki Kasmi
Directed Energy Research Center
Technology Innovation Institute
Abu Dhabi, United Arab Emirates
juan.coronel@tii.ae

Abstract—This abstract presents the simulation and experimental approach and results of the beam shaping and incoherent beam combining of two kW-order laser sources using incoherent polarization combining at infrared wavelengths.

Keywords: Beam shaping; incoherent combining; high-power laser.

I. INTRODUCTION

The development of more compact laser sources for high-power applications have brought the possibility to replace in near future high-brightness laser sources for material cutting or processing.

Currently, the most widely used laser technologies for high-brightness industrial applications are disk, fiber, and CO2 lasers [1]. However, the availability of high-power commercial semiconductor laser diodes opens an opportunity to research on the development of bright laser sources based on beam combining at kW level [2], [3].

In this work, we are presenting the latest results from our team about the implementation of a kW incoherent laser diode stack beam combining. In section two of this abstract more details about the design are provided.

II. HIGH-POWER BEAM COMBINING

The incoherent beam combining implementation proposed in this work is depicted in Fig. 1. The laser sources used are laser diode stacks of ten laser diode bars emitting at 980 nm and having 110 W maximum optical power emission per bar. The laser diode bars are fast-axis collimated using micro lenses. For slow-axis collimation, commercial cylindrical lenses are used to obtain a rectangular emission shape.

Two 1-kW laser diode stacks are placed in orthogonal position one to the other. The beam combining is done thanks to the use of a polarization coated mirror. In front of one of the laser diode stacks (Laser Source 2), we placed a half wave plate to change the beam polarization, then, this beam is reflected by the polarization mirror.

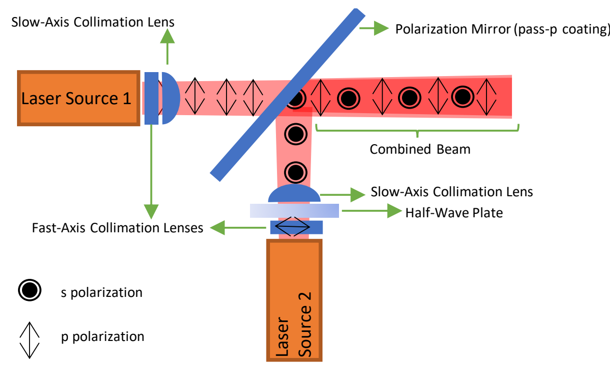

Figure 1. Schematic setup of the polarization-based beam combining (top view).

From the simulation results, it is feasible to implement the polarization-based incoherent beam combining with a power efficiency of 99%. However, in laboratory implementation, the efficiency can drop significantly considering aspects such as the smile effect of the diodes and thermal stress on the lenses. This is going to be explored during the experimental stage of this work and shared during the conference.

REFERENCES

[1] U. Witte *et al.*, “kW-class direct diode laser for sheet metal cutting based on commercial pump modules,” *High-power Diode Laser Technology Xv*, pp. 1008608-1008608–13, 2017, doi: 10.1117/12.2252145.

[2] H. Meng *et al.*, “High-brightness spectral beam combining of diode laser array stack in an external cavity,” *Opt Express*, vol. 23, no. 17, pp. 21819–21824, 2015, doi: 10.1364/oe.23.021819.

[3] J. Yu *et al.*, “High brightness beam shaping and fiber coupling of laser-diode bars,” *Appl Optics*, vol. 54, no. 11, p. 3513, 2015, doi: 10.1364/ao.54.003513.

Analysis of Lightning Electromagnetic Field Propagation Over Mountainous Terrain using Simultaneous Records of Current and its Electric Field at 380-km Distance

1st Dongshuai Li*
DTU Space, Kongens Lyngby, Denmark
IAA-CSIC, Granada, Spain
dongshuai@space.dtu.dk

2nd Mohammad Azadifar
HEIG-VD, Yverdon-les-Bains, Switzerland
mohammad.azadifar@epfl.ch

3rd Antonio Sunjerga
EPFL, Lausanne, Switzerland
antonio.sunjerga@epfl.ch

4th Farhad Rachidi
EPFL, Lausanne, Switzerland
farhad.rachidi@epfl.ch

5th Marcos Rubinstein
HEIG-VD, Yverdon-les-Bains, Switzerland
marcos.rubinstein@heig-vd.ch

6th Alejandro Luque
IAA-CSIC, Granada, Spain
aluque@iaa.es

7th Gerhard Diendorfer
ALDIS, Vienna, Austria
g.diendorfer@ove.at

8th Hannes Pichler
ALDIS, Vienna, Austria
h.pichler@ove.at

***Abstract*—A full-wave Finite-Difference-Time-Domain (FDTD) model is developed to evaluate the propagation effects of lightning electromagnetic fields over mountainous terrain in the earth - ionosphere waveguide (EIWG). The obtained results are validated against simultaneous experimental data consisting of lightning currents measured at the Säntis Tower and electric fields measured in Neudorf, Austria, located at a 380 km distance from the tower. The waveform of the lightning-radiated electric field at 380 km includes both a ground wave and a reflected sky wave. The presence of mountainous terrain mainly affects the time delays and amplitudes of the ground wave, while the skywave parts mostly depend on the effect of the ionospheric cold plasma characteristics.**

***Keywords*—FDTD, Mountainous terrain, Säntis Tower, Lightning, Ionosphere**

I. EXPERIMENTAL DATA

In this study, we focus on lightning in the region around the Säntis Tower located in the Swiss Alps. The 124-m Säntis Tower has been instrumented since 2010 and it serves as an experimental station for the direct measurement of lightning currents. We consider the topography between the Säntis Tower and a 380-km distant electric field sensor in Neudorf, Austria based on global digital elevation model version 2 data.

II. FDTD MODELING

Very low frequency (VLF)/low frequency (LF) waves generated by lightning discharges are well known as an efficient tool to probe the localized variation of the ionospheric D region ($60\,\mathrm{km}$ - $90\,\mathrm{km}$) parameters. In order to include the ionospheric characteristics in the D region, the FDTD model includes three fundamental equations including two of Maxwell's equations and a modified Ohm's equation (sometimes called the Langevin equation).

III. RESULTS AND DISCUSSION

Fig. 1 shows two examples of the measured lightning return stroke currents (a,c) of an upward flash obtained at the Säntis Tower and the simultaneously measured electric fields (b,d) at 380-km distance in Neudorf, occurred at 17:26:00 UTC on Sep 25, 2019. It can be seen that, after taking into account the effect of the irregular terrain along the propagation path and the electron density profile in the ionosphere, both the initial peak and overall waveform of the vertical electric fields calculated by using the FDTD model were found to be in good agreement with the measurements obtained from the 380-km sensor in Neudorf for the considered cases. The use of either the electron density profile or the terrain profile is not enough to obtain a complete match between the simulated and the measured waveforms. The presence of the mountainous terrain mainly affects the time delays and amplitudes of the ground wave parts. However, the skywave parts mostly depend on the effect of the ionospheric cold plasma characteristics.

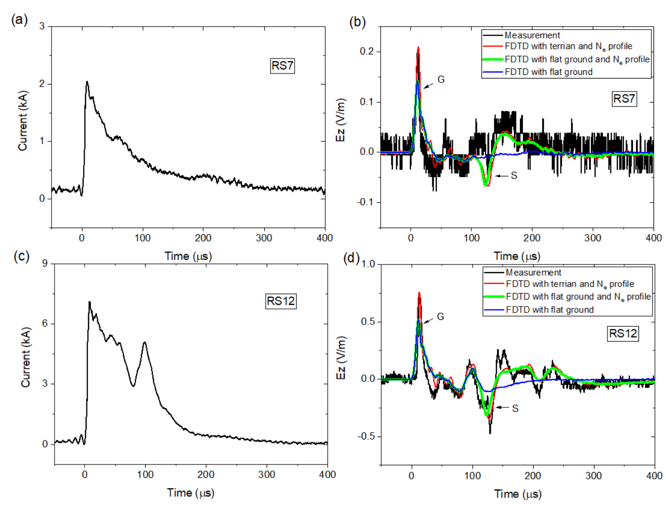

Fig. 1. Two lightning return stroke currents measured at the Säntis Tower (a,c) and the comparison between the E-field observations and the FDTD modeling results at the 380-km Neudorf station (b,d). The ground wave and its reflected sky wave are marked as G and S, respectively.

Ultra-wide band radar system using impulse radiating antennas in The Netherlands

The important contributions of Dr. Dave Giri

Adrianus Petrus Maria (Peter) Zwamborn
Research group Electronic Defence
TNO Defence Safety and Security
The Hague, Zuid-Holland, The Netherlands
Peter.zwamborn@tno.nl

***Abstract*—.**

Beside the books and articles by dr. Dave Giri, his personal involvement to the scientific research programs in the Netherlands in the field of ultra-wide Band high power microwave systems has been paramount. By his expertise, an ultra-wide band radar system was build and this system was used in the field of detection of unexploded ordnance as well as in in high power microwave susceptibility tests. In this contribution these important contributions are reviewed and discussed.

High Power Microwaves, High Power Electromagnetics, Impulse radiating antennas, land mines

I. INTRODUCTION

In the nineties of the last century, the author of this paper was introduced into the field of Nuclear Electromagnetic Pulse Protection (NEMP) and High Power Microwaves (HPM) by the workshops organized by the late dr. Carl Baum. This was the very beginning of the applied scientific engagement with dr. Giri. In the Netherlands, we were running research programs on NEMP and the interest shifted from NEMP to HPM. End of the nineties also a program was started in the field of Humanitarian Demining. At TNO we were enthusiastic about the famous Impulse Radiating Antenna (IRA) and its ability we thought this antenna could help us to investigate the IRA-performance in detecting unexploded ordnance [1] and [2]. We investigated the system and as well as with aid of the Brewster Angle. Dr. Giri was involved to help us design the IRA. This system contained both a transceiver and a receiver IRA. Its specifications were to detect buried objects. Jointly, we wrote a research report on the design and we tested the detection system [1]. During the ISAF mission, we also used the system to detect IEDs.
In the presentation during this special session, the author will highlight the important influence of his scientific talents within the Dutch High Power Microwave research programs, the humanitarian demining program. Dr. Giri's contributions, not only scientifically but also personally. will be highlighted..

REFERENCES

[1] J.B. Rhebergen, A.P.M. Zwamborn and D.V. Giri, “Design of an ultra-wideband ground-penetrating radar system using impulse radiating antennas,” Detection of abandoned land mines”, 12-1 4 October 1998, Conference Publication No. 458.

[2] Lo Vetri, J., Primak, S., van Leersum, B.J.A.M., Zwamborn, A.P.M. (2002). Feasibility Study into the Identification of Landmines Using UWB Radar: An Analysis Using Synthesized Data. In: Heyman, E., Mandelbaum, B., Shiloh, J. (eds) Ultra-Wideband Short-Pulse Electromagnetics 4. Springer, Boston, MA. https://doi.org/10.1007/0-306-47093-4_45

Study on the Effect of HPEM Pulse on RF Front-end

Woosang Lee
1st R&D Institute 2nd Directorate
Agency for Defense Development
Daejeon, Republic of Korea
wslee7@add.re.kr

Jeong Hyeon Kuk, Kang Hyeok Lee, Jin Soo Choi
1st R&D Institute 2nd Directorate
Agency for Defense Development
Daejeon, Republic of Korea

Abstract**—**Direct injection test and high power radiation test are carried out respectively in order to investigate the effect of HPEM pulse on a RF front-end. From the comparison of test results, the correlation between two experimental methodologies can be verified.

Keywords-HPEM, Effect, RF Front-end

I. INTRODUCTION

The RF front-end, composed of an antenna, a filter stage and a low noise amplifier, is one of the vulnerable parts of RF receiving system when it is exposed to high power electromagnetic(HPEM) environment and the threatening electromagnetic signal is induced by the front door coupling. A lot of researches have been reported to investigate the effect on HPEM pulse for RF front-ends from circuit level to system level by using various experimental methodologies [1,2]. When these experiments were planned and designed in detail, common interests might be efficiency and reality for the HPEM effect analysis. In this point of view, we will introduce two different types of HPEM effect tests on RF front-end, direct injection test and high power radiation test will be introduced and the test results will be compared.

II. EFFECT TEST

A. *Direct Injection Test*

The main feature of direct injection test on RF front-end is simplification. In this test setup, the wave propagation from HPEM source to a receiving antenna can be eliminated and the threat signal is induced into RF circuit under test directly. Instead of real high power sources, the solid state power amplifiers(SSPAs) are typically used to generate the simulating HPEM threat signal. When the SSPAs is used in the HPEM effect test, the core advantage is that parameters of electromagnetic signal can be controlled quiet freely in time domain as well as frequency domain due to its wideband characteristics. So, it is possible to simulate a number of HPEM environment cases efficiently using this abbreviated test methodology.

To study the effect of RF front-end in a telecommunication system, one kilowatt in-band SSPA with a signal generator is prepared to generate the equivalent HPEM threat. Then, the input and output signals of every component are monitored while changing parameters of the injected signal such as frequency, power, pulse width, and so on. Figure 1. (a) shows the typical square pulse profile of the injecting signal generated at SSPA and Figure 1. (b) shows the damaged low noise amplifier circuit after direct injection tests.

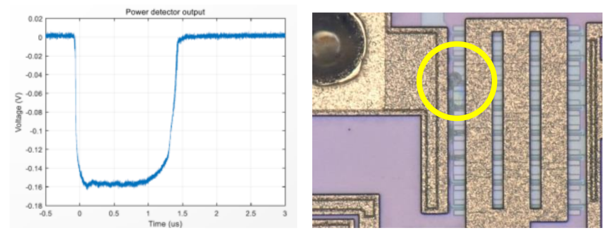

(a) (b)

Figure 1. (a) Injecting HPEM signal, (b) Damage of RF circuit (yellow circle).

B. *High Power Radiation Test*

In spite of efficiency and versatility of direct injection test, the test results should be verified in the real environment conditions. Because it must be a test method with assumption and there are some differences with the real HPEM environment. One of the most unmatched conditions is the injected signal characteristics. Practically, gigawatt class high power sources such as a relativistic vacuum tube generate a specific nonlinear output pulse signal due to pulse shortening, mode competition, frequency shifting, and so on [3]. Therefore, radiation effect tests on the RF front-end including a receiving antenna with a high power source are carried out at outdoor experimental site. In the comparison of the two test results, the correlation between two HPEM effect test methods can be verified.

III. CONCLUSION

In this paper, the direct injection test and the high power radiation test to investigate the HPEM effects via front door coupling were discussed correlatively. Results of the comparison test give us reliability of the experimental method for various types of RF front-end.

REFERENCES

[1] M. G. Backstrom and K. G. Lovstrand, “Susceptibility of electronic systems to high-power microwaves: Summary of test experience,” IEEE Trans. on EMC., vol. 46, no. 3, pp. 396–403, Aug. 2004.
[2] S. M. Hwang and C. S. Huh, “The susceptibility of LNA due to front door coupling under narrow-band high power electro-magnetic wave,” *J IKEEE*, vol. 19, no. 3, pp. 440–446, 2015.
[3] K. Lee, S. Hong, and W. Lee, “Particle-in-Cell Model of a Relativistic Magnetron System driven by a Pulse Forming Network Marx Generator,” Journal of Applied Physics, vol. 131, no. 9, pp. 094901-1~094901-7, March 2022.

Influence of mast positioning on ship RCS in HF band

Nemanja R. Grbić[1,2], *Member*, *IEEE*, Pavle Z. Petrović[1,2], *Member*, *IEEE*, Nikola Lekić[2], *Member*, *IEEE*, Miroslav Perić[2], *Senior Member*, *IEEE*, and Slobodan V. Savić[1], *Member*, *IEEE*
[1]University of Belgrade, School of Electrical Engineering, Belgrade, Serbia
[2]Vlatacom Institute of High Technologies, Belgrade, Serbia
nemanja.grbic@vlatacom.com, pavle.petrovic@vlatacom.com, nikola.lekic@vlatacom.com, miroslav.peric@vlatacom.com, ssavic@etf.bg.ac.rs

Abstract—In this paper effects of the position of a ship's mast on its radar cross section (RCS) are examined in the high frequency (HF) band. Depending on the relative placement of masts it is shown that the monostatic RCS of a ship will change considerably. Hull, command bridge, and other objects will influence the RCS also. Results of electromagnetic simulations indicate that mast placement and bridge positioning allow for an increase or decrease of monostatic RCS for a particular direction.

Keywords – radar cross section (RCS), high frequency over the horizon radars (HF OTHR), mast placement, monopole antenna.

I. INTRODUCTION

Over the horizon radar (OTHR) is a system used for long-range maritime surveillance, which employs the high frequency (HF) surface wave which is vertically polarized [1]. It was shown that in this system a significant contribution to RCS can come from vertical structures such as masts, antennas, and towers [2]. This is even more pronounced when the height of vertical structures is near resonant. With certain arrangements of vertical structures, monostatic radar cross section (RCS) can be canceled in specific directions. In this paper, we will examine some of these effects through numerical simulations.

II. NUMERICAL MODELS AND RESULTS

To investigate the mechanism of RCS cancelation, a simple model of two monopoles separated by λ/4 is simulated (λ being the free space wavelength). Monopoles are placed above an infinite ground plane and illuminated with transverse electromagnetic (TEM) waves traveling in the horizontal plane. The results for monostatic RCS in the horizontal plane are calculated by the WIPL-D Pro [3] and shown in Fig. 1. A clear null in monostatic RCS is seen for directions in the horizontal plane containing the plane of both monopoles, as expected.

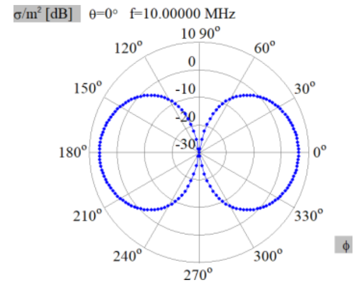

Figure 1. Monostatic RCS of two monopoles separated by λ/4.

On the other hand, for ships with two masts separated by λ/2, there are some effects not present in the previous model. Ships have multiple masts and a command bridge with different electromagnetic surroundings and the ship's hull could not be seen as an infinite ground plane. A simplified realistic model of an oil tanker with two masts and a bridge is presented in the inset of Fig. 2. The ship is illuminated with vertically polarized TEM waves traveling in the horizontal plane. Monostatic RCS for three situations, two λ/2 separated masts and a command bridge separated by λ/4 (blue line), front mast excluded (red line), and both masts excluded (green line) are shown in Fig 2.

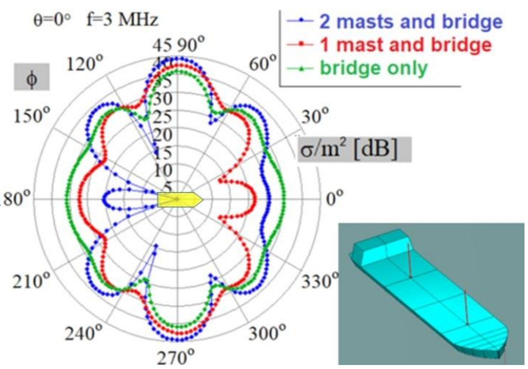

Figure 2. Ship RCS for two masts (blue line), 1 mast (red line) and bridge only (green line). The illustration of ship orientation is shown with yellow object in the center of the diagram.

From Fig. 2 it is observed that monostatic RCS in the direction of ship's axis is reduced when 1 or 2 masts are added compared to the command bridge. Results are generally are dependent on the number of masts and angle of monostatic RCS.

REFERENCES

[1] D. Nikolic, N. Stojkovic, P. Petrovic, N. Tosic, N. Lekic, Z. Stankovic, N. Doncov, "The High Frequency Surface Wave Radar Solution for Vessel Tracking Beyond the Horizon," *Facta Universitatis*, vol. 33, no. 1, pp. 37-59, March 2020.
[2] D. Trizna and L. Xu, "Target Classification and Remote Sensing of Ocean Current Shear Using a Dual-Use Multifrequency HF Radar," *IEEE Journal of Oceanic Engineering*, vol. 31, no. 4, pp. 904-918, October 2006.
[3] WIPL-D Pro v18, WIPL-D, 2022, https://wipl-d.com/.

This research was funded by Vlatacom Institute.

The Directed Energy Center at the University of New Mexico (DEC@UNM)*

Edl Schamiloglu – Director
Department of Electrical and Computer Engineering
University of New Mexico
Albuquerque, NM 87131 USA
edls@unm.edu

Ganesh Balakrishnan – Associate Director
Center for High Technology Materials
University of New Mexico
Albuquerque, NM 87131 USA
gunny@unm.edu

Arash Mafi
Department of Physics and Astronomy
University of New Mexico
Albuquerque, NM 87131
mafi@unm.edu

Abstract— The University of New Mexico (UNM) stood up its Directed Energy Center in Fall 2021, a congressionally mandated initiative. This positions UNM as the only University in the U.S. to have a leading academic research program in both Directed Energy Lasers and Directed Energy Microwaves, with both having experimental and theoretical capabilities. This research effort is complemented by the UNM Global and National Security Policy Institute's Introduction to Directed Energy online course that has been offered every semester since Spring 2017 as part of the Professional Master of Science in Global and National Security (https://gnspi.unm.edu/degrees-and-certificates/masters-degree-.html). The initial focus of the Directed Energy Lasers research is on: Radiation Balanced Fiber Lasers; Integrated Modal Control and Beam Combining of High-Power Diode Laser Arrays for the Next Generation HEL System; Power Scalable Electrically Driven Monolithic IR Surface Emitting Lasers; Novel Microstructured Fibers for Advanced High Power Fiber Lasers; and Hollow-Core Optical Fiber Gas Lasers. The evolving focus of the Directed Energy Microwaves research is to support the U.S. DOD's Electromagnetic Spectrum Superiority Strategy. In this context, the focus is on high power sources of microwaves ranging from X-band to Ka-band. This presentation will summarize the activities of DEC@UNM.

Keywords-directed energy, fiber lasers, semiconductor lasers, quantum dots, high power microwaves

I. INTRODUCTION

The University of New Mexico (UNM) established its Directed Energy Center (DEC) to conduct fundamental and applied research in high-power laser science and technology and high-power microwaves (HPM). The research at UNM-DEC focuses on the ongoing development of optical fiber lasers, semiconductor lasers, other solid-state lasers that can be used in high-power applications; and of HPM oscillators, amplifiers, and components. The primary technical objective of UNM-DEC is to conduct cutting-edge research in lasers and HPM in materials and systems, encompassing theoretical and computer modeling to device fabrication to prototype development. There is a strong demand for DE lasers and microwaves, both in technological innovation and workforce development, to preserve and enhance the dominance of the U.S. in DE technologies. UNM-DEC provides an exceptional platform for both technological innovation and workforce development in DE microwaves and lasers to cater to this demand, which is of prime importance to the national security of the U.S. for commercial and defense technologies.

II. DIRECTED ENERGY LASER RESEARCH

A. Fiber Lasers

Initially, postdoctoral scholars and graduate students are working to establish the DE fiber laser laboratory. Several main research tracks are pursued in the initial phase of the work. These tracks include: (1) the development of high-power sources at 1030 nm wavelength to be used for solid-state laser cooling of Yb-doped silica, and eventually making high-power radiation-balanced fiber lasers; (2) the study and development of fiber lasers and amplifiers in disordered Anderson localizing optical fibers at around one-μm wavelength; (3) the study and development of 3-5 μm wavelength gas fiber lasers. The latter will potentially necessitate the development of fiber-based or semiconductor pump sources at various wavelengths such as 1.5- μm, 2.0- μm, and so on [1,2]. For all these projects, extensive theoretical and modeling efforts are performed using the existing fiber laser and amplifier simulation models or by developing new simulation tools. The simulation tools include pre-developed and newly developed Matlab, Mathematica, Python, and C++ codes, and Comsol Finite Element Models. Some of this development may be performed at the UNM Center for Advanced Research Computing (CARC), which is the hub of computational research at UNM and one of the largest computing centers in the State of New Mexico (NM).

* This research is supported by AFRL Cooperative Agreement FA9451-22-2-0016.

B. Semiconductor Lasers

For the semiconductor laser portion we will develop NIR 976 nm quantum well (QW) and quantum dot (QD) diode lasers. The QW diodes for pumping Yb fiber amplifiers are mature with electrical to optical efficiencies approaching 70%. Our initial objective will be to replicate these efficiencies. We will make use of advanced computations based on many body calculations to design these lasers and model them prior to fabrications. We shall later transition from QW diodes to QD diodes. The dots have superior characteristics compared to wells in terms of metrics such as DI/DT, threshold and beam quality degradation. These will be verified by comparing to QW lasers. We will also put effort into the optimization of epitaxial processes for such lasers. UNM has a state-of-the-art, fully automated VEECO ® GEN 10 reactor for the growth of III-As QW and QD lasers, the reactor is shown in Figure 1. UNM has three decades of expertise in semiconductor QW and QD lasers [3,4].

Figure 1. VEECO ® GEN 10 solid source molecular beam epitaxy reactor for the growth of InGaAs QW and InAs QDs.

III. DIRECTED ENERGY MICROWAVE RESEARCH

For the HPM portion [5], new students are being brought on board who will learn how to run particle-in-cell (PIC) codes (MAGIC, ICEPIC) and other electromagnetic solvers, such as CST Microwave Studio and HFSS for virtual prototyping of HPM sources and components. Newly brought on students will also be mentored by research faculty on experimental techniques using the two accelerators in the *Pulsed Power, Beams, and Microwaves Laboratory* (Figure 2). These new students will complement ongoing research activities on the development of HPM amplifiers, and on continued advances in the relativistic magnetron and the relativistic magnetron with diffraction output (MDO).

Whereas our recent interest has primarily focused in low frequency, L-band and S-band, we did advance E-band (78 GHz) sources under the auspices of the DARPA INVEST program. The UNM group is now seeking, as part of the recently established DEC@UNM to develop pulsed power-driven high frequency HPM sources in the X-band-to-Ka-band range to generate considerable power for front-door disruption against radars, sensors, and other assets employed by our near peer adversaries. Because of the Pf^2 scaling (where P is the output power and f is the frequency) of beam-driven HPM sources, we expect that the power outputs from these sources will decrease as a function of frequency. We will investigate linear beam devices such as backward-wave oscillators (BWOs) and traveling tube amplifiers (TWTs), as well as a relativistic magnetron with diffraction output (MDO), a crossed-field device. In addition, we will advance our earlier work on an E-band power combiner and apply it to the X-band-to-Ka-band frequency range.

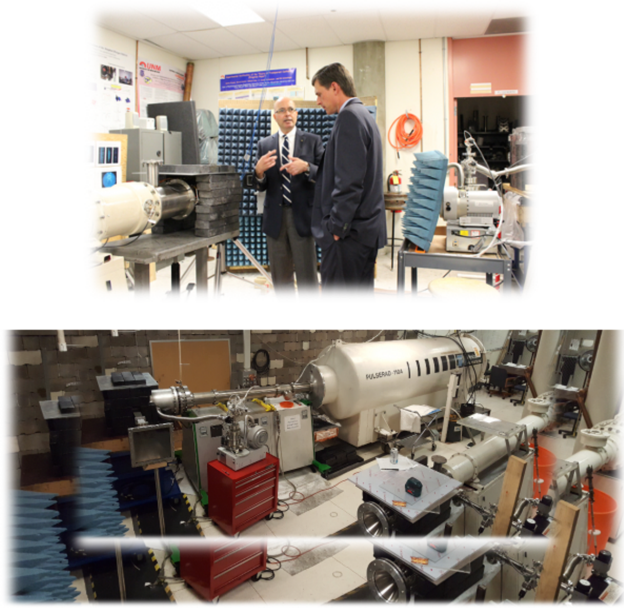

Figure 2. Photographs of the SINUS-6 accelerator (top) and the modified PI-110A accelerator (bottom) used in HPM studies.

REFERENCES

[1] B. Topper et al, "Laser Cooling of a Yb Doped Silica Fiber by 18 Kelvin from Room Temperature," Opt. Lett. 46, 5707-5710 (2021).

[2] B. Abaie, E. Mobini, S. Karbasi, T. Hawkins, J. Ballato, and A. Mafi, "Random Lasing in an Anderson Localizing Optical Fiber," Light Sci Appl 6:e17041 (2017).

[3] G. Liu, A. Stintz, H. Li, K.J. Malloy, and L.F. Lester, "Extremely Low Room-Temperature Threshold Current Density Diode Lasers Using InAs dots in In/sub 0.15/Ga/sub 0.85/As Quantum Well," Electron. Lett., vol. 35, no. 14, pp. 1163–1165, 1999.

[4] A.R. Albrecht et al., "1220–1280-nm Optically Pumped InAs Quantum Dot-Based Vertical External-Cavity Surface-Emitting Laser," IEEE J. Sel. Top. Quantum Electron., vol. 17, no. 6, pp. 1787–1793, Nov. 2011.

[5] J. Benford, J. Swegle, and E. Schamiloglu, *High Power Microwaves, 3rd Ed.* (CRC Press, Boca Raton, FL, 2016).

The Regge Method for a Vertical Half-Circular Loop above Conducting Ground

Sergey V. Tkachenko, Felix Middelstaedt and Ralf Vick
Otto-von-Guericke University, Magdeburg, Germany
e-mail: sergey.tkachenko@ovgu.de

Abstract— The response of the thin-wire half - circular loop perpendicular to PEC ground to the lumped voltage source by application the Regge-Watson transformation is reduced to the sum over frequency-dependent complex values $m_v(k)$ $(v=1,2,3...)$. Corresponding curves $\{Re(m_v(k)), Im(m_v(k)\}$ on the complex m-plane describes deep physical properties of the scattering system.

Keywords- thin wires; circular loop; Regge theory

I. INTRODUCTION

Direct numerical methods, e.g., Method of Moments usually used to calculate EM field coupling with wiring do not allow deep research into the physical essence of the problem. This can only be achieved by using analytical or semi-analytical methods. The exact analytical solutions that are possible for structures with high geometrical symmetry are especially important: an infinite straight wire, a circular wire, a helix wire and their combinations that keep symmetry, e.g., an infinite straight wire over an PEC surface, half-circular loop perpendicular to PEC surface, twisted pairs, etc.

II. RESULTS

Here, we consider a circular half-loop perpendicular to the PEC ground. This structure is the only finite transmission line - like wiring structure for which there is an exact solution to the mixed-potential integral equations. This solution can be obtained by Fourier series for any type of excitations [1], including distributed excitations (e.g., by external plane wave) or lumped excitations (e.g., by voltage source). The solution for the lumped excitation is especially important because it is a Green's function for the current and yields the solution with arbitrary excitation.

To obtain this solution with appropriate accuracy, one has to use 100-400 terms in the Fourier series. In our previous paper [2], we have shown, how to simplify this Fourier solution and, using the phenomenological physical method, approximately obtained the main term of the current excited by lumped source. This current is analog of TEM mode excited by a lumped source in the infinite straight wire above a PEC ground. In this work, we use the Watson - Regge transformation and represent the Fourier sum as an integral in the complex plane of the parameter m, which is an integer in the classical Fourier solution. The integral is defined by the zeros of the modal impedance per-unit length in the complex plane of the parameter m, which zeros define the so called Regge poles, in analogue with scattering theory in quantum mechanics [3].

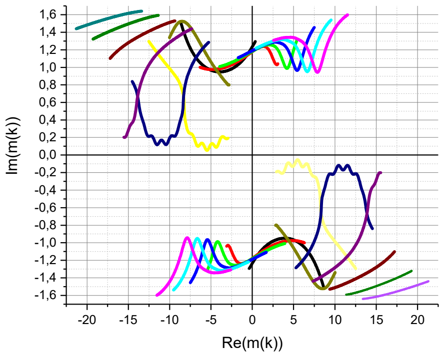

Figure 1. Regge trajectories (26 poles) for circular loop R=4m, r_0=1cm, 0.75 $m^{-1} \leq k \leq 3.875$ m^{-1}.

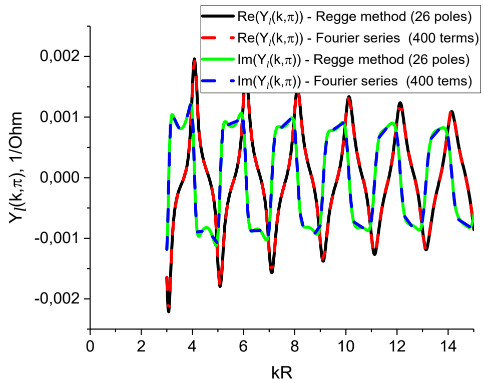

Figure 2. Frequency dependence of the admittance function for current for the circular loop (R=4m, r_0=1cm) calculated by Regge and Fourier methods. Voltage source and observation point are arranged at the points $\phi=0$ and $\phi=\pi$.

The positions of the poles on the complex plane depend on the frequency and form so called Regge trajectories (see Fig.1). The sum over the Regge poles is an exact solution of the problem and equals the sum of Fourier series (see Fig.2). The term corresponding to the pole with the smallest imaginary part coincides with the phenomenological solution. Moreover, after some manipulation on this term, one can obtain the SEM poles of the first layer for the wiring structure.

REFERENCES

[1] L.A. Weinstein, *Open Resonators and Open Waveguides*, Golem Press 1969.
[2] J. Nitsch and S. Tkachenko, "A Lumped Excitation of a Vertical Half-Circular Loop above Conducting Ground,"*2007 Int. Conf. on Electromagnetics in Advanced Applications*, 2007, pp. 752-755, doi: 10.1109/ICEAA.2007.4387412.
[3] T. Regge, "Introduction to Complex Orbital Momenta", Nuovo Cimento, vol. XIV, N. 5, December 1959, pp. 951-976.

Design and Modeling of a Tesla Transformer for HPM Sources

Gideon Nimo Appiah, Fernando Albarracin, Chaouki Kasmi, and Nicolas Mora
Technology Innovation Institute - Directed Energy Research Center, Abu Dhabi, UAE.
gideonnimo.appiah@tii.ae

***Abstract*—**This paper details the design and modeling of a 500 kV pulse generator based on a Tesla transformer for driving a matched low-impedance high-power microwave (HPM) source for a duration of 50 ns. An analytical design approach based on the off-resonance mode of operation of the Tesla transformer is made, and simulations are performed to validate the design process.

Keywords-component; Tesla transformer; pulse generator; numerical analysis.

I. INTRODUCTION

Tesla transformers (TTs) have been used as a primer for particle accelerators and high-power microwave (HPM) sources due to their compactness and high pulse repetition rate capabilities. TTs operating in the off-resonance mode due to a ferromagnetic core exhibit improved coupling coefficient, lower primary circuit voltages, and can be designed with high voltage transformation ratios (~ 1500) [1]. This work aims at presenting an analytical approach and simulation to validate the design of a TT.

II. DESIGN OF THE TT

Fig. 1 shows a schematic diagram of a pulse generator based on a TT, and Fig 2 is a 3D model of the TT. Two inductively coupled circuits oscillate at a resonance frequency, ω to elevate a low voltage into the kV and MV range within a nano or microsecond period.

L_1 and L_2 are the primary and secondary inductances; C_1 and C_2 are the capacitance of the primary and secondary circuits, respectively. The maximum secondary voltage, U_{2max} when the circuits oscillate at their resonant frequency is given as;

$$U_{2max} = U_o\sqrt{\frac{L_2}{L_1}} = U_o\sqrt{\frac{C_1}{C_2}} \quad (1)$$

Korovin showed that the coupling coefficient k due to the presence of a magnetic core can be written as [2];

$$k \approx \sqrt{1 - \frac{8}{3} \cdot F(\beta) \cdot \left(\frac{R_{ex}}{L_{pfl}}\right)^2} \quad (2)$$

where $F(\beta)$ is a structural function defined in [2], R_{ex} is the radius of the external core, and L_{pfl} is the length of the magnetic core. From (2), it shows that for TTs with magnetic cores, k depends only on the geometric properties of the core.

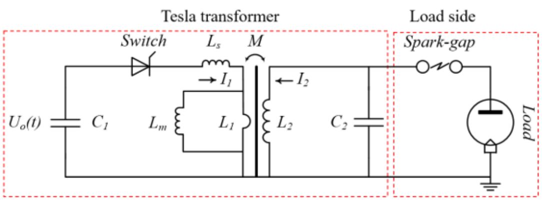

Figure 1. Circuit diagram of open-ferromagnetic cored TT.

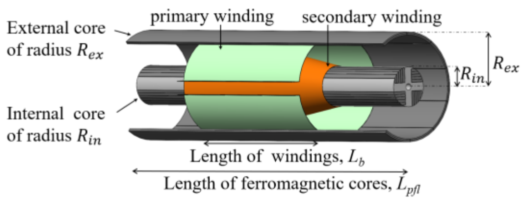

Figure 2. Magnetic core structural diagram of the TT.

III. SIMULATION RESULTS

The input parameters of the TT are shown in Table I. Based on an analytical design approach explained in [2], the calculated parameters of the TT are shown in Table 2. PSICE simulation waveform in Fig. 3. shows that an output voltage and current of 250 kV and 37 kA, respectively, with a 51 ns duration, can be achieved.

TABLE 1. INPUT PARAMETERS OF THE TT

Parameters	U_o	U_{2max}	T_{dur}	Z	ϵ_r
Values	580 V	500 kV	50 ns	6.7 Ω	81

TABLE 2. CALCULATED PARAMETERS OF THE TT

Parameters	L_{pfl}	L_b	R_{in}	R_{ex}	L_s
Values	833 mm	375 mm	41 mm	110 mm	80 nH
Parameters	L_m	L_1	L_2	k	
Values	0.90 μH	0.98 μH	1.24 H	0.96	

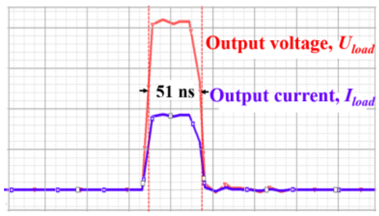

Figure 3. Tesla transformer waveform at rated operations. (U_{load}: 60 kV/div., I_{load}: 20 kA/div., 50 ns/div).

Future work will include electromagnetic simulations to determine areas of electric field enhancements in the PFL and the maximum flux density. The authors look forward to presenting the electromagnetic simulation results during the conference.

REFERENCES

[1] V. V. Rostov, A. S. Stepchenko, P. V. Vykhodsev, and R. V. Tsygankov, "High-voltage drivers based on forming lines with extended quasi-rectangular pulses for high-power microwave oscillators," Electronics, vol. 11, no. 3, p. 406, Jan. 2022.
[2] S. D. Korovin and V. V. Rostov, "High-current nanosecond pulse-periodic electron accelerators utilizing a tesla transformer," Russ. Phys. J., vol. 39, no. 12, pp. 1177–1185, Dec. 1996..

Characterization of a 38-kJ Capacitive Source for an Electromagnetic Accelerator

Aesha AlAli, Fernando Albarracin, Gideon Nimo Appiah, Chaouki Kasmi, and Nicolas Mora
Directed Energy Research Center, Technology Innovation Institute, Abu Dhabi, United Arab Emirates
aaesha.alali@tii.ae

***Abstract*—** This work presents the characterization of a 38-kJ capacitor-based pulse forming unit used as part of the energy source of an electromagnetic accelerator. The voltage and currents through the main components are measured after a 0.6 kV discharge test.

Keywords; capacitor bank, electromagnetic launcher, PFU

I. INTRODUCTION

An electromagnetic accelerator (EMA) thrusts a mobile armature by converting electrical energy into kinetic energy by using the Lorentz force principle. It consists of a capacitive power supply that stores energy and then drives a current pulse to a load made up of parallel rails with a moving armature [1]. Due to the low impedance of the rail-armature setup, the discharge generates currents of dozens of kA from pulse forming units (PFU) charged to voltages of tens of kV. One possible configuration for a PFU comprises a capacitor bank discharged through an inductor by triggering a high-current switch, such as a thyristor; however, spark gaps and thyratrons can also be used [2].

This work presents the experimental characterization of a 38-kJ PFU discharged into the pulse-forming inductor itself. Fiber optic link transceivers were used for both measurement and control subsystems, allowing safe and remote operation of the accelerator.

II. PULSE FORMING UNIT TEST SETUP

The assembly of the 38-kJ energy source for the EMA is shown in Fig. 1a. The module consists of 6 x 125 µF/10 kV capacitors, three 90-kA thyristors, four diodes serving as freewheel mechanisms to protect the capacitors, and a solenoid inductor of 50 µH that connects the power supply to the load. The pulse-forming inductor is short-circuited to the ground to act as the load during the discharge test. Fig. 1b shows the schematic model of the PFU under test.

The capacitor bank charging is remotely controlled via serial communication over a fiber optic link. The control system consists of a compact RIO module, sending a TTL pulse to the thyristor-gate-driver circuit, which triggers the thyristor to discharge the capacitor bank. The measurement system consists of a high-voltage probe and a Rogowski coil whose output signal is transferred to an oscilloscope via fiber optic transceivers, working from DC to 25 MHz. The control system flow diagram is depicted in Fig. 2.

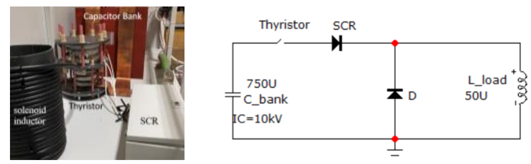

Figure 1. (a) PFU prototype. (b) Circuit model

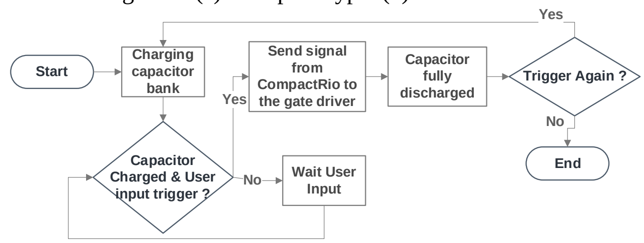

Figure 2. Block diagram of the discharge control.

III. MEASUREMENT RESULTS

Preliminary tests with the PFU charged to 0.6 kV (375 J) were performed. The results are shown in Fig. 2. The load current shows 190 µs rise time and reaches a 1.95 kA peak, indicating a good agreement with the theoretical peak value, computed as

$$I_{peak} = V_0 \sqrt{\omega_0 L_{PFU}} \exp\left(-R\pi / 4\omega_0 L_{PFU}\right) = 2.01 \text{ (kA)} \qquad (1)$$

Where $\omega_0 = 1/\sqrt{C_{PFU} L_{PFU}}$, and R is the equivalent circuit resistance. The resistance from the solenoid (16 mΩ) is the main contributor to R and was used in the calculation. Higher voltage discharge results will be presented during the conference.

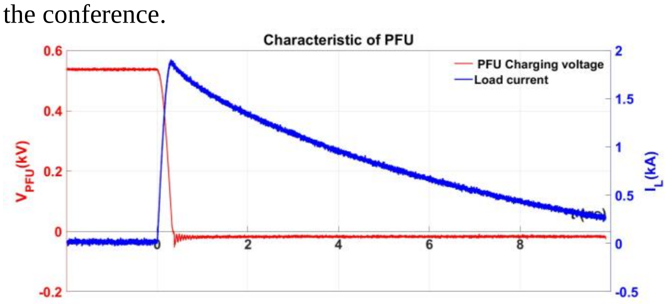

Figure 3. Preliminary experimental results

REFERENCES

[1] W. O. Coburn and W. Williams, “Static and quasi-static models for the magnetic field of a railgun,” IEEE Trans. Magn., vol. 31, no. 1, pp. 692–697, Jan. 1995.
[2] O. Liebfried, V. Brommer, S. Scharnholz, and E. Spahn, “Refurbishment of a 30-MJ-Pulsed Power Supply for Pulsed Power Applications,” IEEE Trans. Plasma Sci., vol. 41, no. 5, pp. 1285–1289, May 2013.

Determination of the Complex Permittivity of E-glass and Balsa wood using a Rectangular Waveguide System

Shaikha AlDhaheri, Papa Ousmane Leye, Chaouki Kasmi, and Nicolas Mora
Directed Energy Research Center, Technology Innovation Institute, Abu Dhabi, United Arab Emirates
shaikha.aldhaheri@tii.ae

Abstract**—** This paper investigates the electromagnetic properties of E-glass and balsa wood, two commercially available dielectric materials. The samples are characterized by calculation and measurement over the X and Ku band frequency ranges (8.2 -18 GHz). A rectangular waveguide system is used for the measurement. The Nicolson Ross Weir (NRW) algorithm is implemented to calculate the complex permittivity and magnetic permeability from the measured S_{11} and S_{21} parameters. In addition, this paper discusses some limitations of the NRW technique to characterize complex permittivity and permeability of low loss materials at frequencies corresponding to multiples of one-half wavelength in the material.

Keywords- electromagnetic characterization, electric permittivity, magnetic permeability, Nicolson Ross Weir (NRW) method, rectangular waveguide

I. INTRODUCTION

The electromagnetic characterization of dielectric materials is relevant to a wide range of practical applications [1]. The use of radar absorbing material (RAM) is a must to stealth the object by reducing the radar cross-section. Several experimental techniques and methods have been developed over the years to measure the complex relative permittivity and complex relative permeability of the materials [1]–[3]. In this paper, the NRW technique is implemented to extract the complex permittivity and permeability of E-glass and balsa wood samples in the X and Ku frequency bands. The equations used and the algorithm to convert from S parameters to dielectric properties are presented. The measurement setup, the calibration, and the measurement procedure are outlined. The measurement results are then compared with the calculation for validation. Finally, the divergence of the NRW technique at frequencies corresponding to multiples of one-half wavelength in the material is highlighted and discussed.

II. MEASUREMENT SETUP

To validate the technique, the samples are measured using a rectangular waveguide system: WR90 for operating frequencies from 8.2 to 12.4 GHz and WR62 from 12.4 to 18 GHz. The experimental setup is shown in Figure 1[2]. A VNA Rhode ‘and’ Schwartz ZNB20, operating from 100 kHz to 20 GHz, and WR90 and WR62 Standard CLKA1 waveguides from Rhode & Schwarz are used to performing the measurement. The material under test is placed between the waveguides, and the S-parameters are measured at the ends of the coaxial cables.

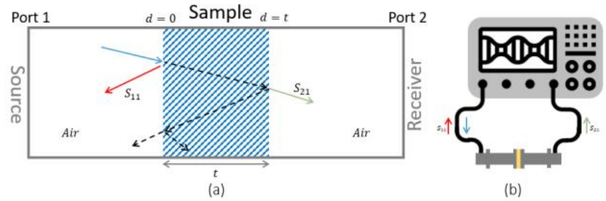

Figure 1: (a) Waveguide section filled with material sample, (b) Experimental setup.

III. METHOD AND DISCUSSION

By assuming no source and load mismatch and solving the boundary condition at d = 0 and d= t, S_{11} and S_{21} can be written as functions of the reflection coefficient (R) and the transmission (T) coefficient between the two faces of the sample [4]:

$$S_{11} = \frac{(1-T^2)R}{1-T^2R^2} \quad (1) \quad ; \quad S_{21} = \frac{(1-R^2)T}{1-T^2R^2} \quad (2)$$

The permittivity and permeability are extracted using the following relationships:

$$\mu_r = \left(\frac{1+\mathrm{R}}{1-\mathrm{R}}\right)\frac{\gamma}{j2\pi\sqrt{\frac{1}{\gamma_0^2}-\frac{1}{\gamma}}} \quad (3) \quad ; \quad \varepsilon_r = \frac{\lambda_0^2\left[\frac{1}{\lambda_c^2}-\left(\frac{\gamma}{2\pi}\right)^2\right]}{\mu_r} \quad (4)$$

Here γ and γ_0 are the propagation constants in the material and vacuum respectively, and λ_0 is the free space wavelength and λ_c is the cutoff wavelength of the waveguide. The algorithm to extract the complex permittivity and permeability is implemented using the above equations.

REFERENCES

[1] F. Costa, M. Borgese, M. Degiorgi, and A. Monorchio, ‘Electromagnetic Characterisation of Materials by Using Transmission/Reflection (T/R) Devices’, *Electronics*, vol. 6, no. 4, p. 95, Nov. 2017, doi: 10.3390/electronics6040095.

[2] A. N. Vicente, G. M. Dip, and C. Junqueira, ‘The step-by-step development of NRW method’, in *2011 SBMO/IEEE MTT-S International Microwave and Optoelectronics Conference (IMOC 2011)*, Natal, Brazil, Oct. 2011, pp. 738–742. doi: 10.1109/IMOC.2011.6169318.

[3] L. Chen, Ed., *Microwave electronics: measurement and materials characterisation*. Chichester: John Wiley, 2004.

[4] A. M. Nicolson and G. F. Ross, ‘Measurement of the Intrinsic Properties of Materials by Time-Domain Techniques’, *IEEE Trans. Instrum. Meas.*, vol. 19, no. 4, pp. 377–382, Nov. 1970, doi: 10.1109/TIM.1970.4313932.

RCS Measurement Technique in Semi-Anechoic Chamber

Papa Ousmane Leye, David Martinez, Shaikha Aldhaheri, Chaouki Kasmi, and Nicolas Mora
Directed Energy Research Center, Technology Innovation Institute, Abu Dhabi, United Arab Emirates
papa.leye@tii.ae

Abstract— This paper presents the implementation of a broadband Radar Cross Section (RCS) measurement system inside the Semi-Anechoic Chamber (SAC) of the Directed Energy Research Center. The setup is used to measure the RCS of a PEC canonical target, and the results are compared with numerical simulations using a rigorous method.

Keywords: Radar Cross-Section (RCS); RCS measurement;

I. INTRODUCTION

The RCS of a target can be estimated using numerical electromagnetic modeling if an accurate 3D geometry of the target is available [1]. An exact numerical calculation of the RCS in the X or Ku band frequencies and for a large bandwidth is often very long and requires a prohibitive memory effort [2]. Therefore, to estimate and validate the numerical prediction, it becomes necessary to have a suitable RCS measurement facility. In general, the measurement of RCS takes place in anechoic chambers [4], that simulate free-space and far-field conditions and where the unwanted reflections are reduced.
This paper focuses on the implementation of an RCS broadband measurement system in a SAC where fully anechoic conditions are not available, and consequently, spurious reflections and interferences become important. Background subtraction and a time gating are performed to extract the target RCS. Finally, the measurement result is compared to numerical calculations.

II. MEASUREMENT SYSTEM

The measurement system is presented in Figure 1.The target is positioned on a Styrofoam column support of 1.5-meter height, and the support is placed on a turntable to rotate the target in azimuth. A laptop is located inside the control room to simultaneously control the VNA and the turntable. The measurement is performed in the azimuth range from -90 to 90 degrees around the target, with a 0.5-degree resolution.

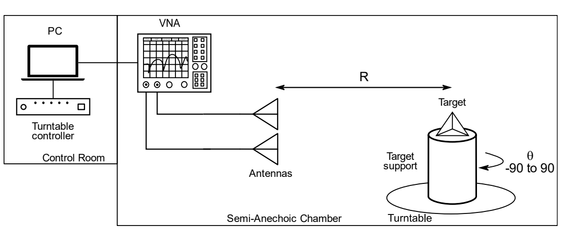

Figure 1: Schematic diagram of the measurement system.

III. RESULT AND DISCUSSION

The RCS of a metallic square trihedral corner reflector of 30 cm sides is measured at 10 GHz for vertical transmit and receive polarization. The measurement is performed using the following steps: First, a full 2-port SOLT (short-open-load-thru) calibration is performed to establish the reference plane at the output of the coaxial cables. Secondly, a metallic sphere of 30 cm diameter (see Figure 2) is used as a reference. The third step consists of measuring the response of the target.

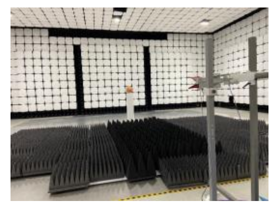

Figure 2:Calibration sphere in the SAC

The geometry of the trihedral and a comparison between measurement and numerical simulation are shown in Figure 3.

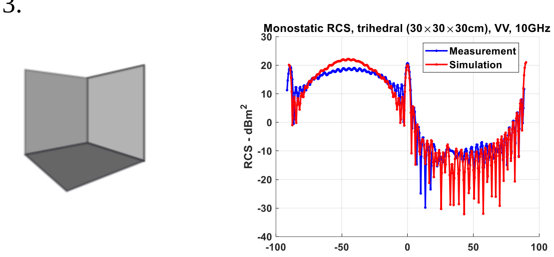

Figure 3: Monostatic RCS of a trihedral corner reflector of 30cm.

According to the plots in Figure 3, between 0 and 90 degrees, the agreement between the simulation and measurement results are very good. Below 0 degrees, the differences are most likely caused by the impact of the imprecise reference target used for calibration. Further discussion will be presented during the final presentation.

REFERENCES

[1] N. N. Youssef, "Radar Cross Section of Complex Targets," *Proceedings of the IEEE,* vol. 77, no. 5, pp. 722-734, 1988.

[2] F. Weinmann, "Ray Tracing With PO/PTD for RCS Modeling of Large Complex Objects," *IEEE Transactions on Antennas and Propagation,* vol. 54, no. 6, pp. 1797-1806, 2006.

[3] D. W. Hess, "Introduction to RCS Measurements," *Loughborough Antennas & Propagation Conference,* 17-18 March 2008.

A Resilience based Approach to HPEM Threat Mitigation

Richard Hoad[1] Ph.D, Barney Petit[1],

[1] QinetiQ Ltd.
Cody Technology Park
Farnborough, Hants, UK
rhoad@qinetiq.com

***Abstract*—** This paper introduces the concept of a Resilience based approach rather than a protection-lead approach to High Power Electromagnetic (HPEM) threat mitigation. It is shown that a resilience based approach is much more intuitive and is how the risk from the majority of common threats are mitigated. The resilience approach and a framework for the management of HPEM resilience is being developed for an update to IEC 61000-5-6.

I. THE PROTECTION-LEAD APPROACH

The earliest standards for High-altitude Electromagnetic Pulse (HEMP) protection of facilities were developed for military use [1]. This is at least partially because the HEMP threat was first acknowledged by the military sector who required a zero-disruption or 'work-through' solution for the HEMP threat. Military HEMP protection standards generally require a high degree of protection, mainly due to the requirement to work-through HEMP events, and also due to the inclusion of significant protection margin so that degradation in the protection performance does not impact the ability of the facility to work-through.

However, military electronic equipment tends to operate in a well bounded-networked manner and is resilient by design. Military facilities that are HEMP protected tend to be continuously staffed with trained professionals who may have dedicated responsibilities for maintenance of the HEMP protection. The protection-lead approach is known to be very effective as long as the 'as-built' protection performance is maintained and continuously assured.

II. A RESILIENCE APPROACH

A protection-lead, work-through, approach described above can be cost intensive, inefficient and very difficult to apply for modern applications and facilities for a variety of reasons which will be discussed in the presentation.

A definition of resilience, used here, is: *'The ability of a system to anticipate, withstand, respond to and recover from a transient electromagnetic disturbance(s) in a timely and efficient manner'*. Note that this definition of resilience includes the requirement for protection (withstand) but other attributes are added. A key change here is a shift in emphasis implied in the protection-lead approach from 'shall continue to work-through', to a 'shall be capable of timely recovery' emphasis in the resilience based approach. For the resilience based approach there is an implied acceptance that the mission or function of a system or facility may be affected or disrupted and therefore that prompt restoration and recovery are likely to be required.

A simple model that describes the necessary attributes that can be used to develop a framework based approach for a resilience based approach is shown in Figure 1. This model is derived from existing, authoritative and peer reviewed principles and practices developed for cyber threats described in the National Institute of Standards and Technology (NIST) Cyber Security Framework [2].

Figure 1 Resilience model

The resilience based approach is intuitive and is used for many other types of common threats. Consider for example the risk of a fire to populated building.

The emphasis in this scheme is in reducing the consequential impact, restoring function and returning to normal operations as quickly as possible. People are not required to work-through the fire.

III. SUMMARY

The resilience based approach is consistent with the practices employed by many modern critical facilities who, for business continuity reasons, often have a clear response and recovery strategy.

The resilience approach and a framework for the management of resilience to HPEM threats is being developed for an update to IEC 61000-5-6 [3] and will be discussed in the presentation.

REFERENCES

[1] R. Hoad and W. Radasky, 'Progress in High Altitude Electromagnetic Pulse (HEMP) Standardization', IEEE Transactions On Electromagnetic Compatibility, Special Issue on HEMP, Vol. 55, No. 3, June 2013

[2] NIST, "Cyber Security Framework," [Online]. Available: https://doi.org/10.6028/NIST.CSWP.04162018 . [Accessed 2022]

[3] IEC 61000-5-6 Ed. 2.0: Electromagnetic compatibility (EMC) – Part 5-6: Installation and mitigation guidelines – Mitigation of external EM influences (in development)

Summary of Lessons Learned to Date from Trial Deployment of HPEM Detectors

Richard Hoad[1] Ph.D, Barney Petit[1], Tim Rees[1], Anatoly Krasavin[1], Grant Hainsworth[1] and Sam Hole[1]

[1] QinetiQ Ltd.
Cody Technology Park
Farnborough, Hants, UK
rhoad@qinetiq.com

Abstract**—** The Totem® detector developed by QinetiQ Ltd. has now been deployed on a trial basis by several different organizations worldwide.

The detector has been devised and developed to detect High Power Electromagnetic (HPEM) environments that may pose a threat to mission critical electronics, and is specifically designed for ground based critical infrastructure settings.

This paper describes the features of the Totem® detector and summarizes some observations and lessons learned from trial deployments.

I. INTRODUCTION

The Totem® detector provides prompt detection of radiated transient E-fields that could pose a threat to the function of electronic systems [1]. The detector has a novel broadband spiral antenna and uses a logarithmic receiver [2]. The detector has on-board flash memory for storing event data, an integral uninterruptable power supply, fiber-optic connections for event data transmission and can be configured to interface with a 24/7 web service. A photograph of the TOTEM detector is shown in Figure 1.

Figure 1. TOTEM detector, Courtesy of QinetiQ Ltd.

II. FEATURES

The characteristics of this detection system are as follows:

- Frequency Range: 10 MHz to 10 GHz
- Instantaneous bandwidth: ~ 100 MHz – proven to detect Hyperband environments (200 ps pulse width)
- GPS/GNSS interference detection
- Event Log: EM protected event logger recording event time, date and magnitude – approx. 1e^6 event records
- Includes integrated battery backup in the event of power outage in normal operating conditions
- Fiber-optic ports for data transmission

EM detection is a vital component for efficient, effective and timely recovery of a system function, if a Resilience approach to EM threat mitigation is used [3].

The primary use and benefits of detection of man-made HPEM is to aid efficient and timely recovery and provide condition monitoring/data intelligence. Such data can be used to identify the prevalence of radiated EM threats and guide the adoption of cost-effective protection. The installation of detectors also serves to raise awareness of the plausible existence of the threat to system operators.

II. RESULTS

Figure 2 shows data gathered from deployment of the Totem® detector at a High Voltage (HV) electrical sub-station site in Scandinavia.

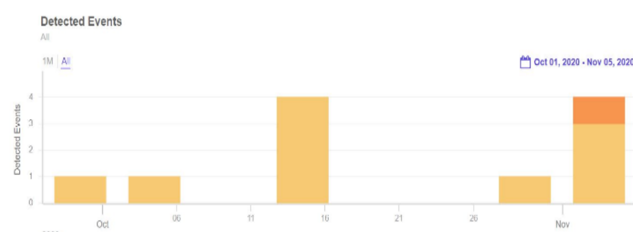

Figure 3. Event data from a Scandinavian HV sub-station

After some analysis and comparisons with data from substation switching logs it was identified that the recorded events correlated perfectly (within 1 second) with a particular circuit breaker switching (closing). No malicious events were detected during the 9 month trial and all events were correlated to the radiated fields from the circuit breaker. Interestingly, the events on the right hand side of figure were quite severe in magnitude, yet no malfunction of equipment at the substation was reported.

We will explain and provide further examples in our presentation.

REFERENCES

[1] D. Herke, L. Chatt, B. Petit and R. Hoad ‘Lessons Learnt From IEMI Detector Deployments’, EUROEM 2016, Imperial College, London, UK, July 2016

[2] Hoad R., Herke, D. L., ‘Electromagnetic Interference Indicator and Related Method’, International Patent Publication Number: WO17/125465 A1, filing date 19 January 2017

[3] IEC 61000-5-6 Ed. 2.0: Electromagnetic compatibility (EMC) – Part 5-6: Installation and mitigation guidelines – Mitigation of external EM influences (in development)

Electromagnetic Shielding in Rock Tunnels

Cables creating path through the coverage

Jostein Godø
National Centre for Protection of Buildings
Forsvarsbygg (NDEA)
Oslo, Norway
Jostein.godo@forsvarsbygg.no

Abstract—For various reasons, some facilities are constructed below ground. One reason could be protection, but not necessarily against IEMI. The ground or rock will however provide some shielding. In this work, measurements has been carried out to explore protection in underground facilities that was not planned for IEMI protection. Originally, the study was only meant to investigate the rock.

Keywords-IEMI protection; underground facilities

I. INTRODUCTION

Soil and rock can provide a certain protection against IEMI. The attenuation will depend on several parameters, like thickness, humidity and chemical composition. Concrete lining, with rebar will also have an effect. The shielding will be greatly dependent on frequency. However, like for shielding enclosures there is an issue about access to shielded space and connection to the outside world. When the shield is quite thick, handling these penetrations can be more complicated.

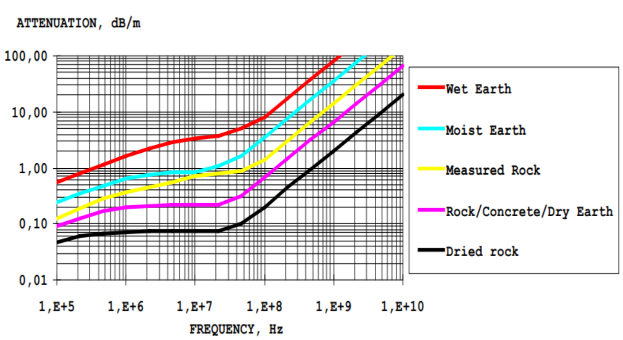

Figure 1 Some calculations of attenuation in coverage[1]

II. MEASUREMENTS

The first investigation of the facility was planned to be done by using whatever transmitters that were present for the higher frequencies, and for lower frequencies a magnetic field transmitter was placed on the inside of the facility.

A. *High frequency measurements*

Simple measurements were done by measuring field strength from transmitters for radio, TV and cellular base stations on the outside and on the way inside the facility. The signal was dramatically reduced after the first bend of the tunnel.

B *Low frequency measurements*

For low frequency measurements, a magnetic transmitter was placed inside of the facility. Measurements were then done on the outside of the facility with some distance to the tunnel opening. Attenuation in rock and concrete lining could be up to 50 dB at 10 MHz.

At a location a road with lampposts were crossing over the facility. Stronger signal was found near the lampposts than closer to the transmitter. Between the road lighting and the location of the transmitter there were transformers, and the cabling between them were in a quite long trace.

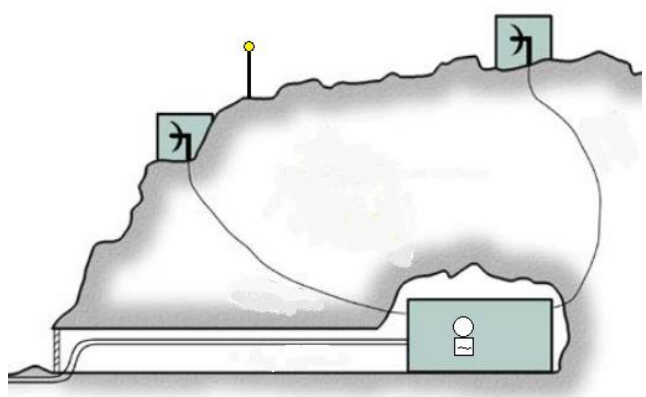

Figure 2 Low frequency measurements, magnetic transmitter inside facility

REFERENCES

[1] K. L. Grønnhaug, “Shielding Against HPM by Overhead Covers”, Tactical Implications of HPM Copenhagen, Denmark 11-13 June 2002

David V. Giri, Switzerland's HPEM Conveyor

Markus Nyffeler
retired, armasuisse Science and Technology
HPE-Laboratory Spiez
Thun / Spiez, Switzerland
markus.nyffeler@visentec.com

Armin W. Kälin
EMProtec AG
Schaubenstrasse 4
Andelfingen, Switzerland
armin.kaelin@emprotec.ch

Abstract — Since the 1970's, the Swiss defense authorities became increasingly concerned about threats posed by Nuclear Electromagnetic Pulse (NEMP) and started to investigate the effects as well as protection methods against High-Power ElectroMagnetic (HPEM) sources. The Swiss EMP Group in the Lab Spiez met Dr. Dave Giri in 1985 on the occasion of an "EMP Interaction and Hardening" short course in Interlaken, Switzerland. This was the beginning of a fruitful and enduring cooperation with Dave. He had a close scientific and personal relationship with Dr. Carl Baum, who already then was a leading scientist in the HPEM community. Carl's theories and ideas and Dave's talent to make ideas work for Swiss protection needs formed a unique combination which contributed a lot to the HPEM community and to standardization.

Keywords - NEMP; HPEM; interaction; hardening; protection, standardization

I. YEARS OF VALUABLE COLLABORATION

From the beginning of our cooperation Dave Giri's talent to translate complex theory into understandable technical information was the key to lead Swiss research projects to success. In a pragmatic way Dave identified opportunities from discussions with research partners and helped to find ways simple enough for quick implementation.

As a neutral country and due to the lack of standards until the 1990's Switzerland had to evaluate and define its own protection requirements. These had to be realistic, yet still meet the limited budget of a small country. The requirements were based on theory and were verified by threat-level tests in our lab. Over the years many results were presented to an interested audience during HPEM conferences. This brought wide recognition and some results also contributed to international standardization.

II. EXAMPLES OF JOINT RESEARCH

Over the years Dave Giri supported many Swiss research projects, such as the investigation of the shielding effectiveness of cylinders and cubes made of rebar mesh by theoretical models and experiments, including time-domain tests using the Swiss MEMPS simulator. The immunity of electronic components was tested using Low Power Microwaves (LPM). The source was taken from a modified microwave oven with a parabolic antenna.

As the world's leading EMP-simulator designer Dave Giri also calculated the antennas of the Swiss EMP simulators. He was involved in the design of VERIFY, one of the fastest EMP-simulators, and in the VEPES modification.

In 1995 Dave Giri and Armin Kälin (then head of the Swiss EMP group) sketched the first HPEM spectrum [1] (Fig. 1) and presented it at AMEREM'96 in Albuquerque. Later the HPE-spectra were adapted for the IEC standards 61000-1-5 [2], 61000-2-13, 61000-4-35 and 61000-4-36.

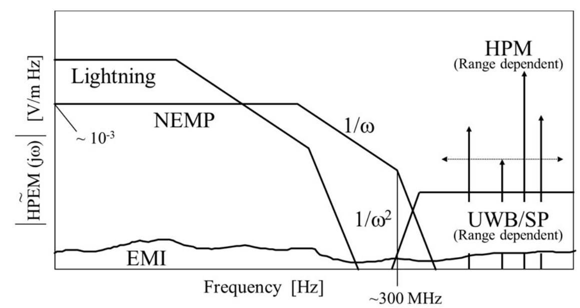

Figure 1. Initial version (1996) of HPEM-spectra [1].

Further collaboration with Dave includes the development of Swiss Impulse Radiating Antennas (SwIRA diameter 1800 mm and SwHIRA 1410 mm).

Typical Swiss civil protection shelters were assessed with respect to HPEM threats. In 2006 Dave designed oscillators for the generation of damped sinusoidal pulses. Armasuisse purchased 200 MHz and 500 MHz oscillators with output voltages up to 30kV. These are used as electromagnetic wave radiators in the Swiss Half IRA (SwHIRA) for the test of various objects.

In 2009 Dave designed and realized a 300 kV feed which permits to use the GTEM 3500 cell in pulsed mode.

These and more collaboration projects with Dave will be presented in more detail during the oral session.

Over the years Dave Giri shared a lot of ideas and experience with us. For us Dave is much more than a scientific mentor, he is a very good friend.

REFERENCES

[1] David V. Giri and Armin W. Kaelin
"Many Faces of High-Power Electromagnetics (HPEM) and Associated Problems in Standardization," AMEREM'96 Meeting, Kirtland AFB, Albuquerque NM, 1996

[2] IEC International Electrotechnical Commission, Geneva
"High power electromagnetic effects (HPEM) on civil systems", IEC TR 61000-1-5, First Edition 2004-11

Extrapolation of truncated transfer functions for compensating time-domain measurements

David Martinez, Chaouki Kasmi, and Nicolas Mora
Directed Energy Research Center, Technology Innovation Institute, Abu Dhabi, United Arab Emirates
david.martinez@tii.ae, chaoiki.kasmi@tii.ae, nicolas.mora@tii.ae

***Abstract*—**Three methods (M1-M3) are implemented to extrapolate the missing spectrum of a truncated cable transfer function. The accuracy of the extrapolation methods is tested by de-embedding the measurement of several time-domain pulses with a rise time between 100 to 1000 ps. Rise time and peak amplitude errors are calculated and compared with the incident pulses waveform parameters.

Keywords— Extrapolation, Hilbert transform, transfer function

I. INTRODUCTION

Subnanosecond HPEM sources produce fast pulses with spectral content reaching the GHz range. The measurement chain used to characterize such systems comprises numerous elements such as sensors, baluns, attenuators, and cables (see, e.g., Figure 1). Interpolation and extrapolation methods are usually required during signal processing to adequately compensate in the frequency domain since the measurement chain elements are generally characterized in separate frequency spans and different frequency steps.

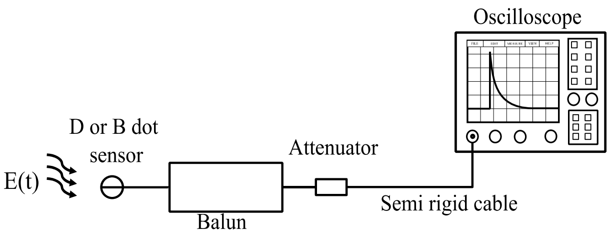

Figure 1. Simplified block diagram for time-domain measurements.

The real and imaginary parts of the complex transfer functions obtained after interpolation and extrapolation must satisfy the Kramers-Kronig relations. Previous authors have proposed reconstructing missing or corrupted data using these criteria. For example, a minimum phase reconstruction of a waveform from its spectral magnitude response was proposed in [1]. A comparison between the Cauchy method and the discrete Hilbert transform properties is proposed for interpolating and extrapolating a corrupted spectrum in [2]. The Hilbert transform integrals in the Z-domain were used to guarantee causality in [3].

II. MEASUREMENT SETUP

The measurement setup is composed of a D-Dot sensor, a balun, a variable attenuator, and a semi-rigid cable connected to a fast 40 GSa/s – 6GHz oscilloscope, as shown in Figure 1. The S-parameters of the semi-rigid cable were measured using a Vector Network Analyzer (VNA) between 100 kHz to 20 GHz in 10^4 points. The cable transfer function (TF) was truncated between 10 MHz and 3 GHz to test the accuracy of extrapolation algorithms.

Three extrapolation methods were implemented to reconstruct the truncated TF missing spectrum. M1 uses a constant extrapolation by keeping the last measured value of the truncated spectrum, while M2 uses 10 dB/dec attenuation to reconstruct the high-frequency spectrum. Finally, M3 uses the Hilbert transform in Z-domain [3]. The comparison between the measured and extrapolated TFs is shown in Figure 2.

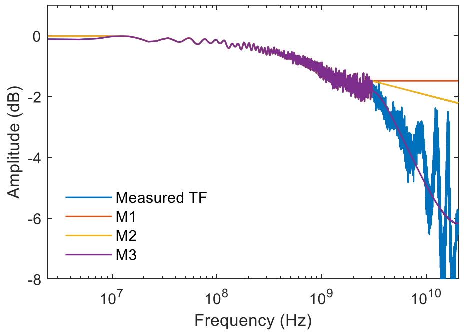

Figure 2. Extrapolated transfer functions of the semi-rigid cable.

III. RESULTS

Several incident EM pulses are simulated with a rise time between 100 ps to 1000 ps and 30 kV/m peak amplitude to test the accuracy of the extrapolation. The expected signal at the oscilloscope is calculated numerically using the measured cable transfer function. Then, the incident electric field is determined by compensating for the cable presence by using the reconstructed spectra with M1-M3. The D-Dot sensor, balun, and variable attenuator are assumed as ideal elements. The obtained waveform parameters (rise time and peak amplitude) are calculated and compared between the incident and compensated electric fields.

REFERENCES

[1] F. M. Tesche, “On the use of the Hilbert transform for processing measured CW data,” *IEEE Transactions on Electromagnetic Compatibility*, vol. 34, no. 3, pp. 259–266, 1992, DOI: 10.1109/15.155838.

[2] S. Narayana, T. K. Sarkar, R. Adve, M. Wicks, and V. Vannicola, “A Comparison of Two Techniques for the Interpolation/Extrapolation of Frequency Domain Responses,” *Digital Signal Processing*, vol. 6, no. 1, pp. 51–67, 1996, DOI: 10.1006/dspr.1996.0006.

[3] J. Becerra, F. Vega, and F. Rachidi, “Extrapolation of a Truncated Spectrum With Hilbert Transform for Obtaining Causal Impulse Responses,” *IEEE Transactions on Electromagnetic Compatibility*, vol. 59, no. 2, pp. 454–460, 2017, DOI: 10.1109/temc.2016.2613044.

Spectral Response of the Conical Monopole Sensor Calibration Setup

Hamad Deiban, Fernando Albarracin, Chaouki Kasmi, and Nicolas Mora
Directed Energy Research Center, Technology Innovation Institute, Abu Dhabi, United Arab Emirates
Hamad Deiban@tii.ae

Abstract—This work presents experimental results of the conical monopole over a ground plane when used as a calibration setup for electric and magnetic field sensors working up to several GHz.

Keywords-component; conical monopole antenna, sensor calibration, D-dot, B-dot, spectral response.

I. INTRODUCTION

The measurement of the transient electromagnetic fields from high-power electromagnetic (HPEM) sources demands the spectral characterization of wideband sensors. A calibration setup with a known multi-decade spectral response is preferred to obtain meaningful results when the sensor under test (SUT) is present. The use of a short conical monopole over a ground plane has been first proposed in [1] to calibrate D-dot and B-dot sensors up to 3 GHz. The authors presented the spectral response analysis of the conical monocone in [2].

The calibration setup scheme is shown in Fig. 1a. The ratio of the electric field E_θ to the input voltage V_{in}, namely the calibration setup transfer function TF_{CS}, can be expressed in a closed form for θ close to 90º (i.e., near the ground plane), as

$$TF_{CS} = \frac{\tilde{E}_\theta}{\tilde{V}_{in}} = \frac{Y_{in}}{f}\frac{a_2}{4\pi}\eta_0\left(j\frac{2\pi f^2}{c_0 r} + \frac{f}{r^2} - j\frac{c_0}{2\pi r^3}\right)e^{-j2\pi rf/c_0} \qquad (1),$$

where E_θ is the radiated electric field, V_{in} is the input voltage, Y_{in} is the monocone input admittance, a_2 is the generatrix, r is the distance between the monocone and the SUT, f is the frequency, c_0 is the speed of light, and η_0 is the free space impedance.

II. EXPERIMENTAL SETUP

A stainless steel, 2.4 x 2.4 m^2 table is used as the ground plane. A resin base was 3D printed to hold the conical monopole. An RG405 coaxial cable with an SMA connector is used to feed the monopole. A picture of the calibration setup is shown in Fig. 1b.

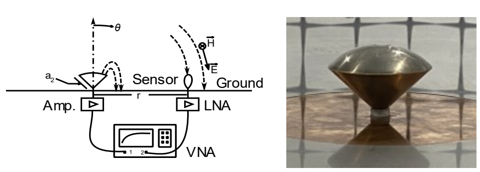

Figure 1: Short-Monocone Setup. (a) Test scheme. (b) Fabricated setup inside a semianechoic chamber

A. Impedance characterization

A comparison of the measured, simulated, and calculated input impedance of the monopole is shown in Fig 2. The shifting towards lower frequencies in the measurements can be attributed to a higher permittivity of the resin in the apex of the monopole.

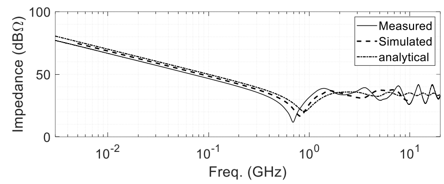

Figure 2: Conical monopole impedance

B. Radiated Field Response

Fig. 3 shows TF_{CS} computed as (1), for the setup in Fig. 1a., comparing both cases of the analytical and the measured conical monocone impedances. An R&S® VNA is used to measure the S_{21} parameter from 100 kHz to 20 GHz, with a resolution bandwidth of 5 kHz. This test considered three distances 150 mm, 300 mm, and 500 mm.

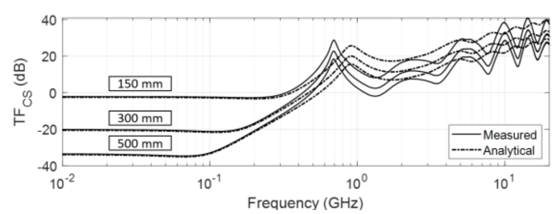

Figure 3: $TF_{CS}(f)$ experimental response

A steeper increase in the magnitude of TF_{CS} is observed around 700 MHz, this is due to the inverse relation of E_θ with the cone impedance in (1). Fluctuations in TF_{CS} at higher frequencies are expected due to imperfections in the coaxial-monocone transition, and the presence of the resin support. The response at lower frequencies agrees on the analytical up to 300 MHz. The upper bound of the available bandwidth is the frequency at which the TF_{CS} is predictable. The lower bound depends on the noise floor of the VNA, once the amplifiers are included. These results are promising for the calibration of commercial electric and magnetic sensors.

REFERENCES

[1] F. Bieth and P. Delmote, "Calibration With a Monocone on a Ground Plane," *IEEE Trans. Plasma Sci.*, vol. 45, no. 10, pp. 2744–2747, Oct. 2017.
[2] F. Albarracin, D. Martinez, G. N. Appiah, J. Galvis, C. Kasmi, and N. Mora, "Spectral Response of the Conical Monopole as Field Sensor Calibration Setup," *IEEE Lett. Electromagn. Compat. Pract. Appl.*, pp. 1–1, 2022.

Aircraft Detection Using HF Radar

Pavle Z. Petrović[1,2], Nemanja R. Grbić[1,2], Nikola Lekić[2], Miroslav Perić[2], and Slobodan V. Savić[1]
[1]University of Belgrade, School of Electrical Engineering, Belgrade, Serbia
[2]Vlatacom Institute of High Technologies, Belgrade, Serbia
pavle.petrovic@vlatacom.com,
nemanja.grbic@vlatacom.com,
nikola.lekic@vlatacom.com,
miroslav.peric@vlatacom.com, ssavic@etf.bg.ac.rs,

Abstract—High-frequency surface-wave over-the-horizon radar (HF SW-OTHR) systems have proven themselves to be a reliable tool for maritime surveillance. However, the surface-wave mode of propagation is closely bound to the surface of the sea, making it not suitable for detection and tracking of targets at greater altitudes, such as airplanes. This paper explores the possibility of using free-wave-propagating electromagnetic wave for aerial targets surveillance using radar in the HF band.

Keywords - High-frequency OTHR radar, aircraft detection.

I. INTRODUCTION

High frequency (HF) radar systems for aerial target detection is a well-known area, as some of the first radar systems in the world operated close to, or in this frequency band. Despite that, there is renewed interest in aerial target detection in this frequency band as high-frequency over-the-horizon radars (HF-OTHR) are becoming more common for ship detection and tracking. The possibility of extending the usability of HF-OTHR for airplane detection and tracking is explored in this paper.

II. NUMERICAL MODEL AND COVERAGE ZONE

The surface-wave mode of propagation generated by the HF-OTHR systems decays exponentially away from the air-sea boundary surface [1]. In the HF band, and for standard seawater electric parameters [2], the result is that the amplitude of the electromagnetic (EM) field will decay e ≈ 2.72 times at heights of several tens of meters. As most aircraft fly at altitudes higher than that, this makes the surface-wave mode of propagation not suitable for the detection of aerial targets and free-wave mode should be used instead. For successful detection using free-wave mode, following conditions should be met: (i) Total distance between radar transmitter (Tx) and target, and between target and radar receiver (Rx) must satisfy the radar equation [3] for the signal-to-noise ratio (SNR) to be high enough for a target to be detectable. (ii) There must be a line of sight between the radar and the target. Refraction of EM field occurring in the atmosphere, altitudes of radar sites and the target must be taken into account [4]. The radar cross section (RCS) for the commercial airplane (Boeing 737) is estimated using 3-D EM modeling software WIPL-D Pro [5], as seen in Fig. 1. A frequency of 25 MHz was considered with a horizontal polarization to suppress the surface-wave mode of propagation.

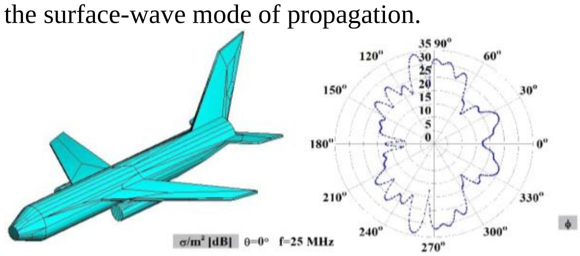

Figure 1. WIPL-D model and RCS for Boeing 737.

The zones of coverage are approximately calculated and shown in Fig. 2 for a hypothetical bistatic radar scenario for which existing Vlatacom HF radar [6] is used to detect Boeing 737 from Fig. 1. In Fig. 2 distances of possible detection are represented in different colors for different altitudes of flight. For the presented results it is estimated that for large targets (Boeing 737) detection is possible over 400 km, depending on the altitude of flying. In these results, the line of sight is the stricter limiting factor for detection (condition (ii)). For smaller targets, this is not the case, and condition (i) must be also considered. Elliptical arcs having constant mean distance between the radar and target are shown in white line (Tx and Rx are their focal points, shown in red dots).

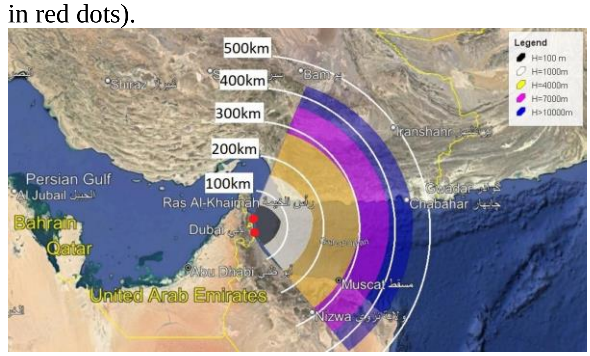

Figure 2. Coverage zone for a bistatic HF radar.

REFERENCES

[1] R. E. Colin, *Field Theory of Guided Waves*, 2nd ed., New York, NY, USA: Wiley-Interscience, 1990.
[2] ITU-Recommendation P.368-9 Ground-wave propagation curves for frequencies between 10 kHz and 30 MHz.
[3] M. Skolnik, *Radar Handbook*, 3rd ed. New York, NY, USA: McGraw-Hill, 2008.
[4] A. Abu-Almal, K. Al-Ansari, "Calculation of Effective Earth Radius and Point Refractivity Gradient in UAE," *Int. J. Antennas Propag.*, vol. 2010, pp. 1-4, May 2010.
[5] WIPL-D Pro v17, WIPL-D, 2020, https://wipl-d.com/.
[6] D. Nikolic, N. Stojkovic, P. Petrovic, N. Tosic, N. Lekic, Z. Stankovic, N. Doncov, "The High Frequency Surface Wave Radar Solution for Vessel Tracking Beyond the Horizon," *Facta Universitatis*, vol. 33, no. 1, pp. 37-59, March 2020.

MOSFET Failure Modelling in Flyback SMPS Under High Level Conducted Electrical Pulses

L.Curos, G.Mejecaze, F.Puybaret
CEA, DAM, CEA-Gramat
F-46500 Gramat, France
laurine.curos@cea.fr

T.Dubois, J-M. Vinassa
Univ. Bordeaux, CNRS, Bordeaux INP,
IMS UMR 5218, F-33400 Talence, France

Abstract—This paper presents an investigation aiming to determine the thresholds that lead to the destruction of the MOSFET transistor used in flyback switch mode power supplies. This thresholds will be used to build behavioral failure models able to predict the destruction of power supplies in the case of HEMP scenario.

Keywords—HEMP; NEMP; Switch-Mode Power Supply (SMPS); MOSFET failure; behavioral model; modelling.

I. INTRODUCTION

Intentional Electromagnetic interferences such as High Altitude Nuclear EM Pulse (NEMP/HEMP) are able to generate electrical disturbances, similar to those produced by lightning. In such scenario, NEMP couples efficiently on aerial lines of the electricity distribution network and parasitic currents/voltages are propagated to the different electronic devices plugged to the grid, such as Switch-Mode Power Supplies (SMPS) [1]. To predict the SMPS failure level using simulation tools, it is important to study and understand the effects of such high amplitude current pulse. During several tests consisting in injecting high current pulses at SMPS input, it has been observed that the disturbance flows through all the SMPS functions causing the destruction of several components. The chronological events of the destruction effects have shown that MOSFET transistor was the first destroyed element in SMPS [2]. The aim of this paper is to determine the destruction levels of SMPS MOSFET transistor and develop a predictive failure model.

III. FAILURE MODELLING

An electrical stress generator is used to inject various electric pulses on MOSFET terminals. Injection stress on the gate permits to obtain a gate failure threshold. Moreover, the injection of an increasing voltage signal between drain-source (gate short circuited) has shown the failure limit due to avalanche phenomenon. Associated to measurements, X-rays pictures and microscopy analyses have been performed on destroyed transistors to observe failures in MOSFET structure. Based on obtained experimental failures results (avalanche voltage failure threshold and gate voltage failure threshold), a MOSFET failure model has been built. The modelling of MOSFET failure consists in using switches controlled by the determined failure levels. In this way, the equivalent component state after failure (Equivalent failure model in Fig. 1) replaces the manufacturer model when simulated voltage or/and current, for a specific time duration, are higher than the failure levels. Switches and equivalent failure model are described in a VHDL-AMS model block that is presented in Fig.1.

This study has been carried out with the support of the Direction Général de l'Armement (DGA) and of the Agence Innovation Défense (AID), both belonging to the French Ministry of the Armed Forces.

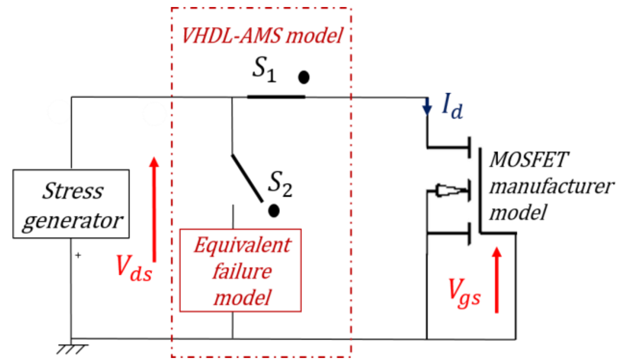

Figure 1. Experimental setup to inject stress between MOSFET drain-source terminals.

The developed model has been integrated into Simplorer simulation software. The amplitude and the global shape of the signals simulated during disturbance injection correlate with the measured voltage and current. The comparison between simulation and measurements permit to validate the built MOSFET failure model.

IV. CONCLUSION

This paper describes the failure modelling method on the MOSFET transistor in SMPS. For each destroyed component, failure models have been developed and integrated into Simplorer simulation software in order to understand and predict the SMPS behavior when a very high amplitude current pulse is injected at its input.

REFERENCES

[1] M. Camp and H. Garbe, "Susceptibility of Personal Computer Systems to Fast Transient Electromagnetic Pulses," IEEE Trans. EMC, vol. 48, pp. 829–833, November 2006.
[2] G. Mejecaze, L. Curos, F. Puybaret, T. Dubois and J.-M. Vinassa, "Destruction scenario of power supply due to conducted pulse from HEMP," GlobalEM, 2022.

Design of a Dielectric Waveguide Sensor for Pseudo-Transmission Measurements

Christoph Baer
Ruhr University Bochum, Institute of Electronic Circuits
Bochum, NRW, Germany
Christoph.Baer@rub.de

Abstract—This contribution discusses a novel, dielectric waveguide (DWG) based, permittivity sensor. A design concept, that realizes a pseudo-transmission measurement approach for attenuating disturbing feed-side reflections, is presented. Measurement results, which prove the high measurement accuracy and sensor applicability, are discussed in detail.

Permittivity Sensor, Dielectric Waveguide, Time Domain

I. INTRODUCTION

Microwave based, time domain (TD) sensors are a popular alternative for the measurement of material parameters such as the material's permittivity. Independently of the actual sensor design, TD sensors have in common that when stuck into a material under test (MUT) the propagation velocity of an electromagnetic wave is altered. Furthermore, all TD sensors must tackle the challenge of feed-side and multiple reflections as these can mask or disturb the actual signal of interest. In the past, this challenge has been mastered by designing transmissometry sensors for line-bound setups [1] or pseudo-transmission sensors for free-space applications [2]. In this work, a pseudo-transmission sensor is introduced that realizes a pseudo-transmission approach on a DWG.

II. SENSOR DESIGN

Quadratic DWGs provide a broad mono-mode operation area for their fundamental mode, which is ideal for a sensor design. By applying a transpolarizing reflector to the DWG's end, a pseudo-transmission structure is realized as the in- and outbound signals are decoupled in their polarization and are therefore orthogonal. However, when using DWGs as TD sensor, one need to consider that the DWG's group velocity increases with the surrounding permittivity. By applying Marcatili's approximation, the group velocity of a specified DWG can be calculated as shown in Fig. 1. The sensor setup is completed by adding an orthomode transducer, which discriminates the polarizations of the in- and outbound signal, a DWG feed as well as a transpolarizing reflector must be added to the DWG structure. Fig. 2 shows a photograph of final sensor

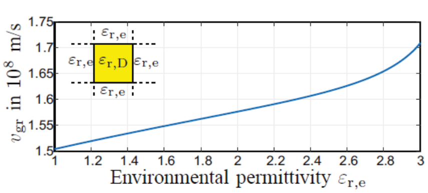

Figure 1: Group velocity of a quadratic DWG (w = 8.5 mm, $\varepsilon_{r,D}$ = 3, f =25 GHz) for different environmental permittivities $\varepsilon_{r,e}$.

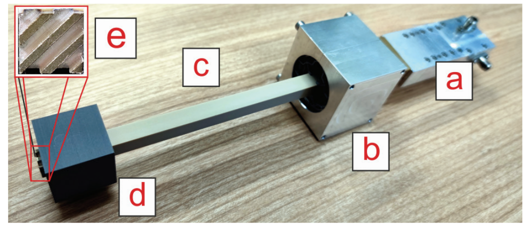

Figure 2: Photograph of the sensor setup indicating: a) OMT, b) corrugated DWG feed, c) rectangular DWG, d) MUT, and e) transpolarizing reflector.

setup. The transpolarizing reflector was realized by metallic, λ/4-deep gratings, orientated 45° to the propagation mode's electrical field direction.

III. RESULTS

The illustrated sensor operates in K-band and is capable to measure permittivities in the range of 1< $\varepsilon_{r,e}$ < 3. Test measurements were recorded by means of a calibrated VNA and 3D-printed test objects with different permittivities. Consequently, the S11-parameter illustrates

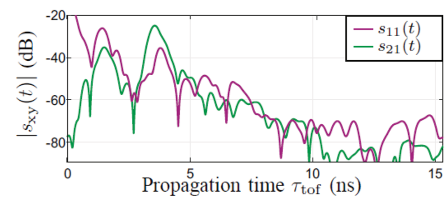

Figure 3: Measured co- and cross-polarized signals in time domain for an MUT permittivity of εr,e = 2.48.

the direct reflection signal, which contains all disturbing reflections, while the S21-parameter represents the pseudo-transmission signal. Fig. 3 shows that the pseudo-transmission design is successfully realized as feed-side reflections are attenuated by more than 15 dB compared to S11. Fig.4 reveals that the fundamental dependency between surrounding permittivity and increasing group velocity was proven. Moreover, the proposed setup is applicable for permittivity measurements as the obtained permittivities have an error of only 0.4%.

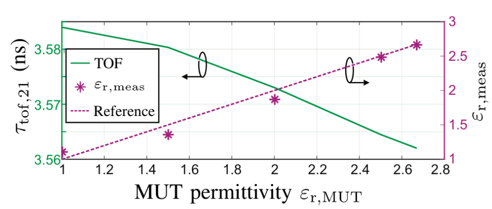

Figure 4: Measured propagation times and derived, MUT permittivities compared to the ideal MUT permittivities.

REFERENCES

[1] B. Will, et al, A time domain transmission measurement system for dielectric characterizations, Int. J. of Microwave and Wireless Tech., vol. 4, no. 3, pp. 349355, 2012.
[2] C. Baer, et al, "Pseudo transmission measurement concept for the volume fraction determination of rice in a pneumatic conveying system," Int.Conf. on Electrom. in Advanced Applications, 2012, pp. 744-747

EMC Capabilities at TII

Islem Yahi, Ali Yaqoob, Aysha Al Neyadi, Chaouki Kasmi, and Nicolas Mora
Directed Energy Research Center, Technology Innovation Institute, Abu Dhabi, United Arab Emirates
islem.yahi@tii.ae

Abstract**—**This paper presents an overview of the Electromagnetic Compatibility (EMC) testing capabilities that are available within the Technology Innovation Institute (TII) - Directed Energy Research Center (DERC). The EMC Lab provides a large panel of testing services covering several international standards (automotive, industrial, or military). The facility can perform emission and immunity testing on systems, subsystems, or platforms up to the size of a vehicle.

Keywords: EMC, Emission, Immunity, Susceptibility, Electromagnetic Pulse, ESD

I. INTRODUCTION

The TII-DERC has designed and built cutting-edge laboratories for acoustics, electromagnetics, and optics to support all their research activities. These laboratories have been built with a network of partners keen to support the center's vision. The EMC laboratory aims to provide large testing facilities within the UAE to perform engineering tests for local/ regional partners. Our research activities are developed in strong connection with the industry; therefore, in the spirit of generating more robust products, the center is constituted as a network of experts that supports the industry in facing the upcoming challenges. We want to raise the EMC competence within the region and be recognized as a reference in the field.

II. EMC LABORATORY CAPABILITIES

The laboratory offers a large scope of testing for Electromagnetic Interference (EMI) and Electromagnetic Susceptibility (EMS), with a special focus on MIL-STD for subsystem [1] and system [2] testing. Both conducted and radiated tests can be performed using the latest technology equipment. The laboratory consists of 3 chambers: a Semi-Anechoic Chamber (SAC) that can hold large systems, a Pulse Power laboratory (that can be connected to the SAC), and a Low-noise Semi-Anechoic Chamber (Fig.1). A Faraday cage and a reverberation chamber are planned to ensure more flexibility and reduced testing time.

A. EMI – Emission testing

Conducted and radiated emission tests can be performed for different specifications. The antennas, probes, and EMI receivers measure from 2Hz to 40 GHz.

Figure 1. Low-Noise Semi-Anechoic Chamber at TII-DERC.

B. EMS – Immunity testing

For susceptibility testing, in addition to the conducted and radiated immunity (RI) tests, all transient phenomena tests such as High Altitude Electromagnetic Pulse (HEMP), Electrostatic Discharges (ESD), or Lightning EMP are available. The current limits are 250V/m for RI (Fig.2 & Fig.3), 300mA for BCI, 300 kV for ESD, and up to 50kV/m for HEMP.

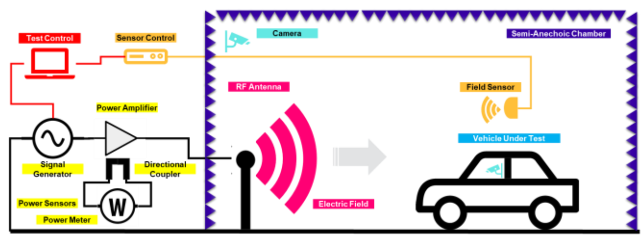

Figure 2. Diagram of the radiated susceptibility vehicle test

Figure 3. Picture of radiated susceptibility vehicle test.

REFERENCES

[1] MIL-STD-461G, "Requirements for the control of electromagnetic interference characteristics of subsystems and equipment", Department of defense interface standard, 2015.
[2] MIL-STD-464C, "Electromagnetic environmental effects requirement for systems", Department of defense interface standard, 2010.

Destruction Scenario of Power Supply Due to Conducted Pulse from HEMP

G. MEJECAZE, L. CUROS, F. PUYBARET
CEA, DAM, CEA-Gramat
F-46500 Gramat, France
guillaume.mejecaze@cea.fr

T. DUBOIS, J.-M. VINASSA
Univ. Bordeaux, CNRS, Bordeaux INP
IMS UMR 5218, F-33400 Talence, France

Abstract— This article presents the effects of a high current conducted pulse, induced by a high-altitude nuclear electromagnetic pulse (NEMP/HEMP) coupling on a global electric power distribution network, on the electrical behavior of a flyback switch-mode power supply. Current and voltage measurements have been performed around each destroyed component during the injection to build a power supply destruction scenario.

Keywords-HEMP; NEMP; Switch-Mode Power Supply (SMPS); component destruction; susceptibility

I. INTRODUCTION

Several studies show that the conducted parasitic current, of hundreds of amperes and voltage of several kilovolts, induced by the coupling of a HEMP on a global electric distribution network, involves the destruction of equipment's power supplies plugged to the grid [1]. Whereas the power supply is impacted first, only few studies deal with the effects of EMP on switch-mode power supplies (SMPS) [2]. Due to the system complexity, only ascertainment of the electronic equipment destruction is done and only few studies propose an analysis of the destruction effects at component level. However, the precise understanding of the mechanisms leading to the SMPS destruction are still insufficient to allow correct prediction and modelling. In this context, a failure scenario of a SMPS has been determined with the understanding of each component failure.

II. EXPERIMENTAL SETUP

A current injection platform gives the possibility to reproduce electrical bi-exponential stresses of several hundreds of amperes (some tens of nanoseconds rise time and hundreds of nanoseconds duration) representative of disturbances induced by the coupling of an HEMP, as defined in the IEC 61000-2-9 standard, on distribution network long cables. After preliminary analyses, a 57 W flyback SMPS, representative of a majority of commonly used power supplies, has been specially designed in order to facilitate the destructions understanding, and manufactured of 100 samples. Its simplified electrical schematic is given in Fig. 1. High current pulse injections have been carried out firstly only in differential mode on the designed power supply. In fact, the interference signal at the SMPS input cannot be considered as a pure common mode signal but also contains a differential mode part due to the contribution of several elements, such as unbalance of SMPS input impedances on phase and neutral.

This study has been carried out with the support of Direction Générale de l'Armement belonging to the French Ministry of the Armed Forces.

III. FAILURE SCENARIO

In order to understand the mechanisms leading to each component failure, current and voltage measurements have been specially performed during the destruction, in "harsh" and noisy environment, with appropriate probes.

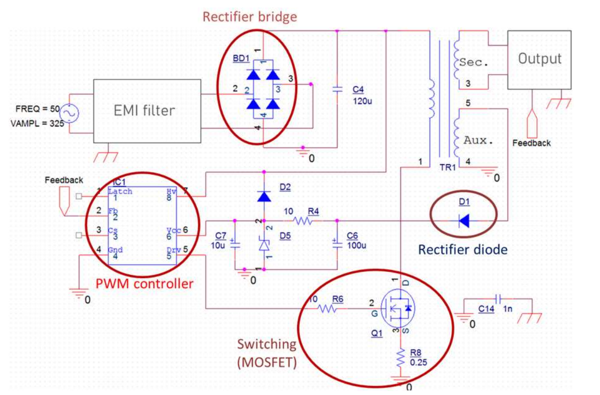

Figure 1. Simplified electronic schematic of the SMPS.

SMPS analyses after their failure have shown that the same components were destroyed due to too high currents of several hundreds of amperes. These components are (circled in Fig. 1): rectifier bridge, MOSFET and its associated resistors, diode of the PWM controller supply and PWM controller. After hundred SMPS destructions, a scenario giving the chronology of the destruction events has been built. The chronology has been determined through current and voltage measurements carried out at different specific nodes during the destruction of the SMPS and by analyzing the datasheet maximum ratings and the destroyed components (using X-rays and optical microscope).

IV. CONCLUSIONS

In this paper, effects of current pulse injection of several hundreds of amperes on a representative flyback SMPS have been studied. It has been observed that four main components were often destroyed and the failure mechanism of each of these components has been explained. Measurements have permitted to build a scenario explaining the SMPS failure through the chronology of destruction events. This scenario is a first step in order to model the susceptibility of power supplies during an electrical pulse injection.

REFERENCES

[1] N. Kularatna, "Powering systems based on complex ICs and the quality of utility AC source: an end to end approach to protection against transients," Proc. of Power Quality, 2005
[2] M. L. Sudheer *et al.*, "Study of conducted susceptibility of power converters," International Conf. on EIC, 1999

Overview of Collaborative Efforts over Several Decades in Pulse Power and Antennas

Ian D. Smith*
Self-Employed Consultant
Oakland, CA 94611, USA
E-mail: iandsmith37@gmail.com

D. V. Giri
Dept. of ECE, University of New Mexico
Pro-Tech, 410 Washington Street, # 1
Wellesley, MA 02481, USA
E-mail: Giri@DVGiri.com

Abstract**—**This paper is submitted for the special session titled SS3: Dave Giri - Life and Legacy. We have collaborated on may projects for US DoD and other agencies. We document some representative projects that we have jointly worked on. The first author's training and work experience is in designing and fabricating state-of-the art pulse power machines. The second author is an expert in applied electromagnetics, designing large electromagnetic facilities such as HEMP E1 simulators. There is also the area of pulser-antenna or pulser-transmission line interfaces. The pulser is not merely a high voltage generator but is to be treated as part of a wave launching system. The two authors' individual expertise has resulted in many successful facilities delivered to sponsors, that became work horses for various US Govt agencies, as well as in western European countries.

Keywords- pulse power, HEMP E1 simulators, Marx driven helical antennas

I. INTRODUCTION

Greetings to the attendees of GLOBALEM2022, from Ian Smith. I am very pleased indeed that GLOBAL EM is honoring the career and times of Dave Giri. My own career has been in the field of pulse-power, which has provided the high-power drive for many of the electromagnetic systems that Dr. Giri has helped to create, and that combination has led to many collaborations with him.

In 1960 I joined the group of Charlie Martin in the UK that launched pulse-power, then I moved to the USA to help its great development. The application of pulse-power to EMP simulators soon brought me into contact with Dave Giri, and I enjoyed collaborations with him that lasted over more than 40 years before I retired in 2014. It is a pleasure to recall some of those collaborations today.

When I went to the USA I joined Physics International Company, and there I built 1.5 MV pulsers to drive the Airforce Weapons Lab's Research EMP Simulators, RES, R, E, S, for short. RES 1A and 1B were long resistively loaded antennas, one horizontal and one vertical, carried aloft by helicopters. Although I knew Dave had contributed to the design of these antennas, I think I did not meet Dave till I supplied a similar pulser called High Altitude Generator 1, or HAG 1, which provided 1.8 MV with a few ns risetime to the ground based HPD, or Horizontally Polarized Dipole antenna, that he was helping design at the Airforce Weapons Lab in Albuquerque. After that I interacted with him at many meetings about other EMP simulator systems he was involved with.

To describe another type of project Dave and I collaborated on, I will jump ahead to the mid-1990s. By then I had left Physics International and co-founded the company Pulse Sciences, Inc., or PSI—the "I" stood for Ian. Dave was instrumental in designing Impulse Radiating Antennas, and PSI built pulsers to drive two of these. The first was a 120 kV, 100 ps risetime pulser driving a transmission line that terminated at a paraboloidal reflector. That could create a 100 ps full-width-half-max impulse with a (range x field) product of 1.2 MV. Then we collaborated on the more powerful JOLT, which was driven by a megavolt and had a corresponding parameter of 6 MV. PSI's pulsers used switches with hydrogen or flowing oil and had repetition rates of hundreds of pulses per second. The Impulse Radiating Antennas were projects of the Air Force Research Lab, as the Airforce Weapons Lab had become known.

Pulse Sciences grew to well over 100 people, and was bought by Titan Corporation, who bought Physics International and placed it under PSI to form Titan Pulse Sciences Division. This was later bought by L3 Communications. Under these ownerships PSI worked with Dave on projects that included in 1998 "VERIFY", a vertically polarized guided-wave EMP simulator driven by 600 kV with a 1 ns risetime, that we exported to Switzerland. They also included a transportable source of high-power microwaves, which were produced at many specific frequencies by spiral antennas designed by Dave and driven by our repetitive 2 MV Marx generator—that was in 2009.

Over these decades, I saw Dave contribute to many other electromagnetic systems, too numerous for me to recall. And I can't address his contributions in other areas, for instance in electromagnetic effects. He was not only a great colleague but a good friend. He and I were big cricket fans; I recall the time we travelled, together with my wife Sheri, to the San Francisco Peninsula to see Sunil Gavaskar, the great Indian batsman, probably the best in the world. He was visiting to play in a local match. It is a great pleasure for me to have a part in the GLOBAL EM session that honors Dave Giri and his splendid career.

Lightning Electromagnetic Fields Computation: An Approach to Reduce the Computational Effort

Daniele Mestriner[1], Massimo Brignone[1], Renato Procopio[1], Martino Nicora[1], Mansueto Rossi[1], Federico Delfino[1], Farhad Rachidi[2] and Marcos Rubinstein[3].

[1]University of Genoa – corresponding author: renato.procopio@unige.it
[2] Ecole Polytechnique Federale de Lausanne (EPFL)
[3] Haute Ecole d'Ingenierie et de Gestion du Canton de Vaud

Abstract—The computation of lightning electromagnetic fields computation usually requires a considerable computational effort if the Channel-Base Current (CBC) realistic waveform and the finite soil conductivity are taken into account. This work proposes a closed-form expression for the radial and vertical electric field and the azimuthal magnetic field generated by a lightning discharge. This is possible thanks to the representation of the CBC expression and of two other suitable functions as Prony series that allow to analytically solve the integrals appearing in the classical field formulas. Since the number of terms required for this approximation is limited, this results in a noteworthy CPU time saving.

Keywords-Lightning, Electromagnetic fields, Computational effort

I. INTRODUCTION

The numerical evaluation of lightning ElectroMagnetic Fields (EMF) using the general field expressions (e.g., [1]) involve numerical integrations, hence, requiring a high computational effort, which could be incompatible with cases where the EMF should be computed at different observation points (e.g., lightning-induced voltages and Lightning Performance (LP) evaluation [2]). This paper proposes an approach, based on the Prony series of some particular functions, that allows to significantly lower the computational effort. The method does not require any assumptions on the CBC and the attenuation function along the channel. The proposed approach has been validated by comparison with the numerical approach [1] and it guarantees an increase in the computational speed of up to 100 times.

II. GENERAL IDEA OF THE METHOD

The lightning magnetic field above an ideal ground expression can be found in [1]. In the proposed approach, we first compute the magnetic field according to the following steps (see [3] for further details). 1) For any model (except the TL one), the channel is discretized into *N* segments; along each segment the attenuation function is considered as constant. 2) After some mathematical manipulations, the magnetic field due to each segment can be expressed in terms of the convolution integral of the CBC and a function y_1 of the time t defined in [3]. 3) the CBC and $y_1(t)$ are expressed by means of their Prony series, which makes the convolution integrals analytically solvable. The radial and vertical components of the electric field can be then computed for a perfectly conducting ground by means of the Maxwell's equations applied to the channel geometry. This implies the discretization of a function $y_2 = ty_1$ by means of its Prony series. Once the radial term of the electric field is computed, the soil conductivity is taken into account by means of the Cooray-Rubinstein formula, suitably converted in the time domain.

III. VALIDATION AND COMPARISON

The proposed approach is compared with the results of a numerical code applied to the equations proposed in [1]. Fig.1 shows the EM fields computed considering an observation point located 200 m far from the lightning strike and placed 10 m above the ground. A typical first stroke is considered and the soil conductivity is 10 mS/m. The channel height is 8 km, while the propagation velocity is the half of the light speed. The MTLE is considered. As can be observed in Fig.1, the two approaches produce the same result. It is important to notice that, in terms of computational time, the proposed approach is more than 50 times faster than the numerical one.

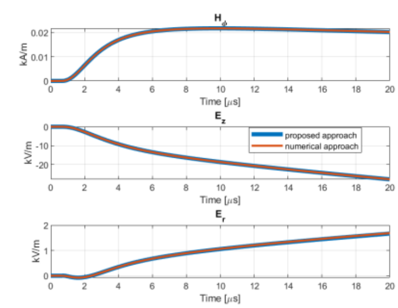

Fig. 1 Comparison between the proposed approach and the numerical one

REFERENCES

[1] F. Rachidi et al. "Influence of a lossy ground on lightning-induced voltages on overhead lines." IEEE Transactions on Electromagnetic Compatibility 38.3 (1996): 250-264.

[2] M. Brignone et al. "Evaluation of power system lightning performance, part i: Model and numerical solution using the pscad-emtdc platform." IEEE Transactions on Electromagnetic Compatibility 59.1 (2016): 137-145.

[3] M. Brignone et al. "A Prony-Based Approach for Accelerating the Lightning Electromagnetic Fields Computation above a Perfectly Conducting Ground." Electric Power Systems Research 209 (2022): 108013.

Use of Reconfigurable Intelligent Surfaces to Modify the Statistical Electromagnetic Properties of Complex Enclosures

Jingnan Cai, Thomas M. Antonsen, Steven M. Anlage
Physics and ECE Departments
University of Maryland
College Park, MD 20742 USA

Abstract— Electromagnetic environments are becoming increasingly complex and congested, creating a growing challenge for electronics that are susceptible to electromagnetic aggression, particularly in reverberant environments. The use of reconfigurable intelligent surfaces (RIS) provides a potential means of re-directing and re-distributing waves to protect sensitive electronic components in such environments. We have developed several approaches that utilize RIS to modify the electromagnetic fields inside reverberant enclosures for the purpose of taming these fields and protecting sensitive components inside. Examples include the use of RIS to create cold spots at locations inside the cavity where a minimal amount of energy is delivered in a given frequency band. We have also used RIS to create coherent perfect absorption (CPA), and the complementary anti-CPA state. CPA (anti-CPA) is a condition under which all (a minimal amount of) radiation incident on an enclosure is absorbed inside the enclosure. The RIS can be programmed to achieve these conditions using a variety of algorithms and machine learning (ML) methods. In general, we demonstrate that ML proves to be remarkably adept at creating desired scattering properties in the complex enclosure. We have also utilized a nonlinear RIS to actively translate deleterious waves to new frequencies where their effects on sensitive electronics can be minimized. Our technique is enabled by the reverberant nature of the cavity, and is effective with an RIS that covers only about 1.5% of the total cavity surface area.

Keywords-Electromagnetic statistics, reconfigurable intelligent surface, machine learning.

I. INTRODUCTION

We are concerned with the problem of high-power microwave signals disrupting the operation of sensitive electronics located inside complex reverberant environments. Our approach to this problem is to use reconfigurable intelligent surfaces (RIS) embedded within to modify the statistics of electromagnetic waves in the enclosure. The RIS is made up of individually programmable pixels whose normal-incidence reflection phase can be digitally toggled between values of approximately 0 and π in a given frequency range. Our RIS has 240 such pixels, and can significantly modify the fields and scattering properties despite covering only 1.5% of the surface area of the enclosure.

II. RIS PROGRAMMING AND PERFORMANCE

Several algorithms have been developed to set the RIS pixels to achieve desired properties inside the enclosure. One such algorithm uses a modified steepest descent method to create cold spots and CPA/anti-CPA states in desired frequency ranges [1]. A ML algorithm was also developed to predict the pixel settings of the RIS required to achieve a given scattering profile $S_{21}(f)$ from 3 to 4 GHz inside a complex reverberant enclosure [2]. The ML algorithm was successful at identifying the correct pixel settings 97.7% of the time, and the remaining errors were mainly confined to mis-identifying the state of just one pixel. These algorithms were extensively tested experimentally in a reverberant scattering setting in the microwave frequency range.

III. NONLINEAR RIS

A new nonlinear RIS has been developed to establish new types of control over the reverberant fields. The pixels are made up of square resonant patches that are loaded with 4 varactor diodes. Under global voltage bias, the patches change their resonant frequency, and reflection phase shift, over the 3-4 GHz band. This unique RIS can be used to alter the statistical properties of the enclosure, in part by varying the loss parameter of the enclosure, as described by the Random Coupling Model (RCM) [3]. The RIS can also translate the frequencies of signals reverberating in the enclosure, effectively sequestering highly energetic signals from resonant absorption in sensitive electronics. We shall review the experimental demonstration of the nonlinear RIS and describe its effects on the statistical electromagnetic properties of complex enclosures.

REFERENCES

[1] Benjamin W. Frazier, Thomas M. Antonsen, Jr., Steven M. Anlage, and Edward Ott, "Wavefront Shaping with a Tunable Metasurface: Creating Coldspots and Coherent Perfect Absorption at Arbitrary Frequencies," Phys. Rev. Research 2, 043422 (2020).
[2] Benjamin W. Frazier, Thomas M. Antonsen, Steven M. Anlage, Edward Ott, "Deep-learning estimation of complex reverberant wave fields with a programmable metasurface," Phys. Rev. Applied, 17, 024027 (2022).
[3] G. Gradoni, J.-H. Yeh, B. Xiao, T. M. Antonsen, S. M. Anlage, E. Ott , "Predicting the statistics of wave transport through chaotic cavities by the Random Coupling Model: a review and recent progress," Wave Motion 51, 606-621 (2014).

This work is supported by ONR under Grant No. N000141912481, and DARPA under Grant HR00112120021.

Coupling of Microwave Pulses to Complex Enclosures: Analytical and Numerical Modeling and Experiments

Jared Erb, Thomas M. Antonsen, Steven M. Anlage
Physics and ECE Departments
University of Maryland
College Park, MD 20742 USA

Zhen Peng
ECE Department
University of Illinois at Urbana-Champaign
Urbana, IL 61801 USA

Abstract—Our objective is to understand the coupling of pulsed high-frequency radiation into complex structures through one or more routes of ingress, and to predict the induced voltages on objects located inside the enclosure. The deterministic study of such scenarios is usually computationally expensive and incapable of capturing the extreme sensitivity to scattering details. We develop a hybrid computational and statistical model to understand coupling and reverberation of the wave energy that dwells inside a complex enclosure. The model assumes minimal information about the enclosure, in the same spirit as the Random Coupling Model (RCM), which has found great success in providing a statistical characterization for wave chaotic systems in the frequency domain. The computational approach captures the details of the incident waves and coupling effects, and combines it with a stochastic Green's function approach to predict the wave distributions inside the enclosure. In addition, the RCM can be transformed into the time-domain and generalized to include early-time short-orbit transmission path effects between the ports, and the inclusion of arbitrary nonlinear or time-varying port load impedances. We have conducted short-pulse time-domain illumination experiments on a variety of wave chaotic enclosures with different types of aperture coupling. We compare the results of the hybrid model to the experimental data and generally find good agreement.

Keywords-Electromagnetic coupling, Random Coupling Model, Time-domain measurements.

I. INTRODUCTION

The Random Coupling Model (RCM) has successfully treated the statistical electromagnetic properties of complex enclosures in the short-wavelength limit [1]. It has been extended to treat the effects of short orbits between ports [2], and the effects of finite radiation efficiency of the ports [3], as examples. We are now concerned with the question of how radiation couples into complex enclosures through a variety of apertures, and then how that radiation reverberates and delivers energy to ports inside the enclosure. Sensitive electronic components inside the enclosure can be treated as one such port.

This work is supported by ONR under Grant Nos. N000141912481, N000142012835, and DARPA under Grant HR00112120021.

II. HYBRID RCM / STOCHASITC GREENS FUNCTION MODEL

Our approach is to join a numerical treatment of pulsed wave energy impinging on the enclosure and finding its way through apertures, with a stochastic Green function numerical model [4] for fields inside the enclosure that is inspired by the RCM. At its heart, our hybrid approach integrates full wave, high fidelity solutions of subsystems (i.e. apertures and electronics of interest) occupying portions of the domain [5], with the RCM effectively simulating the large volume separating the fully-modeled subsystems.

III. EXPERIMENTS

Experiments have been carried out both in the frequency domain and time domain. A broadband horn antenna is used to illuminate various structures, and a short-dipole measurement port is located inside the enclosure. Frequency domain 2-port S-parameter measurements are performed with a network analyzer. A time-domain version of the same experiment is also performed with an arbitrary waveform generator attached to the antenna and an oscilloscope attached to the short dipole.

We compare statistical properties of induced voltages in the target dipole in both the frequency and time domains.

REFERENCES

[1] G. Gradoni, J.-H. Yeh, B. Xiao, T. M. Antonsen, S. M. Anlage, E. Ott , "Predicting the statistics of wave transport through chaotic cavities by the Random Coupling Model: a review and recent progress," Wave Motion 51, 606-621 (2014).
[2] J. A. Hart, T. M. Antonsen, E. Ott, "The effect of short ray trajectories on the scattering statistics of wave chaotic systems," Phys. Rev. E 80, 041109 (2009).
[3] B. Xiao, T. M. Antonsen, E. Ott, Z. B. Drikas, J. Gil Gil, and S. M. Anlage, "Revealing underlying universal wave fluctuations in a scaled ray-chaotic cavity with remote injection," Phys. Rev. E 97, 062220 (2018).
[4] S. Lin, Z. Peng, and T. M. Antonsen, "A Stochastic Green's Function for Solution of Wave Propagation in Wave-Chaotic Environments," IEEE Trans. Antenn. Propag. 68 (5), 3919-3933, 2020.
[5] Z. Peng, Y. Shao, H.-W. Gao, S. Wang and S. Lin, "High-Fidelity, High-Performance Computational Algorithms for Intrasystem Electromagnetic Interference Analysis of IC and Electronics," IEEE Trans. Components, Packaging and Manufacturing Technology 7, (5), pp. 653-668, May 2017.

Simulating an Open Coaxial Return Line in a Reverberation Chamber

Alexander Schoisl, Dr. Markus Rothenhäusler
Airbus Defence and Space, Germany
85077 Manching, Germany
alexander.schoisl@airbus.com

Martin Schwarz
WTD 81, EMV/EME (410)
91171 Greding
martin2schwarz@bundeswehr.org

Abstract—Standardized electromagnetic susceptibility testing for airworthiness qualification according to RTCA DO-160 demands coverage of the frequency range from 10 kHz up to 18 GHz. The Direct Current Mode Stirred (DCMS) test method, which combines Direct Current Injection (DCI)/ High Level Direct Drive (HLDD) with the resonant properties of a Reverberation Chamber (RC), aims at fulfilling the high field level requirements for the whole frequency range. In order to establish the DCMS method as a standardized EMC test, a conversion method between injected power into the Equipment under Test (EUT) and equivalent external field strength is needed. Therefore, a measurement campaign including several test sites and EUTs, supported by numerical simulations, is conducted to provide reliable measurement data and simulation models for corroborating a potential conversion theorem in the future.

Reverberation Chamber; DCMS; DCI; HLDD

I. INTRODUCTION

The DCI method works particularly well in the low kHz frequency range up to some hundred MHz [1] by utilizing the surface conductivity of an EUT and directly injecting the interfering current that would normally be induced by the external field in a HIRF test. To match the generators wave impedance, the EUT must be clamped in a return line. With increasing frequency, the return line starts to radiate due to increasing electrical length. By placing the EUT in a RC this normally lost energy can be utilized as a radiation source for stirred RC operation. To further improve the confidence in this so called DCMS method as an EMC test an ongoing study provides measurement results from different RC test sites with multiple EUTs, which are compared to their corresponding numerical simulations.

II. MEASUREMENT AND SIMULATION SETUP

Fig. 1 shows the setup for one of the RC test sites. Inside an Open Coaxial Return Rig (OCRR) a generic missile (GENEC) is clamped in as EUT and everything is placed within the test volume of the RC. Inside the GENEC two electric field probes and an Electronic Explosive Device (EED) with an attached fiber optic temperature sensor, to monitor the EED's current, is located. The RC is operated in DCI, DCMS and RC mode as described in [2].

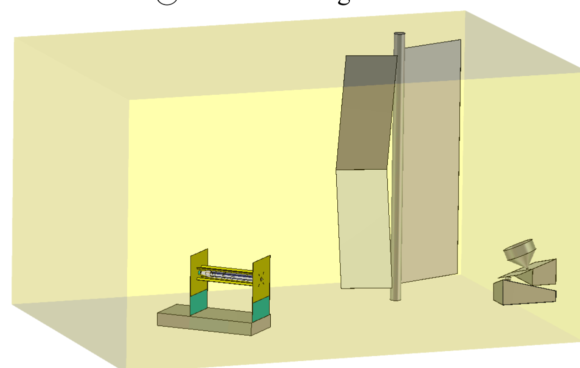

Figure 1. Reverberation chamber setup with GENEC

Those measurements are conducted on four RC test sites with different dimensions to validate the results.

Numerical simulations have been conducted with the software FEKO and its MLFMM solver in the past, but the resulting electric field strength results showed dependencies on the mesh density [3]. In this study Dassault Systemes CST Studio Suite with its frequency domain solver is used for the frequency range up to 1 GHz. Of interest for the comparison with the measurement results are mainly the frequency dependent current maximas through the EED and the electric field strength over frequency inside the GENEC for DCI, DCMS and RC operation. Furthermore, for RC operation, the external electric field strength inside the chamber's test volume has to comply to the homogeneity requirements defined in DIN EN 61000-4-21.

III. RESULTS

First simulation results were used to iteratively improve the simulation model, the final version is in good agreement with the measurement results regarding external and internal electric field strength. The precise modelling of the EED wiring turned out to be a major challenge.

Appreciation goes to the German Customer WTD81 Greding GF410, who enabled this project as a Technology Demonstration.

REFERENCES

[1] EUROCAE ED-107A/SAE ARP5583A; July 2010, pp. 58-72.
[2] M. Rothenhäusler, "Direct Current Mode Stirred – A new Susceptibility Test Method for EMC and HPEM", AMEREM 2018
[3] M. Rothenhäusler, A. Schoisl and M. Schwarz, "Numerical Simulation of a Direct Current Mode Stirred Reverberation Chamber, EMC EUROPE, 2019, pp. 247-252

The “Arreghini’s Problem” challenge

One of my numerous interactions with Dave Giri

Jean-Philippe Parmantier, I. Junqua, S. Bertuol
ONERA/DEMR, Université de Toulouse,
F-31055 Toulouse - France
jean-philippe.parmantier@onera.fr

Abstract—This paper will introduce the Arreghini-problem proposed by Dave Giri to validate Multiconductor Transmission Line Networks (MTLN) solvers. The topology of the problem together with its analytical solution are presented. Then various evolutions are showed to demonstrate recent evolutions on Current-Return-Networks (CRN) and Field-to-Transmission-Lines (FTL) problems. Finally, complex applications of such problems, made possible by those modified Arreghini’s problems, are illustrated.

Keywords - EM-Topology, MTLN, BLT equation

I. INTRODUCTION

My interactions on EM with Dave Giri have been numerous since I have been knowing him and since I began to present my results in conferences. While I progressively became one of Carl Baum’s “protégés” as he used to say it, I also began having interactions with Dave Giri and progressively we became friends. Particularly, I had the chance to be invited in the academy of the HPE-courses, which offered me the opportunity of having so many fructuous scientific exchanges with Dave and brilliant scientists.

In the HPE courses, I taught EM Topology and MTLNs, both of them illustrated by a demo with the BLT-based MTLN CRIPTE code. It happens that in the 2007-Bonascre, France, edition (close to Toulouse), Dave challenged me with a problem that he had solved several years before for one of his former EMP-course (the former name of HPE-courses) student. This student was named, “Franck Arreghini” and without any intentional purpose, this name eventually became famous in many of my activities. Mr. Arreghini’s problem is presented in Figure 1, formulated by Dave Giri’s hand himself. On my side, it became Arreghini’s challenge, exactly formulated as follows by Dave:

- “*Goal: compute currents and voltages in time domain”*
- *Purpose: do the problem analytically, so that time domain computer codes can be tested in special simple cases*”

II. ANALYTICAL RESOLUTION

The problem is indeed very simple in terms of application case but its resolution requires a non-negligible amount of mathematical development that must be done with care in order to establish the exact solution. This development also shows why MTLN computer tools become unavoidable as soon as the topology of the problem becomes slightly more complex (more branches, more wires in branches, cable-shields, various positions and distributions of sources), not to mention physical properties of the wiring (frequency dependence, losses..) or EM-coupling physics (FTL, CRN…).

However, Arreghini’s problem is of real interest for MTLN computer code validations because of its branched topology involving transmission-lines and junctions. As far as frequency domain solvers are concerned, such as CRIPTE, the time-domain voltage excitation becomes a specific challenge that requires appropriate signal processing based on well-dimensioned Fourier Transform operations.

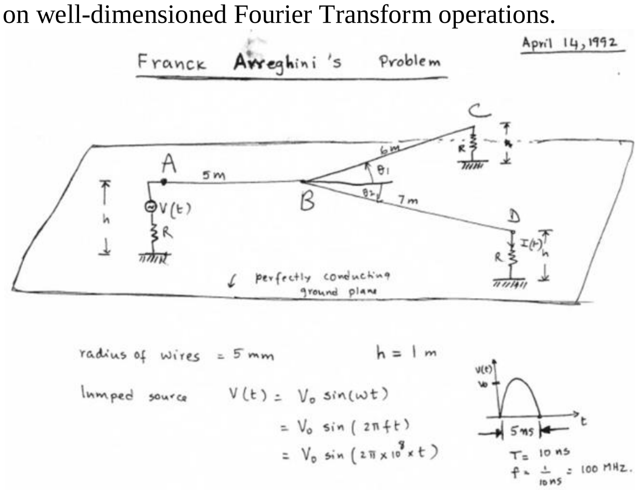

Figure 1. Arreghini’s problem description by Dave Giri’s hand.

II. AREGHINI’S TEST-CASE OFFSPRING

The Arreghini’s problem topology has finally provided the validation for many improvements that we have made in the last 10 years in the CRIPTE code. This will be illustrated with complex CRN [1, 2] and FTL [2, 3] problems.

REFERENCES

[1] I. Junqua, J-P. Parmantier, D. Prost, « Modelling Common Mode Impedances for Lightning Indirect Effects on Multiconductor Cables into Composite Aircraft Equipped, with Current Return Networks » Proc. of 2015 International Conference on Lightning and Static Electricity (Toulouse, France)

[2] J-P. Parmantier, I Junqua, S. Bertuol, T. Volpert, W. Dyab, Ahmed Sakr, Ke Wu, C. Girard, G. Prin, A. Guidoni, G. Samarone, F. Moupfouma, W. Tse, K. Nuyten and A. Blommers “Modelling EM-Coupling on a Massively Composite Aircraft Barrel”, Book of abstracts of ASIAEM 2018, Santa Barbara 2018

[3] J-P. Parmantier, C. Guiffaut, D. Roissé, C. Girard, F. Terrade, S. Bertuol, I. Junqua, A. Reineix “Modelling EM-Coupling on Electrical Cable-Bundles with a Frequency-Domain Field-to-Transmission Line Model Based on Total Electric Fields”, Advanced Electromagnetics,vol. 9, n°. 3, December 2020, pp. 15-31.

The Definition of the Rise Time of Impulse Signals

Carlos Romero[1], Marcos Rubinstein[2], Farhad Rachidi[3]
[1] Armasuisse Science and Technology, Thun, Swizerland, carlos.romero@ar.admin.ch
[2] University of Applied Science of Western Switzerland, Yverdon-les-Bains, Switzerland, marcos.rubinstein@heig-vd.ch
[3] EPFL, Lausanne, Switzerland, farhad.rachidi@epfl.ch

Abstract**—**We present in this paper an example of the numerous contributions made by Dr. Dave Giri in the field of high power electromagnetics that have found applications in other fields. Specifically, we discuss how his definition of the risetime has been applied to lightning-originated waveforms.

Keywords-lightning; signal risetime.

I. INTRODUCTION

The risetime of the lightning current and of electromagnetic fields is an important parameter in the context of electromagnetic compatibility since it responsible for induced voltages and thus for disturbance and damage to circuits and systems. However, the definition of the risetime is not unique and difference methods to measure it are used in different fields. In this abstract, we describe two of the methods. One of them, commonly used in the Nuclear Electromagnetic Pulse and the High-Power Electromagnetics research fields, was proposed by Carl Baum and Dave Giri ([1-3]). The other is widely used in the lightning field and in standards and it is defined based on the instants at which the waveform in question crosses thresholds defined as percentages of the peak value.

II. Risetime definitions

A. The 10% to 90% risetime or $t_{10\text{-}90}$ risetime

The $t_{10\text{-}90}$ risetime is defined as the time between the instant at which a waveform reaches 10% of its peak and the time at which it reaches 90% of its peak (see [4]). In spite of its simplicity, the $t_{10\text{-}90}$ risetime is not generally applicable since some waveforms exhibit an oscillatory behavior during the rising part that makes the 10% and 90% thresholds be crossed more than once.

B. The rate-of-rise risetime

An alternative definition of the risetime was proposed by Carlo Baum and Dave Giri and it is commonly used in the Nuclear Electromagnetic Pulse and the High-Power Electromagnetics research fields [1-3]. The definition is given in terms of the maximum rate of rise of the waveform. It is given in Eq. (1).

$$t_{mr} = \frac{i_{peak}}{\left(\frac{di}{dt}\right)_{peak}} \qquad (1)$$

Fig. 1 shows an example of a measured lightning current waveform at the Säntis tower characterized by a complex early-time behaviour to which the two definitions for the risetime were Applied. The application of Eq. (1) results in a risetime of 0.3 µs, while the use of the $t_{10\text{-}90}$ definition yields a risetime of 0.7 µs.

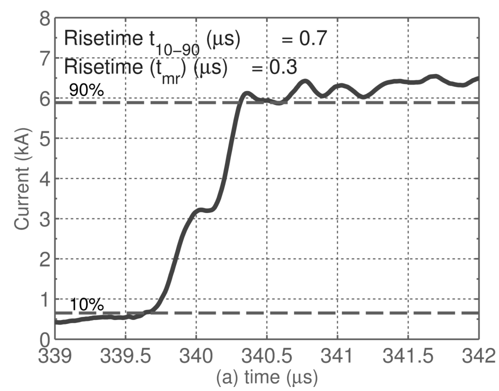

Fig. 1. The use of the two definitions for the determination of the risetime: application to a measured lightning current waveform at the Säntis tower (adapted from [5]).

It was observed [5] that the t_{mr} risetime is in general more consistent with the maximum frequency content of the signals and the probability distributions are more consistent with the expected lognormal distributions.

REFERENCES

[1] C. E. Baum, "Some Considerations Concerning Analytic EMP Criteria Waveforms," *Theoretical Notes,* vol. Note 285 (www.ece.unm.edu/summa/notes), 1976.

[2] D. V. Giri, W. D. Prather, and C. E. Baum, "The Relationship Between NEMP Standards and Simulator Performance Specifications," *Sensor and Simulation Notes,* vol. Note 538 (www.ece.unm.edu/summa/notes), 2009.

[3] D. V. Giri, "Effective Rise Time Resulting from a Convolution of Waveforms with Exponential and Gaussian Rise Characteristics," *Measurement Notes* vol. Note 33 (www.ece.unm.edu/summa/notes), 1987.

[4] R. B. Andersson and A. J. Eriksson, "Lightning parameters for engineering application," Electra, vol. 69, pp. 65-102, 1980.

[5] C. Romero, M. Paolone, F. Rachidi, M. Rubinstein, D. Pavanello and D. V. Giri, "A statistical analysis on the risetime of lightning current pulses in negative upward flashes measured at Säntis tower," 2012 International Conference on Lightning Protection (ICLP), 2012, pp. 1-5, doi: 10.1109/ICLP.2012.6344272.

A Review of High-Power Fiber Laser in Industry

Asma Al Ahmadi , Romain Baudoin, Giuseppe Scurria, Jawaher Al Ameri, Reem Al Ameri, Taif Al Hmoudi, Amit Dubey, Guillaume Matras, Chaouki Kasmi
Directed Energy Research Centre
Technology Innovation Institute
Abu Dhabi, United Arab Emirates
Asma.AlAhmadi@tii.ae

***Abstract*—** High power laser systems have evolved dramatically over the years contributing to the development of new technologies in manufacturing and material processing, communication, and medicine. High Power Fiber Laser (HPFL) is a special type of laser which uses silica fiber doped with rare earth element as an active medium for light amplification. The various geometries of fiber, along with the highly directed beam and wavelength range offers a wide range of possible new industrial opportunities which makes fiber laser research an interest of the Directed Energy Research Centre (DERC) at Technology Innovation Institute (TII). The aim of this research at DERC is to obtain state of the art outputs power emitting in the near infrared range using Yb and Tm doped fibers which provides highest output power among rare-earth elements. This paper will review high power lasers in industry, high power fiber laser application and configuration. In addition to state-of-the-art facilities of DERC for fiber processing showing results and future work.

Keywords: High power, Fiber laser, beam quality, splicing

I. REVIEW OF INDUSTRIAL HIGH POWER LASER

High energy lasers played a critical role in the development of new industrial technologies including material processing like cutting, welding, drilling, and marking different materials for manufacturing purposes. The primary high power lasers used in material processing are CO_2 emitting at 10.6 µm, thin disc emitting at 1.03 µm, and fiber lasers emitting at 1-2 µm operating in both continuous mode, where a continuous beam is emitted, and pulsed mode where a highly intense pulse of laser is emitted. The shorter wavelength of thin disc and fiber laser gives them advantage over the CO_2 since shorter wavelength result in higher absorption in metals and higher wall-plug efficiency [1]. On the other hand, fiber lasers produce a higher beam quality and efficiency compared to thin disc because of its geometry. In addition, fiber laser introduces a more compact and robust design compared to the complex and costly free space design of thin disc laser [2].

II. REVIEW OF HIGH-POWER FIBER LASER

Fiber lasers offers an integrated system with high quality and robustness maintaining lower cost compared to other types of lasers. Fiber lasers are considered solid state lasers where the core of the fiber is doped with rare earth elements and pumped with laser diodes. The interest of this conference paper is Yb doped fibers at 1 µm wavelength which are popular in material processing industry and Tm doped fibers at 2 µm wavelength which are popular for soft tissue surgery, eye surgery and lithotripsy [3]. The system component consists of different architectures of an active fiber as the gain medium, laser diodes as pumping source, Fiber Bragg Gratings (FBG) as reflectors, combiners to combine the pump laser.

III. FIBER PROCESSING STATE OF THE ART FACILITIES

The aim of this research at DERC is to realize two all fiber laser platforms in a Master Oscillator Power Amplifier (MOPA) configuration which consists of two parts one for producing the beam and the second to amplify the beam using optical devices that are fiber based. In order to build an all fiber system, state of the art fiber processing system have been selected which is based on fusion splicing using CO_2 laser, graphite filament, and arc discharge heating sources providing high precision splices and low loss. Along with splicing the product series is designed to perform other several tasks including stripping, cleaning, cleaving, recoating, and proof testing. The goal is to adjust the processing system parameters to achieve high quality splices then test the quality with splice active monitoring system which uses a low power laser diode to test active and passive fibers output power before and after splicing.

REFERENCES

[1] B. Schmidt, M. Schaefer, “Advanced industrial laser systems and applications “ , *SPIE Digital Library* , volume :10525, pages:1052502, Feb 15, 2018. Accessed: Jun. 6, 2022. doi: 10.1117/12.2299534.
[2] Stefan Ruppik, Frank Becker, Frank-peter Grundmann, Wolfram Rath, Ulrich Hefter,” High-power disk and fiber lasers: a performance comparison “ , *SPIE Digital Library,* volume : 8235 , pages : 149-163, Feb 9, 2012. Accessed: Jun. 6, 2022. doi:10.1117/12.913286.
[3] Sen, Ranjan & Saha, Maitreyee & Das Chowdhury, Sourav & Shekhar, N.K. & Pal, Debasis & Ghosh, Aditi & Dhar, Anirban & Pal, Atasi & Pal, Mrinmay, “HIGH POWER FIBER LASERS: FUNDAMENTALS TO APPLICATIONS”, *ResearchGate Science and culture*. December 2015. 81. 319-326.

Electromagnetic Fields in and around an Enclosure for HEMP E1 Excitation

D. V. Giri
Pro-Tech, Wellesley, MA 02481, USA
Dept. of ECE, Univ. of New Mexico,
Albuquerque, NM USA
E-mail: Giri@DVGiri.com

F. M. Tesche
EMConsultant
Lakeville, CT , USA
E-mail: Fred@Tesche.com

Abstract— *In this paper, results of a numerical study of the shielding of a screen room is conducted and presented. Several movies illustrating the behavior of the transient E-field in and around the shielded room due to an incident HEMP-E1 pulse are produced and the global shielding behavior of the enclosure is summarized using cumulative probability distributions.*

Keywords- EM shielding, enclosures, numerical study, fields in enclosures

I. INTRODUCTION

Shielding is an important consideration in the design of a system, which is to be protected against the unwanted effects of electromagnetic (EM) fields. via currents flowing on penetrating conductors. In general, these conductive penetrations arise from the telephone, communications, power, and other non- electrical conductors. In addition to these penetrations, there are several apertures (holes) in the facility enclosure (e.g., the entrances of the facility), and EM fields may penetrate the interior at these points. Finally, EM field diffusion through the facility walls and roof is a possibility. The above three fundamental ways by which external EM energy can penetrate facilities can be characterized by the acronym ***CAD*** as follows:
C → Conductive penetrations A→ Aperture coupling, and D → Diffusive coupling.

II. ENCLOSURE GEOMETRY AND EXCITATION

In this section, we will be interested in the EM fields inside and outside the enclosure shown in Figure 1. We model the entry door into the facility and will illustrate the effects of EM fields passing into the door. The incident angles are represented by using the angles θ and ϕ in the spherical coordinate system. It should be noted that these angles specify the direction from which the incident field arrives.
A vertically polarized excitation field is considered here. Using the FDTD code , a model of the enclosure was developed. The enclosure was located in a computational grid of maximum dimensions (x, y, z) = (121, 121, 60), which yields a total of 5.27 million unknown E and H field components that must be determined in each time step. The mesh dimensions for this model were Δx = 7.2 cm, Δy = 8.8 cm and Δz = 8 cm, and the resulting time step was Δt = 0.14 ns. Typical computation times were on the order of 3 minutes for 500 time points.

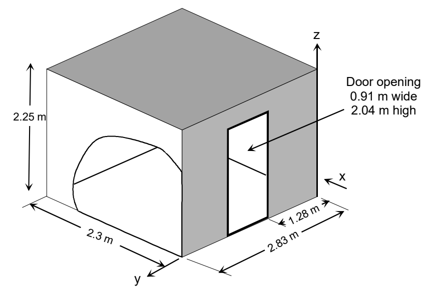

Figure 1. Cut-away diagram of a shielded room, showing an empty interior

We will assume that the incident field arises from a HEMP-E1 and has the form

$$E(t) := Eo\cdot\left[e^{-a\cdot(t-ts)} - e^{-b\cdot(t-ts)}\right]\cdot G\cdot\Phi(t-ts) \quad (1)$$

where the waveform parameters are E_o = 60 (kV/m), G = 1.2 a = 3.75 x 10^7 (1/s), b = 8.46 x 10^8 (1/s).

For the case of $\theta = 90^o$ and $\phi = 180^o$. (Door open) Figure 2 presents a surface plot of the total E-field at a time *t* = 15.56 ns in a 4x5 meter section of the 1-meter-high plane for the facility. In this plot it is easy to see the outline of the shielded enclosure and the location of the front door. At this time, the incident HEMP field has already swept across the facility, and only a remnant of the waveform tail is evident at the far end (x = 4) of the plot.

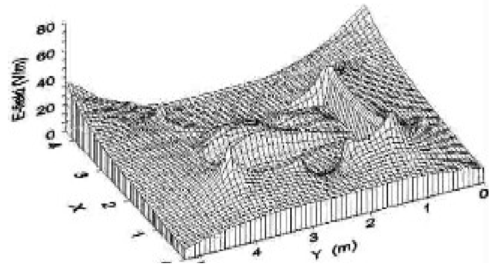

Figure 2. Surface plot of the total E-field in a 4 x 5-meter plane at a height of 1-meter over the ground for the facility and HEMP E1 excitation, at a time *t* = 15.56 ns.

Several such computations and cumulative probability distributions have been computed and will be presented.

Random Coupling Model for Wave-Chaotic Cavity with Aperture Excitation

Hong Soo Park and Sun K. Hong
School of Electronic engineering
Soongsil University
Seoul 06978, Republic of Korea
hosu0202@soongsil.ac.kr; shong215@ssu.ac.kr

Woosang Lee and Jin Soo Choi
Agency for Defense Development
Daejeon, Republic of Korea

***Abstract*—** For statistical prediction of electromagnetic (EM) coupling in the wave-chaotic cavity, the random coupling model (RCM) has been utilized. RCM can also be a useful tool for practical applications such as cavity with aperture excitation, but there are limited experimental verifications. Here, we present a method for predicting the statistical properties and induced voltage in a wave-chaotic cavity where an EM wave is incident through an aperture. Utilizing the aperture impedance based on transmission line theory, the effectiveness of the proposed approach is demonstrated via measurement.

Keywords-HPEM, EMC, random coupling model, wave-chaos, aperture excitation

I. INTRODUCTION

In recent years, the random coupling model (RCM) has received considerable interest in the field of electromagnetic compatibility and high-power electromagnetics in that it can predict the statistical properties of waves inside electrically large cavities in the short-wavelength regime based on wave-chaos [1]. By utilizing the impedance and scattering parameters of cavities and ports, RCM provides statistical predictions of electromagnetic (EM) coupling effects on the target of interest [2].

However, in order to employ RCM in a broader range of applications, it is desirable to predict coupling effects in a more practical environment where the input power is incident through the aperture. Hence, we present an extended RCM for predicting statistical properties and induced voltage in a wave-chaotic cavity with aperture excitation. The proposed concept can be demonstrated using a scattering matrix derived from the aperture impedance.

II. RCM WITH APERTURE EXCITATION

Figure 1 illustrates the experimental setup and general idea of RCM prediction in a wave-chaotic cavity for an incident EM wave from external radiation through an aperture. The cavity (1.2 m × 1.2 m× 0.7 m) is composed of a rectangular aperture (0.2 m × 0.15 m), a target (receive antenna), and a mode stirrer (generating 200 different sets of ray trajectories). With the aperture, our experimental investigation involves two-stages: stage 1) the free-space propagation stage where the wave is incident on the aperture of the cavity, and stage 2) the cavity propagation stage where the incident wave undergoes ray-chaotic propagation and couples to target with the loss parameter α.

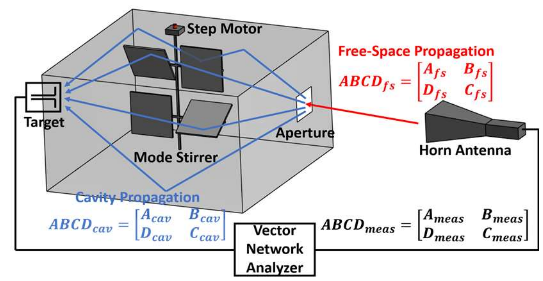

$$\boldsymbol{ABCD_{cav} = ABCD_{fs}{}^{-1} * ABCD_{meas}}$$

Figure 1. Illustration of the experimental setup and ABCD parameters for each stage based on the proposed approach.

Here, the purpose is to predict only the statistical properties inside the cavity using the RCM by obtaining α. To this end, α should be determined using the scattering matrix in the stage 2, but the measurement provides the scattering matrix between the transmit horn antenna and the target, which includes both stages. Hence, our proposed approach is to obtain the ABCD parameter of the stage 1 ($ABCD_{fs}$) through theoretical derivation, and then calculate the ABCD parameter of the stage 2 ($ABCD_{cav}$) through matrix operation with the converted ABDC matrix from the measured scattering parameter ($ABCD_{meas}$). Since the surface of the aperture can be represented as a transmission line, the aperture impedance and the resulting $ABCD_{fs}$ are calculated through transmission line theory [3].

III. CONCLUSION

A method for predicting the EM coupling in a wave-chaotic cavity through aperture excitation is proposed. By utilizing the aperture impedance, the statistical properties inside the cavity can be predicted using RCM even for the coupling of incident power entered through an aperture. Further development of impedance analysis for other aperture shapes can expand the scope of the proposed RCM approach.

REFERENCES

[1] Z. B. Drikas, et al. "Application of the random coupling model to electromagnetic statistics in complex enclosures," *IEEE Trans. Electromagn. Compat.*, vol. 56, no. 6, pp. 1480–1487, Dec. 2014.
[2] J. G. Gil, et al. "Prediction of induced voltages on ports in complex, three-dimensional enclosures with apertures, using the random coupling model," *IEEE Trans. Electromagn. Compat.*, vol. 58, no. 5, pp. 1535–1540, Oct. 2016.
[3] C. Hao and D. Li, "Simplified model of shielding effectiveness of a cavity with apertures on different sides" *IEEE Trans. Electromagn. Compat.*, vol. 56, no. 2, pp. 335–342, Apr. 2014.

Lightning response of distribution lines equipped with shield wires and surge arrester

A. Borghetti, F. Napolitano, C. A. Nucci, F. Tossani
Dept. of Electrical, Electronic and Information Engineering
University of Bologna, Bologna, Italy
alberto.borghetti@unibo.it

K. Ishimoto
Electric Power Engineering Research Laboratory
CRIEPI
Yokosuka, Japan
ishimoto@criepi.denken.or.jp

Abstract**—** Lightning-originated overvoltages are a major cause of outages in distribution lines. In medium-voltage distribution lines equipped with a periodically grounded shield wire and surge arresters, lightning outages associated with indirect lightning are less frequent than those associated with direct ones. Recent analysis concerning medium voltage lines equipped with a shield wire shows that the electromagnetic pulse radiated from the channel may enhance the overvoltage across insulators during direct strikes. This contribution is aimed at further discussing this aspect.

Keywords – LEMP lightning electro-magnetic pulse, distribution lines; lightning protection; direct lightning, grounding

I. Introduction

Flashovers on medium-voltage distribution lines due to lightning activity are caused by indirect and direct strikes. For the assessment of the direct lightning performance, circuit-theory-based electromagnetic transient programs, such as EMTP or ATP, are widely used. In these calculations, a direct lightning strike on a distribution line is typically represented by a lumped-current source in parallel with a resistance, and the influence of electromagnetic field associated with the return-stroke current, namely the lightning electromagnetic pulse LEMP, is typically disregarded. However, according to recent studies, e.g. [1], overvoltages induced by the LEMP may significantly affect the direct lightning performance of some type of MV distribution lines, with specific reference to those equipped with a shield wire. The conclusions of the analysis are supported by the close agreement between the results obtained by means of two different approaches: the three-dimensional finite difference time domain (3D-FDTD) method [2] and the LIOV-EMTP code [3].

II. Content of the paper

Figure 1 shows the overvoltages due to a first stroke in a line equipped with surge arrester installed every 200 m calculated with the 3D-FDTD and with the LIOV EMTP, with and without considering the LEMP contribution. The results are reported for both the cases of a first and a subsequent stroke channel base current waveform. Further results will be presented in the contribution that show how important can be for some cases the effect of the LEMP coupling on the amplitude of induced voltages even for the cases of direct strikes.

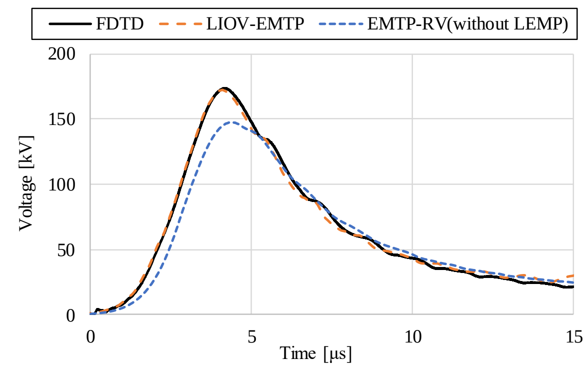

(a) First stroke

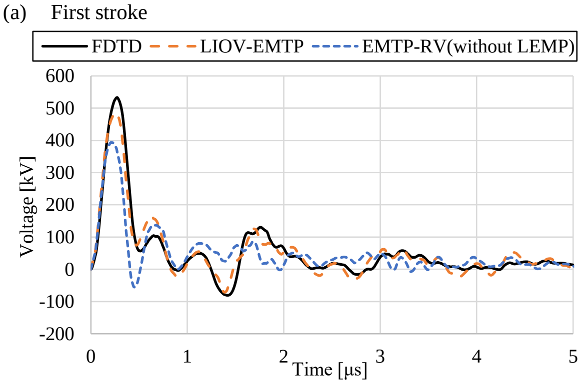

(b) Subsequent stroke

Figure 1. Voltages across insulators at lightning struck pole.

References

[1] K. Ishimoto, F. Tossani, F. Napolitano, A. Borghetti, and C. A. Nucci, "Direct Lightning Performance of Distribution Lines with Shield Wire Considering LEMP Effect," *IEEE Trans. Power Deliv.*, vol. 37, no. 1, pp. 76–84, 2022.

[2] A. Tatematsu and T. Ueda, "FDTD-based lightning surge simulation of an HV air-insulated substation with back-flashover phenomena," *IEEE Trans. Electromagn. Compat.*, vol. 58, no. 5, pp. 1549–1560, 2016.

[3] F. Napolitano, A. Borghetti, C. A. Nucci, M. Paolone, F. Rachidi, and J. Mahseredjian, "An advanced interface between the LIOV code and the EMTP-RV," in *29th International Conference on Lightning Protection*, Uppsala, Sweden, 2008, pp. 1–12.

Materials For Protection Against High Power Electromagnetic Impact

Natallia Nasonova
Proton R&D Innovations
UAE, Abu Dhabi
info@proton-innovations.com

Abstract – A problem of development of shielding materials capable of protection of electronic equipment and systems against HPEM impact includes the tasks of effective HPEM shielding and the produced heat release. Composite and hybrid materials containing fillers of various types are investigated against the HPEM shielding efficiency and thermal behavior.

Key words: HPEM pulsed impact, composite materials, microwave absorption, heat distribution

I. INTRODUCTION

The impact of high power electromagnetic (HPEM) pulses (>100 V/m, duration upto 1.0 ns) on radio-electronic systems and equipment results in losses (distortion) of information, false alarms of security, fire and other alarm systems, equipment malfunctions, blocking of data transmission channels (both wired and wireless), faults and failures of electronic devices, etc. Shielding is an important element of an integrated approach to protect electronic equipment, systems and networks against the HPEM impact.

II. SHIELDING AND ABSORBING MATERIALS

A. *Components justification*

The present investigations cover a wide range of composite materials, containing conductive materials, including those with magnetic properties, such as carbon or metal particles, nickel and iron powders, ferrites, conducting polymers, liquid solutions, and their combinations and other fillers, dispersed in specific structural materials, such as elastic polymers, synthetic resins, concrete, mortars, etc (Figure). Particle size, concentration, distribution in the matrix, and shape (grains, fibers, flakes, etc.) play a significant role. Synthesis of composite, multilayered filler materials and hybrid structure designing increase the shielding efficiency of the shields and absorbers.

B. *EM power absorption requirements*

In general, the EM power absorbed per volume unit P_{loss} is determined by the frequency of the incident radiation f and the dielectric losses ε'' of the composite material:

$$P_{loss} = \omega\varepsilon_0\varepsilon''_r|E|^2 \approx 0{,}556\cdot 10^{-12}\varepsilon''_r E^2 f, W/cm^2$$

An important problem for shields and microwave absorbers development is to develop a material, which is thermally stable for a long period of radiation exposure or quickly restore its properties after short-term heating without reducing the efficiency characteristics.

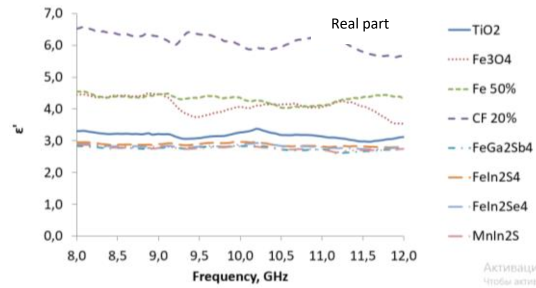

a

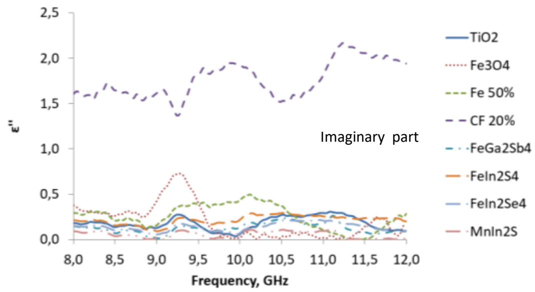

b

Figure. Complex permittivity for some of the developed polymer-based composites with various powder fillers in the frequency band of 8–12 GHz

The problem of HPEM shielding materials development includes the following aspects: 1. Analyze the application conditions; 2. Select the types of fillers and binders to achieve high shielding efficiency, as well as the workability of the resulting material; 3. Analyze the heat release processes in a composite material upon absorption of HPEM energy.

C. *Heat release analysis*

The impact of microwave electromagnetic radiation produces a temperature increase per dielectric volume unit:

$$\frac{dQ}{dt} = 8\cdot 10^{-12}E^2 f\frac{\varepsilon''_r}{\gamma c}, deg/min$$

γ – is bulk density, g/cm^3; c – is a specific heat capacity, cal/g·deg. Since composite materials have a heterogeneous structure, there are losses due to thermal conductivity and radiation and the heat distribution process depends on multiple factors. The power P_h, which is required to heat a dielectric of weight G by ΔQ deg, can be approximately determined as follows:

$$P_h = 4{,}186\cdot G\cdot c\cdot\Delta Q, \mathrm{kW}$$

The measuring installation includes a pulse voltage generator PVG 50-1000 and an electric field digital indicator. The shielding efficiency regarding UWB electromagnetic pulses, averaged over the frequency range for their spectrum, is defined as the ratio of the electric field amplitudes measured before the shield was installed (E_1) and after it was installed (E_2):

$$\mathrm{SE} = 20\cdot\log\left(\frac{E_1}{E_2}\right), dB$$

A thermal portrait of a material while HPEM absorption in practice is obtained using a thermal imager.

3D Printed Absorbing Frequency Selective Surface in the S-Band

Fernando Albarracin, Mae AlMansoori, Felix Vega, Chaouki Kasmi, Nicolas Mora
Directed Energy Research Center, Technology Innovation Institute, Abu Dhabi, UAE
fernando.albarracin@tii.ae

Abstract—This work presents the design and experimental characterization of a 3D printed absorbing frequency selective surface (FSS) working in the S-band. Conductive polylactic acid (PLA) is used to manufacture the unit cells composing the high impedance surface.

Keywords- additive manufacturing, absorbing FSS, resistive surface

I. INTRODUCTION

The study and development of frequency selective surfaces (FSS) to implement high impedance surfaces (HIS) have been a well-reported topic in the past years [1]. A HIS is implemented by placing an FSS on top of a grounded dielectric slab. These structures are designed to exhibit a perfect magnetic conductor (PMC) behavior over a certain frequency range. Applications include surface current suppression, radar cross section reduction, and microwave thin absorbers. Numerous techniques can be used to implement a microwave thin FSS-absorber, such as photo etching from conductive layers and printing of conductive inks [2]. Additive manufacturing using conductive material is an alternative for quick prototyping of FSSs. In this work, a 3D-printed wideband absorbent FSS in the S-band is designed and implemented. Experimental results of the absorption level and the characterization of the PLA material are presented.

II. ABSORBING FSS DESIGN

The surface impedance of the absorbing-FSS can be computed as the parallel connection of the FSS impedance and the grounded substrate impedance:

$$Z_{abs} = \frac{Z_{FSS} Z_d}{Z_{FSS} + Z_d}. \qquad (1)$$

When the reactance of Z_{FSS} cancels the inductance of Z_d, the parallel circuit resonates, and Z_{abs} becomes real-valued [1]. The real part of Z_{abs} must match the free-space impedance to effectively absorb the incoming wave. Under this condition, an optimum value R_{FSS} = Re{Z_{FSS}} can be extracted [1].

$$R_{FSS} = \left(\frac{\beta}{\omega \varepsilon_r \varepsilon_0 \eta_0} \right) \tan^2(\beta d) \approx R_s \left(\frac{P^2}{A} \right) \qquad (2)$$

where d is the dielectric thickness, η_0 and ε_0 are the free-space impedance and permittivity, respectively, P is the FSS periodicity, and A is the area covered with PLA per unit cell. β is the propagation constant and ω is the angular frequency. The FSS sheet resistance, R_s (Ω/sq), is related to the PLA conductivity σ, and thickness h_t, as [1]

$$R_s = \frac{1}{\omega h_t j \cdot (\varepsilon_0 \varepsilon_r - j\sigma / \omega)} \approx \frac{1}{h_t \sigma} \qquad (3)$$

The dielectric parameters of the conductive PLA material were characterized using an open-ended coaxial probe, and the results are plotted in Fig. 1.

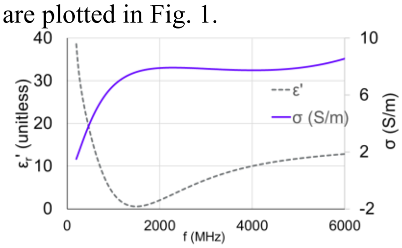

Figure 1. Conductive PLA measured characteristics.

A crisscross geometry is selected as the FSS unit cell due to its simplicity and wideband response [2]. The thickness of the unit cell is optimized via full-wave simulation, using the PLA material characteristics. An array of 6 x 7 squared unit cells with a 6.25 cm side was 3D-printed with a 100% density. Fig. 2a shows the prototyped unit cell. The FSS is glued on one side of a 12 mm thick Styrofoam layer (ε_r=1.1), 38x44 cm^2. A layer of aluminum foil acts as the ground plane.

III. RADIATION TEST RESULTS

A two antenna, quasi-monostatic setup was used to characterize the FSS in an anechoic environment. The transmission parameter (S_{21}) from an aluminum plate of the same dimensions as the FSS is used as the reference. A comparison of the measurement and simulation results is presented in Fig. 2b. Discrepancies are observed at low frequency. However, almost the complete S-band is covered with the presented design for absorbance levels better than -10 dB.

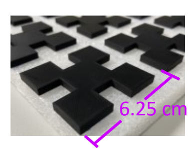

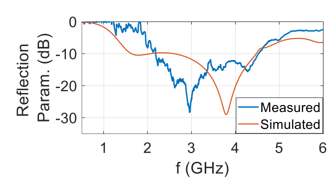

(a) (b)

Figure 2. 3D-printed absorbing FSS prototype. (b) Measured reflection coefficient on boresight.

REFERENCES

[1] F. Costa, A. Monorchio, and G. Manara, “Analysis and Design of Ultra-Thin Electromagnetic Absorbers Comprising Resistively Loaded High Impedance Surfaces,” *IEEE Trans. Antennas Propag.*, vol. 58, no. 5, pp. 1551–1558, May 2010.
[2] L. Sun, *et al.*, “Broadband metamaterial absorber based on coupling resistive frequency selective surface,” *Opt. Express*, vol. 20, no. 4, pp. 4675–4680, Feb. 2012.

An Efficient Computer Code for the Analysis of Grounding Systems Using the Method of Moments

Hamidreza Karami[1], Carlos Romero[2], André Koch[2], Marcos Rubinstein[3], Farhad Rachidi[1]
[1] EPFL, Lausanne, Switzerland, hamidreza.karami@epfl.ch and farhad.rachidi@epfl.ch
[2] armasuisse Science and Technology, Thun, Switzerland, andre.koch@DynamicPhenomena.ch and carlos.romero@ar.admin.ch
[3] University of Applied Science of Western Switzerland, Yverdon-les-Bains, Switzerland, marcos.rubinstein@heig-vd.ch

***Abstract*—We present an efficient computer code based on the method of moments (MoM) for the analysis of arbitrary grounding systems embedded in a lossy soil.**

Keywords- Grounding system; numerical method; method of moments (MoM); input impedance.

I. Introduction

Accurate analysis of grounding systems is an important topic in electromagnetic compatibility (EMC) studies. The importance mainly lies in the fact that grounding systems play a crucial role in protecting people and facilities from disturbances generated by faults, lightning strikes and other transients. The aim of this paper is to present an efficient computer code based in the Method of Moments for the analysis of grounding systems.

II. Code Structure

The proposed code is based on the mixed potential integral equation method presented in [1]. The tangential component of the total electric field over the grounding object is forced to zero in this method. By substituting the scattered field with the vector of magnetic potential and electric potential scalar and performing the expansion and testing procedure in the Method of Moments (MoM), linear algebraic equations can be obtained. Solving these equations yields the current distribution along the grounding system.

The structure of the code can be divided into three parts: 1) Input, 2) Kernel, and 3) Output as illustrated in Figure 1 (a). In the input part, one should define the geometry of the grounding system, the electrical parameters of the soil, and the frequency range of the simulation. In the Kernel part, all the numerical steps needed for the simulation of the grounding system response and the calculation of the input impedance are embedded, for example, finding the junctions, meshing the structure, and creating all the sub-matrices to calculate the input or mutual impedance, Z_{in} or Z_{12}. Finally, the user can plot the required part of the input impedance in the Output part. The code has been validated using as reference numerical results in [2].

III. Numerical Example

We consider a 60×60 m^2 grounding grid with 6×6 meshes buried at a depth of 0.5 m [2] as shown in Figure 1 (b). In this figure, the solid-black lines, blue circles and red crosses show the ground electrodes, the nodes, and the excitation port (the lightning attachment point), respectively.

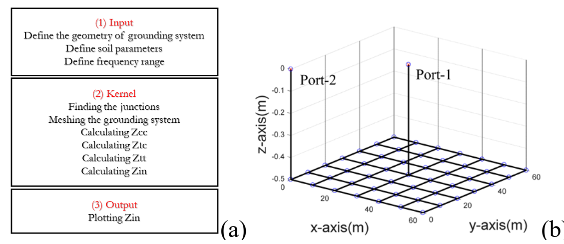

Figure 1. (a)The structure of the code for the analysis of grounding systems. (b) A 60×60 m^2 grounding grid with 6×6 meshes buried at a depth of 0.5 m.

The grid is composed of 7-mm radius rods. In Figure 1 (b), Port-1 and Port-2 are considered to be located at the center and at one corner of the grid, respectively. The soil is characterized by a permittivity of $\varepsilon = 9$.

The magnitude of the input impedance of the considered grounding grid is shown in Figure 2 for different soil conductivities. The obtained results are consistent with the results presented in [2].

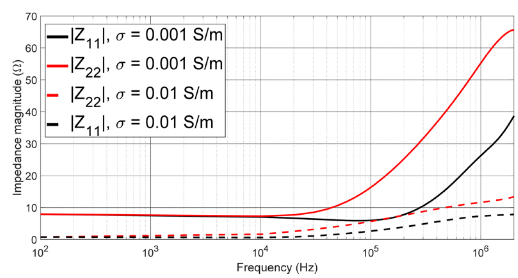

Figure 2. Magnitude of the input impedance of the 60×60 m^2 grid buried at 0.5 m depth in a homogenous soil excited from the center and corner ports as shown in Figure 1.

The main advantage of the MoM is that the mesh cells needed to solve the problem is limited to the grounding structure only, unlike other numerical methods such as finite-difference time-domain or finite-element methods. Future work includes the extension of the code to take into account stratified soils.

References

[1] H. Karami, K. Sheshyekani, and F. Rachidi, “Mixed-potential integral equation for full-wave modeling of grounding systems buried in a lossy multilayer stratified ground,” *IEEE Trans. Electromagn. Compat.*, vol. 59, no. 5, 2017.
[2] M. Heimbach and L. D. Grcev, “Grounding system analysis in transients programs applying electromagnetic field approach,” *IEEE Trans. Power Deliv.*, vol. 12, no. 1, pp. 186–193, 1997.

Landmine Detection Using Electromagnetic Time Reversal Based Methods

Hamidreza Karami[1], André Koch[2], Carlos Romero[2], Marcos Rubinstein[3], Farhad Rachidi[1]
[1] EPFL, Lausanne, Switzerland, hamidreza.karami@epfl.ch and farhad.rachidi@epfl.ch
[2] armasuisse Science and Technology, Thun, Switzerland, andre.koch@DynamicPhenomena.ch and carlos.romero@ar.admin.ch
[3] University of Applied Science of Western Switzerland, Yverdon-les-Bains, Switzerland, marcos.rubinstein@heig-vd.ch

Abstract—In this paper, the interaction between a measurement system, the landmine, and the soil is investigated to detect an unknown buried object. In particular, the performance of different approaches for landmine localization using electromagnetic time reversal (EMTR) methods is investigated in terms of their detection efficiency and computational efficiency. The considered methods include the classical time-domain EMTR, iterative EMTR, EMTR-DORT (decomposition of the time reversal operator), and EMTR-MUSIC (Multiple signal classification). The obtained simulation results show that EMTR is a promising technique for landmine detection and localization.

Keywords- Landmines; time reversal base methods;

I. Introduction

Although a large spectrum of methods has been investigated to detect landmines, only enhanced metal detectors and ground penetrating radars have been used in the field [1]. The performance of these methods is still far from the desired levels due to the complexity of the environmental and field conditions. In this paper, time reversal methods in both the acoustic and the electromagnetic regime [2] have been applied to localize landmine(s). We present the results of an investigation in which different types of EMTR based methods (classical EMTR, iterative EMTR, DORT, and TR-MUSIC) are applied to the problem of landmine localization. These methods have shown to be promising in terms of accuracy and efficiency in localizing landmines, and could potentially replace or complement existing methods in the future.

II. Comparison between EMTR-Based Methods

The simulation results showed that both the TR-MUSIC and DORT methods, implemented in a single frequency, were able to accurately locate the targets. The resolution of the DORT method can be increased by increasing the number of antennas. However, even with a higher number of antennas, DORT does not allow to achieve super-resolution. With a similar computational cost to that of the DORT method, EMTR-MUSIC is able to achieve super-resolution to distinguish targets located within distances as low as $\lambda/20$. The classical EMTR method implemented in the time-domain requires higher computational resources compared to DORT and TR-MUSIC. In summary, TR-MUSIC appears to outperform other EMTR-based methods, allowing to detect multiple closely spaced targets using a reasonable number of sensors.

III. Numerical Results

As seen in Figure 1 (a), A 5-mm radius spherical metallic target is buried in a homogeneous soil at a depth $d = 0.4$ m. Three identical dipole antennas are used as transmitters with length and radius 135.5 mm and 2.5 mm, respectively. At 1 GHz, the antenna return loss is about 20 dB, which is appropriate to detect landmines at this frequency. All dipole antennas are at a height $h = 0.5$ m above the ground. The horizontal distance between adjacent antennas is $s = 0.5$ m. The frequency range of the excitation Gaussian pulse is from 0 to 2.0 GHz.

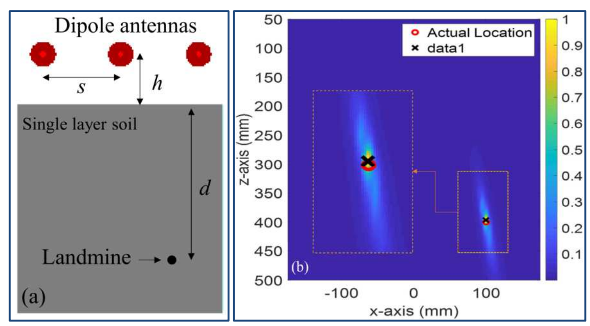

Figure 1. (a) A view of the geometry of the homogenous soil half-space problem. (b) 2D view of the TR-MUSIC pseudospectrum. The red circle and the black cross show the actual and estimated landmine locations. The soil permittivity and conductivity are 4.0 and 0.01 S/m, respectively.

Figure 1(b) shows the TR-MUSIC pseudospectrum obtained using the CST-MWS time-domain solver. The red circle and black cross show respectively the actual and estimated target locations. In this case, TR-MUSIC could localize the landmine with a localization error of 3.58 mm.

References

[1] "Guidebook on Detection Technologies and Systems for Humanitarian Demining | Geneva International Centre for Humanitarian Demining." [Online]. Available: https://www.gichd.org/en/resources/publications/detail/publication/guidebook-on-detection-technologies-and-systems-for-humanitarian-demining/. [Accessed: 21-Jan-2021].
[2] V. R. N. Santos and F. L. Teixeira, "Application of time-reversal-based processing techniques to enhance detection of GPR targets," J. Appl. Geophys., vol. 146, pp. 80–94, Nov. 2017.

Electric Field Radiation from the Tapered-Impedance Half Impulse Radiating Antenna

Felix Vega, Fernando Albarracin, Abdul R. Baba, Adamo Banelli, Chaouki Kasmi
Directed Energy Research Center, Technology Innovation Institute, Abu Dhabi, United Arab Emirates
fernando.albarracin@tii.ae

Abstract**—**This work presents experimental results from a radiation test of the tapered impedance half impulse radiating antenna (TI-HIRA) when fed by a commercial 50-Ω pulsed generator. The design of a prototype and the measured electric field waveform are presented.

Keywords- electric field measurement, impulse radiating antenna, tapered impedance converters.

I. INTRODUCTION

During the last decades, the impulse radiating antenna IRA, has been widely used for radiating high-amplitude electromagnetic pulses for EMC and IEMI studies. The half-IRA (HIRA), is the monopolar version of the IRA and is implemented by introducing a ground plane in the horizontal symmetry plane [1]. In the conventional operation of a HIRA, a constant-impedance TEM transmission line composed with coplanar-plate feeders illuminates a parabolic metal dish with a spherical wave, to finally generate the main radiated pulse. A correlation between optimal illumination of the dish and feeder size constrains the HIRA input impedance to values close to 100 Ohm [2]. Therefore, a commercial unbalanced 50-Ω generator would need an external wideband impedance transformer to feed the HIRA. As an alternative, the authors introduced the tapered impedance HIRA (TI-HIRA) [1] by integrating a TEM feeder whose characteristic impedance changes as a function of the radial distance from the focal point to the dish aperture. The TI-HIRA is sketched in Fig. 1a.

II. TI-HIRA DESIGN

The impedance of a TEM feeder arm, when the exponential progression is selected, can be computed as

$$Z(r) = Z_1 e^{\alpha r} = 60\pi \frac{K(m(r))}{K(1-m(r))}, \tag{1}$$

where r is the radial distance measured from the focal point, the exponential coefficient is $\alpha = (1/F)\ln(Z_2/Z_1)$. Z_1 is the arm impedance at, Z_2 is the terminating impedance at the reflector side, F is the focal length. $K(m(r))$ is the complete elliptic integral of the first kind, and $m(r)$ is a parameter defining the impedance of the TEM feeder [1]. Once F, Z_1, and Z_2 are defined, $m(r)$ is numerically solved for each value of r in (1). The feeder geometry is sketched in Fig. 1b. The aperture angles of the feeder arm, β_1, and β_2, become a function of r, computed as

$$\beta_1(r) = 2\tan^{-1}\left(m(r)^{0.25}\tan\left(\frac{\beta_0}{2}\right)\right), \quad \beta_2 = 2\tan^{-1}\left(m(r)^{-0.5}\tan\left(\frac{\beta_1(r)}{2}\right)\right) \tag{2}$$

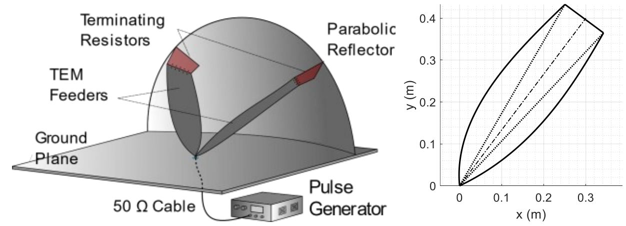

Figure 1. (a) TI-HIRA. (b) Feeder geometry: Exponential impedance arms (continuous line) and constant impedance arms (dashed line).

A dish with a diameter of 1.2 m and F = 0.46 m is used. Z_1 and Z_2 are 100 Ω and 200 Ω, respectively. Note that the TI-HIRA input impedance is expected to be the parallel connection of two feeding arms i.e., 50 Ω.

III. RADIATION TEST RESULTS

A 50 Ω solid-state pulsed generator, with a peak voltage of 14 kV, a risetime of 100 ps, and a pulse width of 3 ns is used to drive the TI-HIRA prototype in a semianechoic environment. On the receiving side, a B-dot free-field magnetic field sensor, with an equivalent area of $9\cdot10^{-6}$ m^2 was used. The B-dot is connected to a 6 GHz oscilloscope through an ultra-wideband balun. The receiving chain was placed inside a shielded box and powered via UPS. A comparison of the measured and the simulated electric field waveform on boresight, reduced to 1 m, is presented in Fig. 2. Small discrepancies can be observed in the prepulse area. As it can be seen there is excellent agreement between the experimental and simulated results.

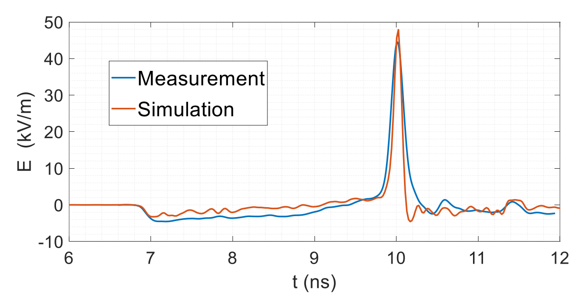

Figure 2. TI-HIRA Electric field waveform, reduced to 1 m.

REFERENCES

[1] F. Vega, F. Albarracin-Vargas, C. Kasmi, and F. Alyafei, "The Tapered Impedance Half-Impulse Radiating Antenna," *IEEE Trans. Antennas Propag.*, vol. 69, no. 2, pp. 715–722, Feb. 2021, doi: 10.1109/TAP.2020.3016496.

[2] E. G. Farr and C. E. Baum, "Prepulse Associated with the TEM Feed of an Impulse Radiating Antenna," *Sens. Simul. Notes 337*, Mar. 1992.

Investigation of Electrode Erosion in Gas-Filled Spark Gap Switch

A. R. Baba, A. Mohanta, J. J. Pantoja, M. Alkaabi, A. Alebri, F. Vega, G. Matras, S. Al Marzooqi, A. Dubey, A. Alteneiji, R. Al Ameri, and C. Kasmi
Directed Energy Research Center,
Technology Innovation Institute,
Abu Dhabi, United Arab Emirates
abdul.baba@tii.ae

Abstract—In this work, erosion on electrodes used in gas-filled spark gap switches is experimentally investigated. Two different electrode profiles, including a new profile with axial holes proposed here for laser-triggered gas-filled spark gap switch, are considered. Based on experimental results, the life span of the electrodes and the degradation of main parameters, including rise time, and hold-off voltage, are estimated.
Keywords: Spark gap, Electrode profile, Streamer, Gas-filled spark gap switch, Electrode erosion

I. INTRODUCTION

Gas-filled spark gap switches have widely been used in pulsed power technology due to their simple construction, low cost, and ease of operation [1]. The reliability of gas-filled spark gap switches is based on the surface quality of the electrodes, gas decomposition and dissociation, and the insulator damage that occur as the energy is dissipated in the switch [2]. Different studies have been conducted to investigate the chemical and physical processes responsible for the erosion of the spark gap electrodes [2]. In this study, different electrode materials and profiles are considered. One of the profiles includes axial hole through which a femtosecond laser can be coupled axially between the two electrodes to trigger and achieve a lower jitter compared to the self-breaking spark gap switches.

II. ELECTRODE PROFILE

Erosion rates are determined by material, electrode profile, dimensions, gap length, polarity, voltage, and current. The profile with axial hole is shown in Fig.1. Due to the geometry and the field enhancement between the electrodes, it is important to investigate the erosion on the surface. The erosion rate of the electrodes is substantial around the tip of the electrodes in accordance with the electric field distribution shown in Fig. 2. Similar behavior has been reported for hemispherical and Rogowski electrodes [1] since discharges are confined around the center of the electrodes.

III. EXPERIMENTAL SETUP

Different electrode profiles and materials have been considered. The gap between the electrodes can be varied from 0.5 to 2 mm and nitrogen gas is used as a spark gap medium. The spark gap is connected to a charging capacitor through a resistor. The capacitor is charged by a DC voltage source capable of delivering up to 60 kV. The accurate distance between the two electrodes is measured with a feeler gauge. Erosion surface area is estimated by microscopic measurements of pits on the tips of the electrodes.

Fig.1 Laser-triggered gas-filled spark gap prototype design.

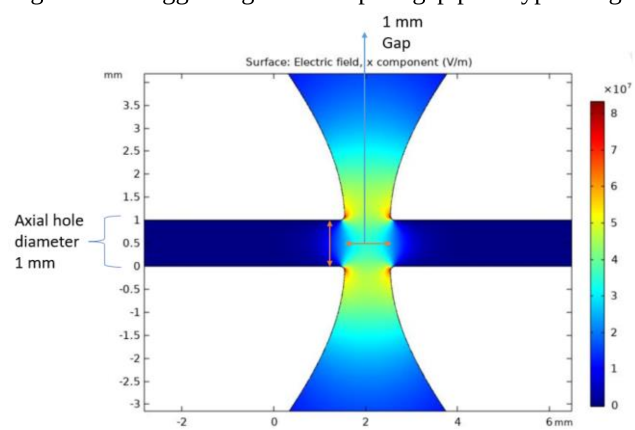

Fig. 2 Electric field simulation of electrodes with 1 mm gap distance for 50 kV.

IV. DISCUSSION

Electrode erosion after a certain number of pulses results in field distortion that degrades and deteriorates the hold-off voltage and rise time for high voltage applications. Electrodes have been subjected to high local pressure from the arc area due to the expansion of plasma which could lead to the pit formation on the tips of the electrodes. Appropriate selection of electrode profile along with material can reduce the electrode erosion rate, which can lead to higher reliability of the switch.

REFERENCES

[1] V. Gandi, R. Verma, M. Warrier, and A. Sharma, “Effect of Electrode Profile and Polarity on Performance of Pressurized Spark gap Switch,” Plasma, vol. 5, pp. 130–145, 2022.

[2] L. B. Gordon, M. Kristiansen, M. O. Hagler, H. C. Kirbie, R. M. Ness, L. L. Hatfield, and J. N. Marx, "Material Studies in a High Energy Spark Gap," IEEE Trans. Plasma Sci., vol. PS-10, pp. 286–293 (1982).

Two Different Types of 3D Lightning Mapping Systems Developed for Observing Winter Lightning in Japan

Daohong Wang
Department of Electrical, Electronic and Computer Engineering
Gifu University, Gifu, Japan
wang@gifu-u.ac.jp

Haitao Huang
Department of Electrical, Electronic and Computer Engineering
Gifu University, Gifu, Japan
hitao_huang@yahoo.co.jp

Nobuyuki Takagi
Department of Electrical, Electronic and Computer Engineering
Gifu University, Gifu, Japan
takagi-n@gifu-u.ac.jp

Junchen Yang
Department of Electrical, Electronic and Computer Engineering
Gifu University, Gifu, Japan
yangjc227@gmail.com

Ting Wu
Department of Electrical, Electronic and Computer Engineering
Gifu University, Gifu, Japan
tingwu@gifu-u.ac.jp

Kazuo Yamatomo
Department of Electrical Engineering
Chubu University, Kasugai, Japan
kyamamoto@isc.chubu.ac.jp

Abstract—We have developed two different types of 3D lightning mapping systems for observing winter lightning in Japan. One of the systems consists of 12 stations. At each of the station, a discone antenna is used for the sensor and its output is sampled at 25 MS/s with 16 bits. This system uses time-of-arrival technique and is called DALMA (Discone Antenna Lightning Mapping Array). Another system consists of 3 stations. At each of the stations, a broadband interferometer with 3 discone antennas as sensors was deployed. In this system, the outputs from all antenna are sampled at 1GS/s with 16 bits. The latter system primarily uses interferometry technique and is called InLMA (Interferometer-type of Lightning Mapping Array). Both systems are GPS-synchronized. Using these two systems, we have recorded many winter lightning discharges. This paper is to report the two systems and one example result obtained.

Keywords- Lightning, Lightning mapping, Winter lightning, Upward lightning

I. INTRODUCTION

As it is well known, winter thunderstorms in Japan are usually much lower than summer thunderstorms. In addition, many upward lightning and positive lightning occurred during winter thunderstorms in Japan. These factors make 3D mapping of winter lightning in Japan a very challenging issue since all lightning mapping systems suffer an intrinsic deterioration in the uncertainty for locating low altitude sources, particularly sources of positive leaders. As a matter of fact, we have tried to use the FALMA (Fast Antenna Lightning Mapping Array) for 3D mappings of winter lightning but failed [1]. In this study, we have developed and deployed two systems which are capable of doing 3D mapping of winter lightning within the area covered by the FALMA. This paper is to report the two systems and one interesting flash observed by the two systems.

II. RESULT

As an example, a lightning flash mapped by DALMA [2] is shown in Fig.1. Unlike summer lightning, this winter lightning exhibited very complicated progression features. During the conference, we will report the detail of the complicated features with the result by InLMA included.

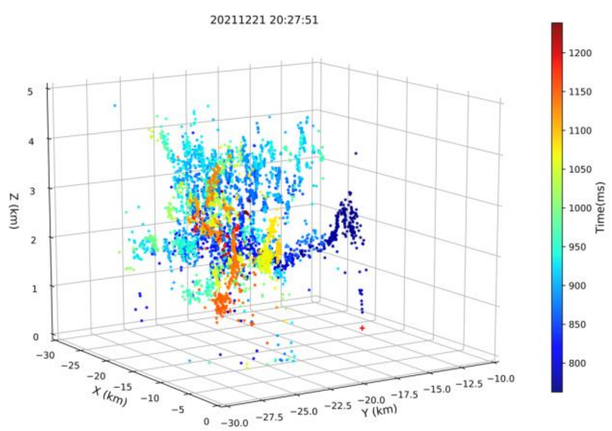

Figure 1. 3D mapping of an interesting lightning flash

REFERENCES

[1] Wu, T., Wang, D., & Takagi, N. (2020). Multiple‐stroke positive cloud‐to‐ground lightning observed by the FALMA in winter thunderstorms in Japan. Journal of Geophysical Research: Atmospheres, 125, e2020JD033039.

[2] Wang, D., Wu, T.,Huang, H.,Yang, J., & Yamamoto, K. (2022). 3D Mapping of Winter Lightning in Japan with an Array of Discone Antennas. IEEJ. https://onlinelibrary.wiley.com/doi/full/10.1002/tee.23667

ACKNOWLEDGEMENT

This research is mainly supported by the project JPNP07015 commissioned by the New Energy and Industrial Technology Development Organization (NEDO) of Japan.

The Concept of a Switched Oscillator Box Array: 4x3 Matrix Resonant Source for HPEM Applications

Mae AlMansoori, Ernesto Niera, Luciano Prado de Oliveira, Abdul Rouf Baba,
John J. Pantoja, Fernando Albarracín-Vargas, Felix Vega, Chaouki Kasmi
Directed Energy Research Center, Technology Innovation Institute, Abu Dhabi, UAE
Mae.almansoori@tii.ae

Abstract—This paper presents the concept of a resonant source for High Power Electromagnetic applications based on a Switched Oscillator (SWO) box. The single unit design will be discussed and validated. The final prototype of array was manufactured and presented in the paper.

Keywords-switched oscillator, TEM-horn antenna,

I. INTRODUCTION

In this paper, we present a 4x3 transmitter array system for high-power electromagnetic applications. This system consists of multiple resonating transmitters, tuned at different frequencies, and integrated into a single radiating rack. Each transmitter is comprised of an antenna, switched oscillator, HV-source, and pneumatic system. The system can be used to test the susceptibility and vulnerability of devices in a frequency range of 100 to 900 MHz following IEC 61000-4-36 standards.

II. SINGLE UNIT DESIGN AND VALIDATION

A single transmitter box, shown in Fig. 1, has been designed and integrated to be portable, compact, and independent of any external power source. The TEM horn "box-like" antenna has been designed [1] in which the cavity formed between the arms of the TEM horn and the ground plane has been used as housing for the SWO, the SF6 pneumatic system and the connecting elements. The HV pulsed source and the electronic control system have been installed in a small box attached to the back of the antenna. The whole system has a box-like form factor, with side dimensions of 0.44 λ. The single box is expected to produce an electric field around 10 kV/m at 1 m.

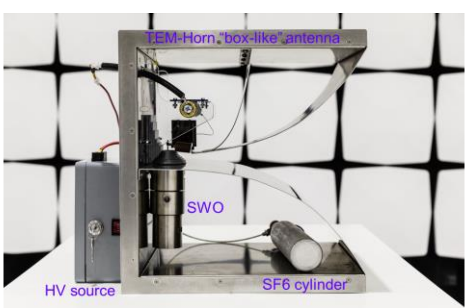

Figure 1. Single SWO box

The designed unit was tested and the electric field was measured in time domain. The reported peak amplitude was 9.51 kV/m at a charging voltage of 29kV with a central frequency of 330 MHz.

III. THE CONCEPT OF AN ARRAY

Based on the reported results of the single box, a concept of the array system has been developed combining 12 of the designed SWO boxes. The concept, shown in Fig. 2, presents the integrated system where each unit has its independent single-ended HV source, antenna, and radiating source. However, the 12 units has a single pneumatics circuit where each box is connected in series. The system is designed to have a peak electric field of 90 kV/m at 1 m. Moreover, this system has advantages over other systems with similar E-field ranges due to its low cost and easy maintenance. The manufactured final prototype is shown in Fig. 2.

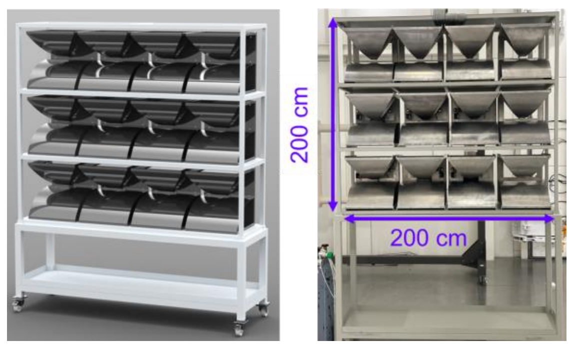

Figure 2. From left to right: 3D model, final manufactured prototype.

IIII. CONCLUSIONS

A design of a SWO Box array was presented based on a validated single SWO Box unit. The design is independent of any external power sources, low-cost, and easily maintained. The expected electric field is above 20 kV/m.

REFERENCES

[1] S. Wang and Y. Xie, "Design and Optimization of High-Power UWB Combined Antenna Based on Klopfenstein Impedance Taper," IEEE Transactions on Antennas and Propagation, vol. 65, no. 12, pp. 6960–6967, Dec. 2017.
[2] F. Vega and F. Rachidi, "A Switched Oscillator Geometry Inspired by a Curvilinear Space—Part I: DC Considerations," IEEE Trans. on Plasma Science, Vol. 44, No. 10, October, 2016.

Direction Finding System Based on an Additively Manufactured Stackable Luneburg Lens

Mae AlMansoori*(1)(2), A. Rangel(3), J. Pantoja(1), F. Vega(1)(4), A. Banelli(1), C. Kasmi(1)(2), L.O. Fichte(2), and M. Stiemer(2)

(1)Directed Energy Research Centre, Technology Innovation Institute, Abu Dhabi, United Arab Emirates

(2)Faculty of Electrical Engineering, Helmut Schmidt University, 22043 Hamburg, Germany

(3)Quanta Electromagnetic Science S.A.S, Bogota, Colombia

(4)Universidad Nacional de Colombia-Sede Bogotá, Bogotá 111321, Colombia

Mae.almansoori@tii.ae

Abstract— In this study, a 3D printed Luneburg lens-based direction finder was designed, manufactured, and tested. The paper discusses the material characterization process, followed by the design, construction, and finally the test of the prototype.

Keywords-Direction-of-arrival; Stereolithography.

I. INTRODUCTION

Direction of Arrival (DOA) estimation at microwave frequencies is important in many sensor applications such as wireless communications [1]. There are two known techniques used for DOA estimation [2]: the amplitude comparison which is wideband, low cost and portable but has low accuracy [2], and the phase interferometer system with high accuracy but is expensive and complex. Therefore, a DOA estimation system that is at relatively low cost, portable and possesses high accuracy is highly desirable in many applications. In this study, this will be achieved through a 3D printed stackable Luneburg lens.

II. LENS DESIGN AND MANUFACTURING

A Luneburg lens is a gradient index device in which the refractive index gradually changes inside the material [3]. The l variation in the permittivity profile of the lens is achieved by placing air inclusions in the base material, lowering the base permittivity to the required value [4]. The final design is shown in Fig. 1.

The lens was manufactured out of Acrylonitrile Butadiene Styrene (ABS) using Stereolithography (SLA) technology, which presented a dielectric constant of 3.07 at 1.5 GHz, and had finer details with an accuracy of ±0.01 mm. The manufactured lens is shown in Fig.1.

II. EXPERIMENTAL VALIDATION

A first test of the functionality of the lens was performed in an anechoic environment. A receiving antenna was placed at the Zeroth position of the lens. A transmitting antenna was placed at a constant radial distance and the relative angle between the transmitting antenna and the Zeroth position was varied between +- 45'. The received power per angle of arrival was measured. As comparison, the same test was performed removing the lens.

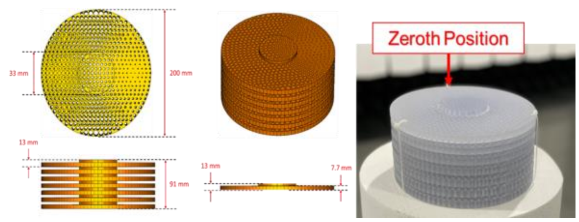

Figure 1. From the left to right: The constructed design of the Luneburg lens, manufactured and aligned final lens prototype. Notice the Zeroth position of the lens

The results presented in Fig. 2 shows that the power received maximizes when the relative angle coincides with the Zeroth angle of the lens, showing the capability of this device in identifying this angle of arrival.

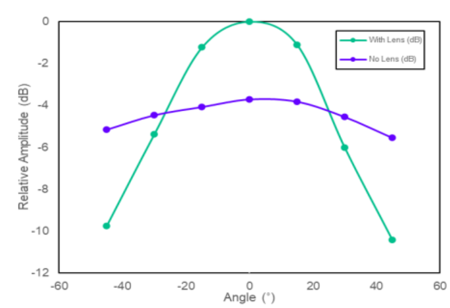

Figure 2. Relative amplitude measured at different angles of arrivals with and without lens. Notice how the lens maximizes the received power when the angle of arrival and the position of the lens coincide.

REFERENCES

[1] L.C. Godara, "Application of antenna arrays to mobile communications. II. Beam-forming and direction-of-arrival considerations," Proc. IEEE, Vol. 85, no. 8, pp. 1195-1245, 1997.

[2] J. Lee and J.Woo, "Interferometer direction-finding system with improved DF accuracy using two different array configurations," IEEE Antennas Wireless Propag. Lett., vol. 14, pp. 719–722, 2015.

[3] K. Sato and H. Ujiie, ''A plate Luneberg lens with the permittivity distribution controlled by hole density,'' Electron. Commun. Jpn. (Part I, Commun.), vol. 85, no. 9, pp. 1–12, Sep. 2002.

[4] M. Almansoori, A. Rangel, J. Pantoja, F. Vega, A. Banelli, C. Kasmi, L.O. Fichte, and M. Stiemer, "A study of materials and additive manufacturing techniques for a novel 2D Luneburg Lens", Proc. Int. Symp. Antennas Propag., Denver, Colorado, Jul. 2022 [submitted].

Protection of Control, Signal, and Data Points of Entry Against HEMP

Sergio N. Longoria
Technical Product Line Manager, Filters
ETS-Lindgren Inc., Cedar Park, Texas, USA
Sergio.longoria@ets-lindgren.com

Abstract— This paper discusses the special case of using passive filter devices on control, signal, and data Points of Entry (PoE) for the protection of electrical or electronic equipment against HEMP. Much of the discussion about protection of electrical PoE's is focused on facility power filters. However, it should be recognized that control, signal, and data cabling is also of concern and should be attended to properly. This paper will review the requirements for protection against HEMP and briefly touch on IEMI protection as described in various standards. The paper examines the electrical and mechanical characteristics needed in order to effectively accomplish the task of protecting and also providing operational reliability and safety for control, signal, and data points of entry

I. INTRODUCTION

We begin by noting the signal and control protection requirements of military standard MIL-STD-188-125 and commercial standard IEC 61000-4-24. It should be pointed out that these standards are only concerned with HEMP and not with IEMI. Other standards such as MIL-STD-461 deal with the issue of interference, but not as an act of deliberate and malicious intent. IEC 61000-4-36 is a commercial standard that effectively deals with the IEMI threat. A new standard, IEC 61000-5-10, is a guide for the application of protective measures for HEMP and IEMI.

Filters must handle conducted threats but must be constructed in a way that maintain the RF shielding effectiveness of the protected space to which they are attached. As such, the design of these filters should follow established standards and practices. These filters must be designed, validated, and tested not only for the required protection, but also as part of an RF shielded system that must remain operational, reliable, and safe during an attack as well as during normal operations.

The electrical and mechanical characteristics such as the type of materials used, the filter topology, construction practices, testing, and final installation are of critical importance for an effective mitigation and protection of defense and commercial structures. And while power filters should be built following the requirements of one or more safety standards such as UL 1283 and IEC 60939, signal and control filters have no such requirements and a more general standard such as MIL-PRF-15733 could be used.

II. THE PROTECTION STANDARDS

A PoE is any place within a shielded structure where there is an opening for passing cables, materials, or persons. In this paper, we are concerned only with PoEs that require metallic cables or wires to pass information from the unprotected area to the protected area or vice versa. MIL-STD-188-125 establishes that any cables passing through the shield must be treated for an HEMP threat such as E1 and E2. E1 is a fast pulse characteristic of the detonation of a nuclear warhead in space. E2 is a slower pulse similar to lightning. In addition, MIL-STD-188-125 establishes that the HEMP protection shield should be 80 dB from 10 MHz to 1 GHz. This does not consider IEMI which can fall on the frequency range above 1 GHz. Fortunately, filters can easily be made to work for IEMI once the filter has been designed to take care of the E1 and E2 pulses. But MIL-STD-188-125 is considered to be a severe protection standard and used mainly for critical defense structures. IEC 61000-4-24 considers different levels of protection depending on the structure to be protected and the level of protection desired. The intent is to show that extreme protection is costly whereas perhaps in some cases, a short disruption of operations may be acceptable in exchange for a more cost effective solution.

III. DESIGN OF CONTROL, SIGNAL, AND DATA PROTECTION FILTERS

A. Electrical Features

All control, signal, and data filters used for HEMP/IEMI protection must have a voltage rating and current rating consistent with the source and load impedances they will be protecting. In addition, typical designs for HEMP include an input inductor and a fast acting semiconductor arrestor device. But control, signal, and data filters pose a unique design challenge that is not present in power filters. That is, these filters typically have a broader passband than power filters. This passband may be upset by the addition of delay inductors, allowing distortion of the signal or passage of HEMP frequencies. An even more unique problem is found with high speed data signals as the passband of these must be quite large.

B. Mechanical Features

The filters' enclosure material should be plated steel or stainless steel. This is necessary so that conducted and radiated currents do not pass into the filter and thus into the protected area, but rather get diverted to earth ground or reflected. The proper filter design should have at least one completely sealed compartment on the load side for effective mitigation of HEMP/IEMI of the protected area.

C. Filter Testing

Filters should be tested for safety according to the manufacturer's procedures or MIL-PRF-15733. The filter expected attenuation (insertion loss) should be in compliance with the protection requirements and tested per MIL-STD-220 or CISPR 17. In addition, the filters should be tested for their residual current performance during a simulated HEMP PCI event. PCI testing is done as design verification by a 3rd party, and typically not during production.

Problems and Best Practices in Protecting Data Lines Against HEMP

Sergio N. Longoria
Technical Product Line Manager, RF Filters
ETS-Lindgren Inc., Cedar Park, Texas, USA
Sergio.longoria@ets-lindgren.com

Abstract**—**This paper discusses the unique design problems associated with protecting data lines with passive filters against a HEMP event. In today's intercommunicated world, much of the electronic communication takes place over data channels, more specifically data wires. These wires can carry data in a myriad of formats and speeds. Some of the data could be Ethernet, others could be control signals such as RS232 or RS485. Each of these could be passing data at different speeds. For example, we have RS485 protocols that can send data at 78 kbps or at 115 kbps. In addition, data signals can carry encoded voice messages, or can carry proprietary sensor information to a control center. A control center could be a HEMP hardened building where it would be necessary to have all these data transmission wires protected against an EM pulse. Many HEMP protection standards recommend that data signals should be converted to fiber in order to safely pass this data during a HEMP event. But the recommendation begs the question as to why that is. Thus, this paper will discuss the nature of the data that is to pass through, the pulse that data wires need to be protected against, and the filter characteristics that make protection with passive data filters problematic. Finally, some recommendations on protecting sites according to well-established commercial and military standards are provided.

I. THE HEMP FILTER AND ITS IMPLICATIONS

A. *The Data to Pass Through*

On the one hand, a data signal consists of a train of pulses or a square wave. Fourier Transformation of a complex wave tells us that a square wave is actually made up of multiple sinewaves as shown in Fig. 1. Any complex wave can be broken down into sine waves that when added together give the original complex wave.

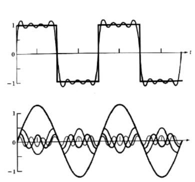

Fig. 1. Complex waves can be broken down into sine waves

Thus, a data filter must be able to pass all the composite sine waves in order to be able to reproduce at the other end the same square wave without loss of fidelity to the signal, without loss of the shape, and thus without loss of information as it passes through the filter. These multiple sine waves are actually at multiple frequencies. When a square wave is seen in the frequency domain, it looks as shown in Fig. 2. A filter is typically a passive device that would allow, up to a certain cut off, frequencies to pass. In filter terminology, we say that the passband of the filter must be wide enough to allow for all these composite sine waves to pass through.

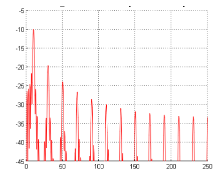

Fig. 2. Frequency domain view of a complex waveform

But this wide passband is also the Achilles' heel of all passive data filters used for HEMP protection.

B. *The HEMP Waveform*

The HEMP waveform or pulse shape is given in various well-known standards. This is essentially a double exponential pulse with an established rise time as shown in Fig. 3.

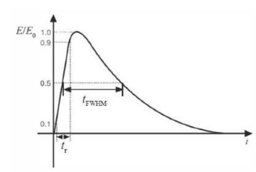

Fig. 3. Typical HEMP waveform

The composition of a signal like this shows that the pulse's rise time contributes to a multiple frequency component that can be shown by Fourier analysis. It is accepted that the typical HEMP waveform would generate frequency components from a few kHz to about 300 MHz.

C. *Data Filter Passband*

A typical data filter is a low pass filter that has a passband, or 3dB cut off point at several MHz in order to allow the data to pass without degradation. In addition, the stop band is further removed at several MHz because passive components do not have a sharp or instantaneous cut off at 3dB. Thus most of the energy of a HEMP event will be in-band or pass right through the filter, with only some lesser energy passing through the skirts of the filter's response. This would typically result in greater power residuals (or transients) appearing in the data line which could still damage the system that the filter was intended to protect.

D. *HEMP Protection of Data lines*

Because of the foregoing, data wires should be converted to fiber as recommended in commercial and military standards. Exceptions could be made if the data wires have a slow transmission rate, probably below 9.6kbps. But even in such cases, it would be prudent to inquire of the filter manufacturer if a given data filter meets a given protection standard.

Experimental Investigation of the Breakdown Voltage of Nitrogen (N_2) and Sulfur Hexafluoride (SF_6) Gaseous Mixture

Using Experimental and Numerical Methods

M. AlYousef(1), M. AlKaabi(1), Y. AlNuaimi(1), S. AlDahmani(1), H. AlKetbi(1), H.AlYahyaee(1), M. AlMenhali(1), A. AlEbri(1), H. AlHammadi(1), A. Al Ali(1) , F. Vega (1), C. Kasmi(1)

(1) Direct Energy Research Center, Technology Innovation Institute, Abu Dhabi, United Arab Emirates
mohamed.alyousef@tii.ae

Abstract—This paper studies the breakdown voltage of a gaseous mixture of Nitrogen (N_2) and Sulfur Hexafluoride (SF_6). The study consists of both experimental and numerical methods. The comparison was conducted under various pressures, separation distance, and gases compositions. The results were measured using a pressurized dipole spark gap for the breakdown at a corresponding distance and were processed using an octave code that records the observed trend of the findings.

Keywords: Insulation Gases, Spark Gap, Voltage Breakdown

I. INTRODUCTION

Dielectric, or insulating, gases prevent electric discharge up-to a certain electric field level. They are used in multiple applications such as: Transformers, circuit breakers, and generally in HV pulsed power applications. Two of the most commonly used gases are Nitrogen (N_2) and Sulfur Hexafluoride (SF_6), the later having a relatively higher dielectric strength than the former. Paschen's law provides one of the most fundamental equations that describes the relation of the voltage breakdown between two electrodes and the gas pressure times the distance between the electrodes.

$$V_B = \frac{Bpd}{\ln(Apd) - ln\left[\ln\left(1+\frac{1}{\gamma_{se}}\right)\right]} \qquad (1)$$

where, V_B: breakdown voltage in volts, p: pressure in Pascals, d: gap distance in meters, γ_{se}: secondary-electron-emission coefficient, A: saturation ionization in the gas at a particular E/p, B: is related to the excitation and ionization energies. Notice that Eq (1) applies in uniform electric field conditions.[3]

A mixture of gases is used to optimize the breakdown voltage and corresponding pressure for numerous spark gap applications. Using only SF6 is a costly alternative, therefore mixing it with N2 would reduce the overall operating cost. This study will illustrate the optimum mixture composition.

When it comes to mixtures of different gases Paschen's law does not provide an equation that predicts the voltage breakdown; this is the goal of this paper through experimental testing.

Other papers and articles [1], [2] are using mathematical methods and approximations to estimate the dielectric strength of gas mixtures. As a continuation of these efforts this paper will present a series of experiments specifically on the mixture discussed and compare the results with the theoretical estimations.

II. METHODOLOGY

The experimental setup is presented in Figure. 1. It consists of a power supply, DC-AC converter, HV transformer, 2-stage voltage multiplier, and a spark gap. A HV Probe across the spark gap measures the voltage breakdown. The results are plotted based on the experimental output data. In addition, the experiment was done by varying the pressure, gas mixture percentage, and the distance between the electrodes.

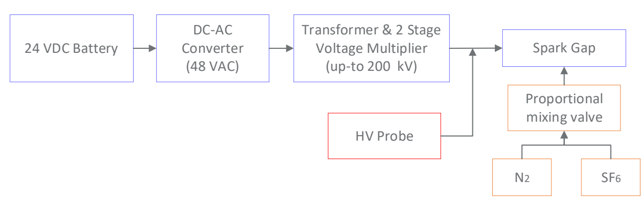

Figure 1. Experimental setup.

REFERENCES

[1] P. J. Chantry and R. E. Wootton, "A critique of methods for calculating the dielectric strength of gas mixtures", Journal of Applied Physics 52, 2731-2739 (1981)

[2] N. H. Malik and A. H. Qureshi, "A Review of Electrical Breakdown in Mixtures of SF6 and Other Gases," in *IEEE Transactions on Electrical Insulation*, vol. EI-14, no. 1, pp. 1-13, Feb. 1979, doi: 10.1109/TEI.1979.298198.

[3] Husain, E.; Nema, R. (August 1982). "Analysis of Paschen Curves for air, N2 and SF6 Using the Townsend Breakdown Equation". IEEE Transactions on Electrical Insulation, August 1982.

[4] V. Carboni, H. Lackner, D. Giri and J. Lehr, "The breakdown fields and risetimes of select gases under the conditions of fast charging and high pressures," PPPS-2001 Pulsed Power Plasma Science 2001. 28th IEEE International Conference on Plasma Science and 13th IEEE International Pulsed Power Conference. Digest of Papers (Cat. No.01CH37251), 2001, pp. 482-486 vol.1.

Compact and Efficient Mode Converter for HPEM Applications in L Band

Luciano Prado de Oliveira, Felix Vega, Abdul Rouf Baba, John J. Pantoja, Adamo Banelli, Chaouki Kasmi
Directed Energy Research Centre
Technology Innovation Institute
Abu Dhabi, United Arab Emirates
luciano.prado@tii.ae

Abstract— Many high-power microwave (HPM) sources, such as relativistic backward wave oscillators, magnetically insulated transmission-line oscillators, and magnetrons, use circular waveguides output. When the antenna to be used has a rectangular waveguide input a is required in order to make an efficient transition. Such converter must be compact, present high-efficiency conversion, and have low return loss. This paper presents a design adapting a custom size circular-TE_{11} pulsed-magnetron output waveguide, insulated in ceramic, to a standard WR650 TE10 waveguide, insulated in air. The device was designed based on the principle of LC matching on a rectangular waveguide and was manufactured using CNC technology. The measurements show that the device has a return loss (S_{11}) lower than -20 dB over a bandwidth of 400 MHz, centered around a central frequency of 1.3 GHz, at 1.3 MW peak power.

Keywords-mode converter; high-power microwave; HPEM.

I. DESIGN AND PROTOTYPE

The aim of this paper is to present the design and measurements of a TE_{10} to TE_{11} mode converter for high-power applications [1].

The power source is a 1-MW RK6517 magnetron oscillator operating in the L band. The magnetron output is a circular waveguide with a diameter of 75.4 mm, ceramic of unknown dielectric constant.

A classical stub-turner transmission line approach [2] was proposed as the solution to the problem. However, this required overcoming one of the most challenging tasks of the project: determining the impedance of the circular waveguide filled with a ceramic material of unknown permittivity. Two measurement methods were implemented: open-ended coaxial probe and cut-off frequency of circular waveguide. Both methods predicted an ε_r=6.5.

The designed mode converter (MC) consists of a rectangular waveguide WR650 (main transmission line) with one end connected directly to the circular waveguide through a custom-made flange on the transversal excitation plane. The remaining end was terminated on a standard rectangular flange, allowing the connection of the antenna. A stub waveguide was connected in parallel to the main transmission line. It consists of a WR650 segment, terminated in a short-circuit. The length and positioning of the stub were calculated to reduce the reflections back to the magnetron. The mode converter was designed with a return loss of less than -25 dB at 1.3 GHz.

The primary waveguide was manufactured in aluminium on a CNC with a total length of 202 mm. The 84.7-mm long stub was placed on one of the broad walls at 92 mm from the rectangular end.

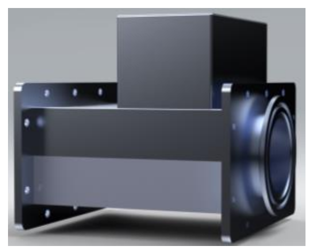

(a)

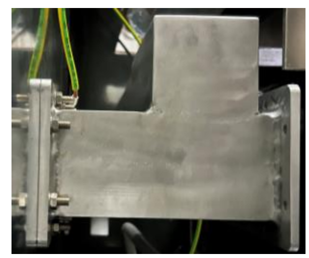

(b)

Figure 1. Mode converter. (a) model. (b) installed prototype.

III. RESULTS

The measurements of the manufactured MC, return loss and insertion loss, are shown in Fig. 2. As it can be seen, the mode conversion efficiency is higher than 97% over the frequency range from 1.28 to 1.32 GHz, with a return loss of less than -20 dB over the bandwidth. The conversion efficiency is about 99.3% at the central frequency, with a return loss of approximately −37 dB at 1.30 GHz.

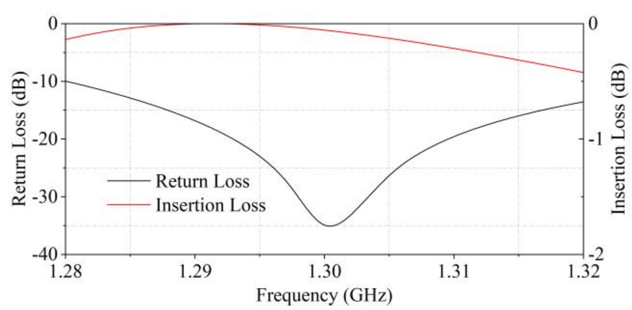

Figure 2. Mode converter's return loss and insertion loss.

REFERENCES
[1] "Susceptibility of Electronic Systems to High-Power Microwaves: Summary of Test Experience", *IEEE Trans. Electromagn. Compat,* vol. 46, No. 3, August 2004.
[2] D. M. Pozar, "Microwave Engineering," Ed. New York: John Wiley & Sons, 2011.

Single Layer Microstrip Gysel Combiner for High-Power CW Applications

B.Sugumaran(1), O.Silva(1), F.Vega(1),C.Kasmi(1)

(1) Directed Energy Research Center, Technology Innovation Institute, Abu Dhabi, United Arab Emirates
Bharathidasan.Sugumaran@tii.ae , Oliver.Silva@tii.ae , felix.vega@tii.ae , chaouki.kasmi@tii.ae

Abstract—This paper presents the design and simulation of a single layer broadband microstrip Gysel combiner for high-power, continuous-wave applications. The combiner is designed to operate in the 1.4 to 1.8 GHz frequency range, handling a combined output power of 500 Watts CW. The design is limited to a single layer microstrip to avoid complex mechanical fixtures keeping a compact size. Besides, it offers return loss lower than 20 dB and isolation between ports is 20 dB, according to simulation results. This is the first report on a high-power Gysel combiner that uses a planar and single layer microstrip approach.

I. INTRODUCTION

The Gysel power combiner [1] is often used for power applications due to its superior power handling capabilities and good thermal performance, when compared to Wilkinson power combiners [2]. Unlike the later, where the resistor is embedded into the network resulting in poor thermal dissipation, the Gysel uses two isolation resistors connected to the ground improving the thermal dissipation. The isolation resistors can be high power terminations, improving the suitability for high-power applications.

The general configuration of the 2:1 Gysel power combiner proposed in this paper is shown in Figure 1. The impedances and the length of the lines are calculated according to [2]. The combiner will be built on the RT6035HTC substrate, to take advantage of the high thermal conductivity and dissipation efficiency. The corresponding impedances for each line and its associated electrical length are described in the Figure 1.

II. SIMULATION RESULTS

The circuit was simulated in Keysight Advanced Design System (ADS). The results are shown in Figure 2. It can be seen that the isolation is better than 20 dB and the insertion losses are better than 0.3 dB in the band of operation, 1.4 - 1.8 GHz. It can also be seen that the S11 is less than -20 dB.

The expected resulted combined power, when applying 250 Watts to each input is 468 Watts. The efficiency of the combiner reaches 93.6%, with only 32W losses due to insertion and heating.

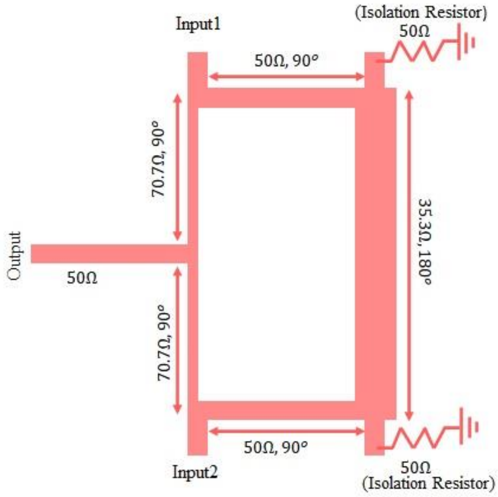

Figure 1: Architecture of 2 to 1 Gysel Power Combiner for port impedance of 50 ohms.

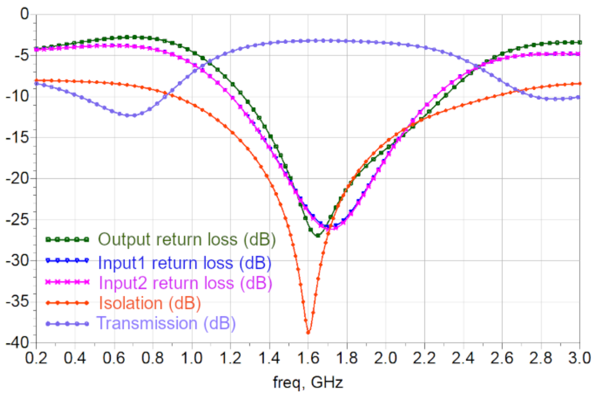

Figure 2 : Simulated result of Gysel Power Combiner.

REFERENCES

[1] U. H. Gysel, “A New N-Way Power Divider/Combiner Suitable for High-Power Applications”, 1975 IEEE MTT-S Int. Microwave Symposium. Dig., pp. 116-118.

[2] Veljko Crnadak and Siniša Tasić, ”VHF Gysel 3 dB Power Divider/Combiner” IcETRAN 2017, Kladovo, Serbia, June 05-08, ISBN 978-86-7466-692-0

An Unmanned Aerial Vehicle Platform for the detection of Landmines and IEDs using GPR

Asilah Al Mesmari(1), John J. Pantoja(1), Jesus Alvarez(1), Adamo Banelli(1), Felix Vega(1), Chaouki Kasmi(1)

(1) Directed Energy Research Centre, Technology Innovation Institute,

Abu Dhabi, United Arab Emirates

Asilah.almesmari@tii.ae

Abstract—In this paper, we present the status of an ultra-wide band ground penetrating radar system mounted on an UAV. The device has been designed for humanitarian demining operations. We describe the platform, the GPR, the method of detection and the integration of artificial intelligence-based algorithms for classification of the landmines. A set of preliminary results is also presented.

Keywords-component; Ground Penetrating Radar, Unmanned Aerial Vehicle (UAV), humanitarian demining, artificial intelligence

I. INTRODUCTION

One of the most promising tools for humanitarian demining is the Ground Penetrating Radar (GPR) [1]. Among the advantages of GPR are discrimination between landmines and metal fragments, reduction in detection time and reduction of false alarms.

However, one of the main challenges in humanitarian operations is the mobility of the operator and the demining tool over the landmine field.

In order to overcome this challenge, we propose to install the GPR on an aerial vehicle (UAV) platform, that will be remotely piloted, scanning the terrain at low altitude.

II. DESCRIPTION OF THE SYSTEM

The system consists of a UWB GPR, using a MIMO antenna system as operating between 900 MHz to 5 GHz. A set of six Vivaldi antennas are connected to a NanoVNA through a RF switch and a distribution network. See Figure 1 for reference.

The S matrix produced by the NanoVNA is processed by a set of digital filters for denoising. The resulting signal will be transmitted via a wireless link to a computational platform where a Machine Learning algorithm will process the signal, discriminating between landmines and clutter [2].

The system will be mounted on a DJI Matrice 600 UAV. The platform will scan a 1 x 1 square meter area in 10 minutes, which is 85% reduction time over the conventional process. The range of operation is 200 m, from the pilot.

Initial tests were done with the instrument to characterize the electromagnetic signature of real improvised explosive devices (IEDs) and landmines in a controlled environment. These results are presented in Figure 2.

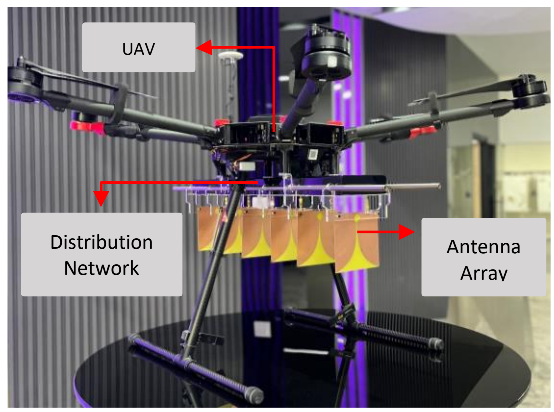

Figure 1. GPR setup mounted on an UAV with 6 antennas

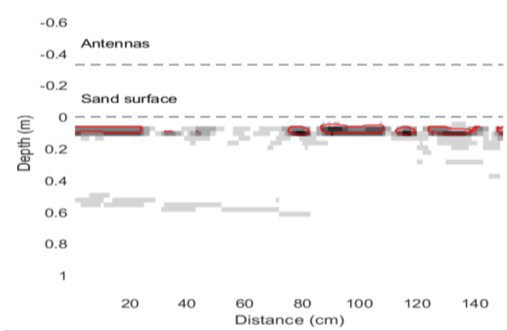

Figure 2 . Results data of soil detection measured in UAE desert

Above figure, is a radargram processed with background removal to create an environment where the sand is homogenous. The dark grey areas highlighted in red represents the variation of the objects buried, whereas the light grey areas are the interface of the next layer of sand.

REFERENCES

[1] M. Sato, Y. Hamada, X. Feng, F. Kong, Z. Zeng, G. Fang "GPR using an array for landmine detection" in Near Surface Geophysics, Vol 2, 2004, pp. 1 –8.
[2] S. Gutierrez et al., "Advances on the detection of Landmines and IEDs in Colombia using UWB GPR and Machine Learning Techniques," 2021 15th European Conference on Antennas and Propagation (EuCAP), 2021, pp. 1-4.

Fast L-band demonstrator for Remote Induction of Disturbance for Access Denial (RIDAD)

A. Banelli(1), J. Pantoja(1), L.Prado(1), A.R. Baba(1)
M. Al Mansoori (1), A. Almesmari (1), J. Alvarez (1), E. Neira(1), F. Vega (1), C. Kasmi(1)
(1) Directed Energy Research Center, Technology Innovation Institute, Abu Dhabi, United Arab Emirates
adamo.banelli@tii.ae

***Abstract*—**RIDAD, a prototype for a narrowband High Power Electromagnetic Radiator in the MW power range and operating at L-band using a pulsed Magnetron source is presented. The system is intended to demonstrate High Power Electromagnetic effects on electronic equipment and EMC studies. The electric and mechanic setup is shown and discussed.

Keywords: High-Power Electromagnetic Effects; HPEM; Pulsed Magnetron

I. INTRODUCTION

In this paper, a High-Power Electromagnetic Radiator (HPEM) operating in L band is presented. The system is intended as a cost efficient narrowband demonstrator for addressing high power electromagnetic effects on electronic equipment [1] .
Currently, possible High-Power sources include Klystrons (for MW range applications), Magnetrons and Solid-State technology: Solid-State amplifiers lack the capability of operating in the MW power range, while Klystron, although capable of higher power output, is less cost-effective compared to Magnetron.
The final architecture uses a Magnetron operating at 1.3GHz and is able to deliver more than 1 MW peak power. We'll describe the overall system architecture, consisting of pusled Magnetron, High-Voltage Pulse Modulator, Mode Converter and Antenna. Finally, test results are shown.

II. SYSTEM ARCHITECTURE

In Fig.1, the general architecture of the transmitter is presented: it comprises a High-Voltage Pulse Modulator and Peaking Box unit for high Voltage generation, Heater Power Supply and Magnetron; the Magnetron's output port is connected to the Radiator through a Mode Converter, which in our system is made by an L band Standard Gain Horn with an in-house design lens introduced to include the overall gain.
The final integrated system with antenna and directional coupler for power monitoring is shown in Fig.2.

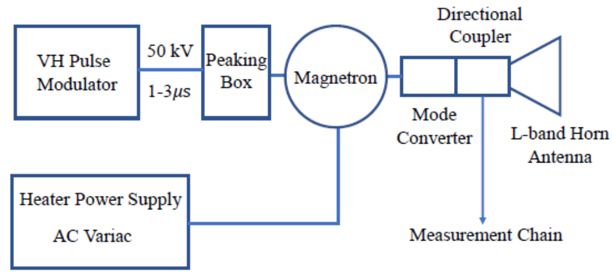

Figure 1. General System Architecture.

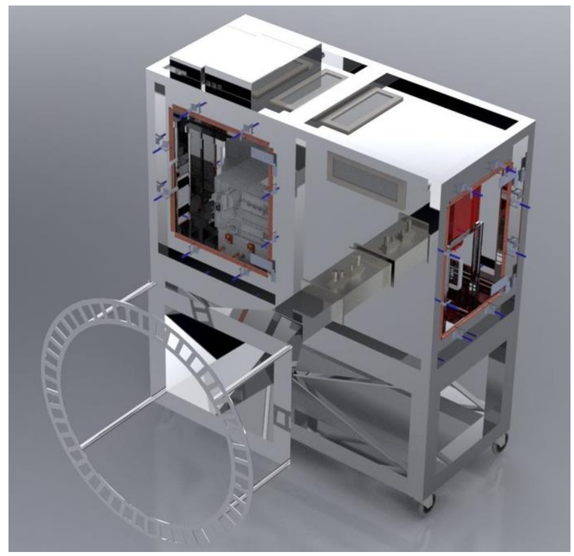

Figure 2. Integrated transmitter (shielded box) and radiator (horn and lens).

III. TEST RESULTS

The measured E-field at 6.8m is presented in Fig.3. The resulting Vfar from the test is 55kV.

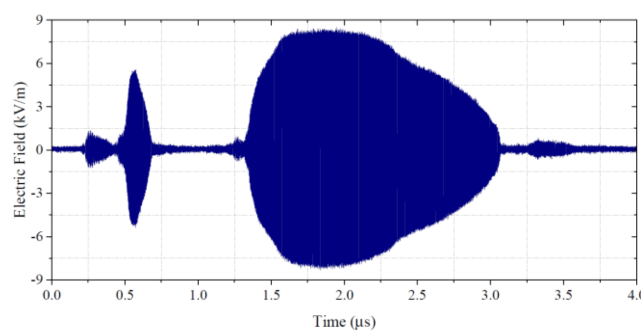

Figure 3. Measured E-Field.

REFERENCES
[1] M.G.Bäckström, K.G Lövstrand, "Susceptibility of Electronic Systems to High-Power Microwaves: Summary of Test Experience", *IEEE Trans. Electromagn. Compat,* vol. 46, No. 3, August 2004

Ant Nests detection under Forest Coverage by Drone Borne Radar Survey

Gian Oré[1], Alexandre Santos[2], Daniele Ukan[3], Ronald Zanetti[4], Mariane Camargo[5], Luciano P. Oliveira[6], Hugo E. Hernandez-Figueroa[1]

[1]School of Electrical and Computer Engineering, University of Campinas, UNICAMP, Campinas, Brazil
[2]Department of Forest Engineering, Federal Institute of Mato Grosso, IFMT, Campus Cáceres, MT, Brazil
[3]Department of Forest Engineering, UNICENTRO, Irati, PR, Brazil
[4]Entomology Department, Federal University of Lavras, DEN/UFLA, Lavras, MG, Brazil
[5]Klabin S/A, Telêmaco Borba, PR, Brazil
[6]Directed Energy Research Centre, Technology Innovation Institute, Abu Dhabi, United Arab Emirates

Abstract**—**This work presents unprecedented results for ant nest detection in industrial forests from data collected by a drone-borne tomographic radar. The data acquisition was carried out in commercial eucalyptus forests where several ant nests were identified. The P-band data were collected performing helical flight trajectories and SAR images were obtained using a fast back-projection algorithm. Then, a convolutional neural network was trained to estimate the ant nest locations, reaching a success rate of 80% in a validation dataset.
Keywords-SAR imaging; ant nest; tomographic mapping

I. INTRODUCTION

Leaf-cutting ants build underground nests, which are made up of chambers, and are dangerous for forest productivity. A 3-year-old nest can occupy an area of 100 to 200 m^2 and have chambers down to a depth of 7 m [1].

This article reports the results of the ant nest detection from remote monitoring carried out with a drone-borne tomographic radar performing helical trajectories to obtain tomographic information of the eucalyptus forest area. Finally, a convolutional neural network (CNN) is used to estimate the ant nest locations from SAR images.

II. METHODS

Five-year-old industrial eucalyptus forests belonging to the company Klabin were mapped with a multiband drone-borne tomographic radar [2]. From fieldwork in the monitored area, ant nest of different sizes was found and georeferenced using a conventional GPS for reference data. Five areas were mapped with helical trajectory flights ranging from 120m to 80m in height to obtain tomographic information. The data from the P band was processed using a fast back-projection algorithm [3]. For each area, a set of eight SAR images representing an area of 100x100m from the surface to 2.1m underground was obtained.

A CNN was proposed to detect ant-nests in SAR images. The five sets of SAR images were divided into sub-images of 12x12m with a stride of 4m, obtaining a total of 2420 sub-images sets of 60x60x8 pixels. The neural network has two convolutional layers of 9x9x64, a max-pooling layer, a convolutional layer of 5 x 5 x 128, a dense layer of 115200 neurons, a dense layer of 32 neurons, and an output layer of a sigmoid neuron. Hidden layers have a rectified linear unit (ReLU) as the function activation. The network was trained using the binary cross-entropy loss function and the Adam as the stochastic optimization method.

III. RESULTS

The training dataset comprises the sub-images sets of four areas, leaving one area for the validation dataset. The estimation of the ant nest position in the training dataset achieved a hit rate of 100% and a false alarm rate of 0%. The result of the validation dataset is presented in Figure 1.

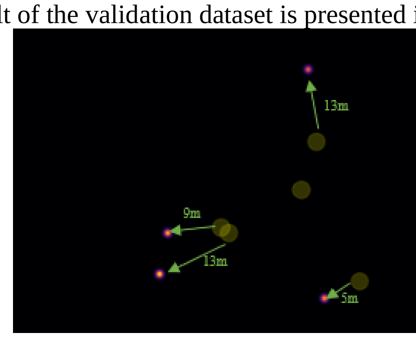

Figure 1. Ant nest's position: actual positions in yellow, estimated positions purple.

The results of the validation dataset have a planimetric error, which is the distance between the actual and estimated ant nest position, between 5 m and 13 m. A hit rate of 80% and a false alarm rate of 0% were achieved.

III. CONCLUSIONS

This paper presents the results of estimating the ant nest position from tomographic SAR images, showing that SAR systems have great potential for detecting ant nests in industrial forests. In future works, we hope to estimate the ant nest positions with a planimetric error of fewer than 5 m and a hit rate greater than 80%.

REFERENCES

[1] A. C. Swanson *et al.*, “Welcome to the Atta world: a framework for understanding the effects of leaf-cutter ants on ecosystem functions,” Functional ecology, vol. 33, no. 8, p. 1386 – 1399, 2019.

[2] L. Moreira *et al.*, “A Drone-borne Multiband DInSAR: Results and Applications,” 2019 IEEE Radar Conference, MA, USA, Apr. 2019, p. 1-6.

[3] J. A. Goes *et al.*, “Spiral SAR imaging with fast factorized back-projection: a phase error analysis,” Sensors, vol. 21, no. 15, p. 1 – 20, 2021.

State of the art on the use of Conductive Fabrics for Lightning Protection

John J. Pantoja, Felix Vega, Chaouki Kasmi
Directed Energy Research Center
Technology Innovation Institute
Abu Dhabi, UAE
john.pantoja@tii.ae

Abstract—In this paper we present a review on the research and developments of lightning protection based on conductive fabrics. Efforts to understand, model, test, and design materials based on conductive fabrics able to withstand intense current pulses, developed in the last decade, are discussed. Research work starting from conductive-fabrics electrical and thermal modeling to experimental results on new composites will be reviewed.

Keywords- conductive fabrics; conductive textiles; lightning strokes; lightning; lightning protection; woven fabric.

I. INTRODUCTION

Conductive fabric is a versatile material used in different applications including electromagnetic shielding, sensors, and wearables. Due to its capability to conduct intense current pulses and its low weight, another application that has drawn the attention lately is lightning strike protection. Lightweight components for lightning protection are required in oil tanks, aircrafts, portable shelters, and wind turbines, where conductive films and composite materials are being commonly used. In this talk, a review on the research findings and recent applications of conductive textiles for lightning protection is presented.

II. EXPERIMENTAL TESTS

Impulse experimental tests have shown that conductive fabrics can endure high current impulses. Different effects are obtained depending on the current level, fabric layers, weave pattern, and conductive material. These effects include melting, vaporization, and bursts at hot spots [1]. Based on a series of experimental tests with 10/350 μs current impulses, Roman et al. reported 2.5 kA/cm as the maximum lightning current density for one layer of rip-stop textile [2].

Some recent applications include the use of electrically and thermally conductive structural fabric to provide direct lightning strike protection on some areas of aircrafts and also electromagnetic shielding [3]. These characteristics are obtained with fibre and metallic-wire hybrid fabrics and interlaminar conductive nonwovens in carbon-fiber-reinforced-polymer laminates.

III. ELECTRO-THERMAL MODELING

Electrical models have been used to estimate the effects of intense current impulses on conductive fabrics. Based on experimental tests, the fabric resistance can be calculated and used to estimate the potential rise due to the impulse current [1]. Other studies look for the capacity to handle high impulsive currents. Scratches perpendicular to the current flow, initially denominated as "striation", were observed in impulsive tests on different kinds of conductive fabrics. These scratches, produced by the conductive layer evaporation, reveals that thermal dissipation and phase change were produced at hot spots, generating a non-linear behavior from the electrical point of view.

Striation on conductive woven fabrics is explained on [4] using an electrical equivalent circuit that considers yarns' contact resistance and its specific action required to reach melting, evaporation, and burst limits.

IV. CONCLUSION

Conductive fabrics are a promising component of future lightweight lightning protection systems that can be easily integrated to structural components. Experimental tests and theoretical and numerical models show that conductive fabrics can endure high density current levels; however, several conductive layers or large areas are required to withstand a direct lightning strike.

REFERENCES

[1] J. Cristancho, J. Rodríguez, C. Rivera, F. Roman, L. Herrera, and J. J. Pantoja, "Conductive Fabric Potential Rise due to Lightning Impulse Currents*," in 2019 Int. Symp. Lightning Protection (XV SIPDA),* 2019, pp. 1–6, doi: 10.1109/SIPDA47030.2019.8951605.

[2] F. Román et al., "10/350 μs Lightning Impulse Current Behavior of a Conductive Fabric," *2021 35th International Conference on Lightning Protection (ICLP) and XVI International Symposium on Lightning Protection (SIPDA)*, 2021, pp. 01-06, doi: 10.1109/ICLPandSIPDA54065.2021.9627391.

[3] B. Alemour, O. Badran, M. R. Hassan, "A Review of Using Conductive Composite Materials in Solving Lightening Strike and Ice Accumulation Problems in Aviation", J. Aerosp. Technol. Manag., vol. 11, pp. 1-23, 2019.

[4] J. J. Pantoja, J. Cristancho, J. Rodriguez, C. Rivera, F. Roman, F. Vega, Ch. Kasmi, and F. AlYafei, "Specific Action as a Metric to Determine Thermal Degradation of Conductive Fabrics Exposed to High Current Impulses," Progress. Electromagn. Res. C., vol. 105, pp. 59–72, 2020.

Cathode Edge Effect and Divergence of Emitted Electron Beams in Vircators

Moza S. Mohamed (1, 2), Evgeny A. Gurnevich(2), E. Neira (1), F. Vega(1, 3), and Chaouki Kasmi(1)
(1) Directed Energy Research Center, Technology Innovation Institute, Abu Dhabi, United Arab Emirates. http://www.tii.ae.
(2) Institute for Nuclear Problems, Belarusian State University, 220006, Minsk, Belarus
(3) Universidad Nacional de Colombia, Sede Bogotá, Colombia.
Moza.mohamed@tii.ae

Abstract—This paper analyses the beam imprint and beam microbeams of high explosive emission cathodes that are used in virtual cathode oscillators (Vircators). The results show the influence of the edge effect and how acquiring the microbeams' imprint can estimate the transverse momenta spread of the cathode beam.

Keywords-Vircators; Beam imprints; Explosive emission cathodes; Edge effect.

I. INTRODUCTION

The geometry and the material influence the homogeneity of the beam's current emitted by a cathode. In this paper we investigate the beam imprints of planar MPG-8 graphite cathode and carbon epoxy capillary cathode, Figure 1.

Figure 1 Planar MPG-8 graphite cathode (left). Smooth planar surface with capillaries attached to duralumin substrate (right).

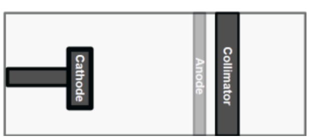

Figure 2 Experimental setup to obtain a full-beam imprint.

For the experimental procedure, an axial vircator was used. The experimental setup is shown in Figure 2. For obtaining the full beam imprint the radiochromic film was placed on top of the collimator overlooking the cathode. For obtaining the microbeams' imprint the film was placed behind the collimator. To calibrate the film a procedure similar to reference [1] was used.

II. RESULTS

A. *Beam imprint*

Figure 3 shows the imprint for the graphite cathode (left) and multi-capillary cathode (right). From the obtained prints we can see that the graphite cathode edges exhibit higher field strength than the centre of the emitting surface of the cathode this causes the dips in the centre of the cathode emitting surface. For the carbon epoxy multi-capillary cathode the beam imprint indicates a uniform distribution of the radiation dose (kGy) absorbed in the film over the electron-beam cross-section and had no dip in the beam density in the centre of the cathode.

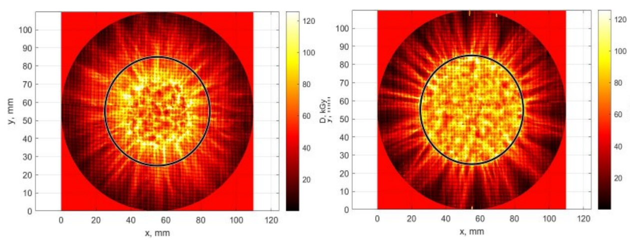

Figure 3 Beam imprint. Left is the planar MPG-8 graphite cathode and right is the multi-capillary cathode.

B. *Microbeams' imprint*

Using the pepper pot method [2], we obtained the beam imprint for the graphite cathode by measuring the displacement of the microbeams' centres relative to the centres of the collimating holes versus the hole position. From the microbeams' imprint, we were able to calculate the energy spread by calculating the characteristic angles of electron incidence on the anode surface based on the magnitudes of displacements and the thickness of the collimator (8mm). Results showed that the energy spread for the graphite cathode was approximately 16% this is considered really high but this is because graphite emitters have low uniformity [3].

III. CONCLUSION

To conclude, we highlighted the importance of the cathode emitter on its performance. Most importantly we experimentally determined the energy spread of the graphite cathode.

REFERENCES

[1] V. G. Baryshevsky *et al.*, "Generation of High-Current Electron Beams in Diodes With Large-Area Explosive Emission Cathodes," *IEEE Trans. Plasma Sci.*, vol. 44, no. 7, pp. 1103–1111, Jul. 2016, doi: 10.1109/TPS.2016.2572043.

[2] S. Barabin, A. Kozlov, T. Kulevoy, D. Liakin, A. Lukashin, and D. Selesnev, "Pepper-Pot Emittance Metasurements," *Proceedings of the 26th Russian Particle Accelerator Conf.*, vol. RUPAC2018, p. 3 pages, 0.540 MB, 2018, doi: 10.18429/JACOW-RUPAC2018-THPSC18.

[3] A. Roy, A. Patel, R. Menon, A. Sharma, D. P. Chakravarthy, and D. S. Patil, "Emission properties of explosive field emission cathodes," *Physics of Plasmas*, vol. 18, no. 10, p. 103108, Oct. 2011, doi: 10.1063/1.3646361.

Towards High-Power Microwaves

S. Anishchenko, V. Baryshevsky, A. Gurinovich,
E. Gurnevich, P. Molchanov, A. Rouba
Research Institute for Nuclear Problems of BSU
Minsk, Belarus
sergei.anishchenko@ephl.by, gur@inp.bsu.by

Abstract — In this paper, we review and compare high-power microwave (HPM) sources operating without a magnetic field to guide the electron beam that are capable of producing HPM pulses with a duration of about 100 ns. The proposed analysis summarizes multi-year research carried with three types of HPM sources: an axial vircator, a split-cavity oscillator and a virtual cathode oscillator in reflex triode geometry. These options were simulated for electron beam energy ~400 keV and for pulsers with demonstrated capability to provide HPM pulses with the required pulse duration. Designed sources were experimentally tested, and their advantages and weaknesses are discussed with respect to high output power, long pulse duration, and good operation stability.

Keywords-high-power microwaves; reflex triode; vircator; split-cavity oscillator

I. INTRODUCTION

The aim of the presented analysis is to compare HPM sources of different types and substantiate the choice of a source that will provide high output power, long pulse duration and good operation stability. The technical requirements for the HPM source are operation without a magnetic field and compact design. Single frequency operation during the 100 ns is desired. Three types of HPM sources were analyzed: an axial vircator, a split-cavity oscillator, and a virtual cathode oscillator in reflex triode geometry. The paper is organized as follows. Each HPM source is described in a separate section. Some general approaches and design solutions were applied to all of them – they are discussed in a particular section for one of the sources. Each section presents the experimentally obtained results and discusses the observed advantages and weaknesses of each source.

II. AXIAL VIRCATOR

Using [1] as a starting point for the development, we designed the axial vircator. In the simulation, it looked to be efficient, and the output power looked very promising. However, the experiments demonstrated low reproducibility of results [2]. The subsequent analysis [3] explained the unstable operation by high dependence of source efficiency on the spread of of the electron velocities in the beam.

III. SCO

The split-cavity oscillator, as proposed in [4], was designed to operate at 400 kV. Simulated and experimental results showed that the stability of the observed results was high, but the experimental results showed that the radiated power and pulse duration were low when compared to the simulation. Analysis of results enabled us to assume that pulse shortening was being caused by expanding plasma cloud, which is formed in the vicinity of extractor as a result of its being bombarded by electrons causing the beam to be compressed by its own magnetic field.

IV. REFLEX TRIODE

The virtual cathode oscillator in reflex triode geometry [5] demonstrated higher operation stability at high-power operation with longer pulse duration as compared with other sources. It provided good single frequency operation during the 100 ns pulse [6] (see Fig. 1). High operation stability was ensured by use of multi-capillary cathode [7].

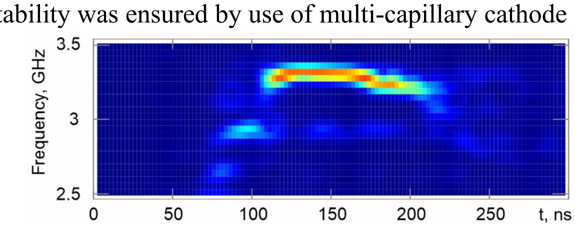

Figure 1. Shot-time fourier transform of HPM pulse

REFERENCES

[1] L. Zhi-Qiang et al., “Simulation and experimental research of a novel vircator,” Chin. Phys. Lett., vol. 25, no. 7, pp. 2566–2569, 2008.
[2] V. Baryshevsky, A. Gurinovich, E. Gurnevich, P. Molchanov, “Experimental study of an axial vircator with resonant cavity,” IEEE Trans. Plasma Sci., vol. 43, no. 10, pp. 3507–3511, 2015.
[3] E. Gurnevich, P. Molchanov, “The effect of the electron-beam parameter spread on microwave generation in a three-cavity axial vircator,” IEEE Trans. Plasma Sci., vol. 43, no. 4, pp. 1014–1017, 2015.
[4] B.M. Marder, “The split-cavity oscillator: a high-power e-beam modulator and microwave source,” IEEE Trans. Plasma Sci., vol. 20, no. 3, pp. 312–331, 1992.
[5] A.G. Zherlitsyn, G.V. Mel’nikov, P.Ya. Isakov, “Effect of feedback on the microwave radiation in a triode with a virtual cathode,” J. Commun. Technol. and Electron., vol. 52, no. 7, pp. 798–802, 2007.
[6] V. Baryshevsky, A. Gurinovich, E. Gurnevich, and P. Molchanov, “Experimantal study of a triode reflex geometry vircator,” IEEE Trans. Plasma Sci., vol. 45, pp. 631–635, 2017.
[7] J.Z. Gleizer, T. Queller, Yu. Bliokh, S. Yatom, V. Vekselman, Ya.E. Krasik, and V. Bernshtam, “High-current long-duration uniform electron beam generation in a diode with multicapillary carbon-epoxy cathode,” J. Appl. Phys., vol. 114, 123303, 2013.

Tolerances in Flux Compression Generator Design: Theory

S. Anishchenko, P. Bogdanovich, A. Gurinovich
Research Institute for Nuclear Problems of BSU
Minsk, Belarus
sanishchenko@mail.ru, gur@inp.bsu.by

Abstract— The physical properties of FCG components available on the market (wires, explosives, liners (armatures), etc.) might differ from those that were originally used for FCG design. As a result, the output parameters of the manufactured generator (e.g. maximum output power) could deviate from the pre-calculated values. Simple formulas are derived to enable evaluation of change in maximum output power of a helical flux compression generator due to variations in either wire insulation thickness or detonation velocity of explosive. The obtained formulas establish acceptable tolerances for FCG components produced by a third-party manufacturer.

Keywords-HFCG; FCG; tolerances; insulation thickness; detonation velocity

I. INTRODUCTION

The main features of FCGs invented in the 1950s are now well known [1–3]. The FCG design for a particular task is based on the use of well-developed theoretical models and numerical methods [4–7]. However, the physical properties of FCG components available on the market (wires, explosives, liner, etc.) might differ from those that were originally used for FCG design. As a result, the output parameters of the manufactured generator (e.g. output power) could deviate from the pre-calculated values. That is why, some simple formulas are derived to enable evaluation of change in maximum output power of a helical flux compression generator powering an inductive load due to variations in either wire insulation thickness or detonation velocity of explosive. The obtained formulas establish acceptable tolerances for FCG components produced by a third-party manufacturer.

II. INSULATION THICKNESS

The insulation thickness of wires produced even by the same manufacture can vary along wire length. As a result, wire diameter d and winding density differ from one inductor sample to another. This means that there is some spread in FCG inductance values $L_G(t)$ for different specimens.

Since the current amplification factor is mainly determined by the ratio of the initial FCG inductance L_0 to the load inductance L_l, one should expect a deviation of the generator output parameters from those declared during design procedure. For the exponentially decreasing FCG inductance $L_G(t)=L_0e^{-\alpha t}$ and resistance $R_G(t)=R_0e^{-\alpha t}$, the change in maximum output power ΔP_{max} is given by the following formula

$$\frac{\Delta P_{\max}}{P_{\max}} \approx -2\left(1-\frac{2R_0}{\alpha L_0}\right)\cdot\frac{\Delta d}{d} \tag{1}$$

Here, $\Delta d/d$ is a relative change of wire diameter.

III. DETONATION VELOCITY

A similar situation is observed with parameters of explosive used for liner filling. The detonation velocity might differ in different tests. The dependence of inductance derivative $dL_G(t)/dt$ on the detonation velocity v results in variations of the maximum output power:

$$\frac{\Delta P_{\max}}{P_{\max}} \approx \left[1+\frac{R_0}{\alpha L_0}\cdot\left(1+2\ln\frac{2L_0}{3L_l}\right)\right]\cdot\frac{\Delta v}{v} \tag{2}$$

Here, $\Delta v/v$ is a relative change in detonation velocity.

IV. RESULTS

Simple formulas enabling evaluation of change in maximum output power of a helical flux compression generator due to variations in either wire insulation thickness or detonation velocity of explosive are derived. The obtained formulas establish acceptable tolerances for FCG components produced by a third-party manufacturer.

REFERENCES

[1] A.D. Sakharov et al., “Magnetic cumulation,” DAN SSSR, vol. 165, no. 1, pp, 65–68, 1965.
[2] A.I. Pavlovsky, R.Z. Lyudaev, “Magnetic cumulation” in Issues of modern experimental and theoretical physics, Leningrad, Nauka, 1984.
[3] Magnetocumulatiove generators – pulsed energy sources. vol. 1, eds. V.A. Demidov, L.N. Plyashkevich, V.D. Delemir, Sarov, RFNC-VNIIEF, 2012.
[4] B.M. Novac, M.C. Enache, I.R. Smith, and H.R. Stewardson, “Simple 2D model for helical flux-compression generators,” Laser Particle Beams, vol. 15, no. 3, pp. 379 – 395, 1997.
[5] A.S. Pikar, N.Yu. Deryugin, P.V. Korolev, V.M. Klimashov, “The method for numerical modeling of magnetic field compression in HFCG,” Proc. Russian VI Zababahin's Sci. Readings, Sarov, Russia, 2001, pp. 38:1 – 38:5 [in Russian].
[6] D.E. Lileikis, “Numerical modeling of a helical, explosive flux compression generator,” in Proc. IEEE Conf. Rec. Plasma Sci., May 1997, p. 276.
[7] S.V. Anischenko, P.T. Bogdanovich, A.A. Gurinovich, and A.V. Oskin, “Simulation of helical flux compression generator,” IEEE Trans. Plasma Sci., vol. 46, no. 5, pp. 1859 – 1863.

A Concept for High-Power Radiator Based on the Dipole-Reflector-Director Configuration

M. AlMenhali(1), H.AlYahyaee(1), A. AlEbri(1),
A. Al Ali(1) , H. AlHammadi(1), M. AlYousef(1),
M. AlKaabi(1), Y. AlNuaimi(1), H. AlKetbi(1),
S. AlDahmani(1), F. Vega (1), C. Kasmi(1)

(1) Direct Energy Research Center, Technology Innovation Institute, Abu Dhabi, United Arab Emirates
Mariam.almenhali@tii.ae

***Abstract*—**This paper proposes a High-Power radiator, composed of a feeding dipole, a reflector, and a director plate. The dipole is fed through a controlled high-voltage pulse generator. By varying the dimensions of the plates and the distances between the elements of the system the influence of the reflector and director on the spectrum were studied.

Keywords: High Power Electromagnetics, Dipole, Reflector based antenna, Director

I. EXPERIMENTAL SETUP AND SIMULATION PROCESS

High-power single dipole antennas, connected to spark gap switches have been used as a feeding element in parabolic reflector-based high-power radiators [1] and [2]. The approach presented here explores the compactness and simplicity of using a flat reflector and a flat director plate. This approach requires, however, a better understanding of the influence of the relative dimensions of the system along with the distances between them, on the overall performance of the radiator. This system is demonstrated in Figure. 1.

The system is fed through an IAS [2] which consists of two electrodes with a 100 kV double exponential signal connected to the two dipole arms. The analysis will be performed with a fixed dipole length. The E-field produced by the system without the reflector and director was ~ 40 kV/m at 1 m.

The relative distances between the elements and the sizes of the plates were optimized based on the influence on the spectrum and the radiated field. The influence on the bandwidth was of interest and is shown in Figure. 2 for two different cases with a variation in L1 and L2. A soft computing algorithm will be used as an optimization tool.

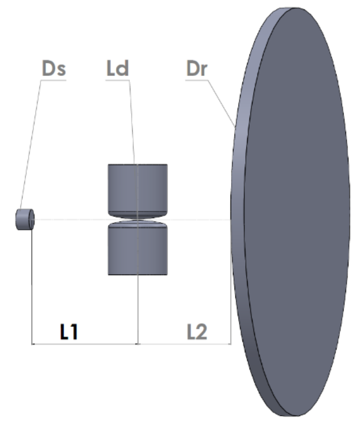

Figure 1 Proposed layout. The parameters L1, L2, Ld, Dr and Ds were optimized in order to maximize the radiated signal in boresight

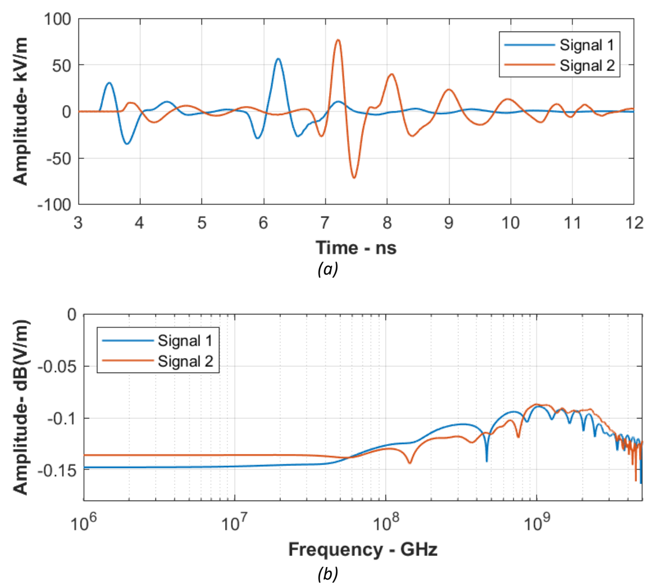

Figure 2 In signal 1, Dr and L2 are 10 mm and 360 mm respectively whereas in signal 2, they are 130 mm and 510 mm, L2 and Ds were kept constant in this case. (a) Time domain signal at 1 m, the amplitude of the radiated field is increased by approximately 25% due to the change in the dimensions listed above. (b) Moreover, the spectrum has changed due to the variation in dimensions, as shown above, the energy is more distributed in signal 2, whereas the bandwidth seems to be narrower in signal 1.

REFERENCES

[1] J. Ryu, J. Lee, H. Chin, J. Yeom, H. Kim, H. Kwon, S. Han and J. Choi,“A high Directive Paraboldial Reflector Antenna for High far Voltage in an Ultra Wideband Source System,” *IEEE Trans. Plasma Sci.*, vol. 41, no. 8, pp. 2283–2290, Aug. 2013.

[2] J. Ryu and J. Lee, “An integrated antenna-source system of very high ultra wide-band gain for radiating high power wide-band pulses,” *IEEE Trans. Plasma Sci.*, vol. 40, no. 4, pp. 1019–1026, Apr. 2011.

Effect of the Electrode Geometry on the Radiation Performance of a High-Power Dipole Antenna

A. Alebri (1), A. Al Ali (1), H. AlHamaadi (1),
H. Alyahyaee (1), M. Almenhali (1), M. Al Yousef (1),
M. Al Kaabi (1), Y. Al Nuaimi (1), H. Al Ketbi (1),
S. Al Dahmani (1), F. Vega (1), C. Kasmi (1)
(1) Direct Energy Research Center, Technology Innovation Institute, Abu Dhabi, United Arab Emirates
Ahmed.AlEbri@tii.ae

***Abstract*—This paper studies the influence of the geometry of the electrodes of the spark gap used in a dipole antenna for high-power UWB applications. The efficiency of radiation is illustrated through simulations and experiments.**

Keywords: Hertz Antenna, Spherical electrodes, Rogowski electrodes, Flat electrodes, Bruce electrodes, Hemisphere electrodes, EM Radiation.

I. INTRODUCTION

Dipole antennas have been proposed as a source of electromagnetic radiation in High Power applications [1], [2]. The radiator consists of a pressurized spark gap, fed by a pulsed high voltage source. The electrodes of the spark gap connected to the arms of a dipole, as illustrated in Figure 1.

The electrodes of the spark gap are, generally, designed taking into consideration the electric field distribution in electrostatic conditions. However, little attention has been given to the effect that the shape of the electrode has on the radiated signal, i.e. initial risetime, bandwidth, etc.

In this paper we'll study the field radiated by a normalized dipole under different spark gap electrodes, namely: Bruce, Rogowski, Flat, Hemisphere and Spherical. See Figure 2 for illustration.

II. Experimental Setup & Simulation

The simulation setup consists of a set of three dipole antennas with different length to diameter ratio. For each one, five different electrodes have been designed. The gap distance L_2 is held constant in all the cases. The spark gap was excited using double exponential signal from a HV pulser at constant rise/fall time and peak voltage. See Figure 3 for illustration.

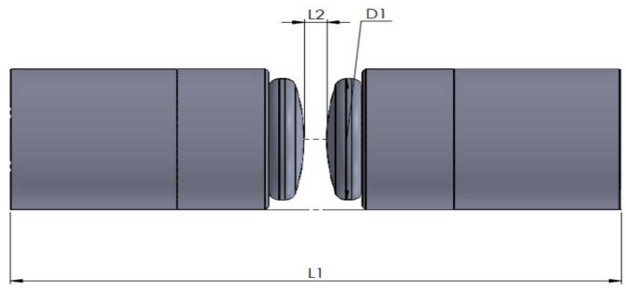

Figure 1 Electrodes of a spark gap connected to the arms of a dipole

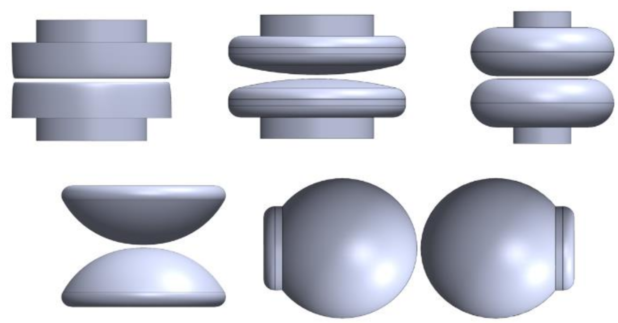

Figure 2 Electrodes shapes: Rogowski electrodes, Bruce electrodes, Flat electrodes, Hemisphere electrodes, Spherical electrodes respectively.

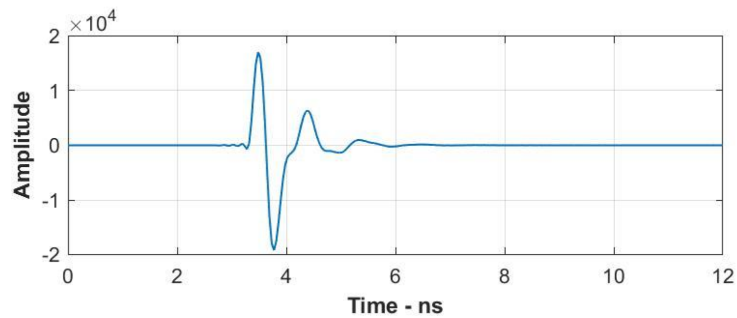

Figure 3 Example of the radiated electric field, normalized at 1(m). The peak voltage at the excitation is 50kV, the rise time is 500 ps.

REFERENCES

[1] J. Ryu, J. Lee, H. Chin, J. Yeom, H. Kim, H. Kwon, S. Han and J. Choi,"A high Directive Paraboldial Reflector Antenna for High far Voltage in an Ultra Wideband Source System," *IEEE Trans. Plasma Sci.*, vol. 41, no. 8, Aug. 2013.

[2] J. Ryu and J. Lee, "An integrated antenna-source system of very high ultra wide-band gain for radiating high power wide-band pulses," *IEEE Trans. Plasma Sci.*, vol. 40, no. 4, Apr. 2011.

Semi-analytical gray-box modeling of an impulse radiating antenna

E. Le Boudec, F. Rachidi
Electromagnetic compatibility laboratory
Ecole polytechnique fédérale de Lausanne
Lausanne, Switzerland
elias.leboudec@epfl.ch

M. Rubinstein
University of Applied Science of Western Switzerland
Yverdon-les-Bains, Switzerland
marcos.rubinstein@heig-vd.ch

F. Vega, N. Mora
Directed Energy Research Centre
Technology Innovation Institute
Abu Dhabi, United Arab Emirates

***Abstract*—The time-domain cartesian multipole expansion allows to express electromagnetic fields radiated by localized current distributions as semi-analytical expressions. In this work, we find such expressions for the electric field radiated by an impulse radiating antenna (IRA), thanks to a formulation as an inverse problem.

model fitting; multipole expansion; impulse radiating antenna; inverse problem; analytical solutions

Analytical expressions for the fields emitted by impulse radiating antennas are limited to the boresight cylinder [1]. In this paper, we propose to generalize such expressions to the whole space thanks to a "gray-box" modeling approach, i.e., we fit experimental data to a model whose physical behavior is known, but specific parameters are not.

The antenna is modeled by a time-domain multipole expansion [2] in cartesian coordinates. This approach delivers semi-analytical expressions for the electric and magnetic fields radiated by a pulsed, spatially-localized source in a isotropic and homogeneous medium. It works by approximating the true source current density by a sum of equivalent time-depend multipole moments. As the number of multipole moments approaches infinity, the resulting field converges to the true field outside of the source region.

The inverse problem can be stated as follows: given time-domain field measurements $\mathbf{E}_i$ at a number of observation points $\mathbf{r}_i$, find the parameters of the multipole expansion which best fit the measurements. These parameters can be represented by a single vector $\mathbf{x}$, containing the equivalent source location $\mathbf{r}_0$, the amplitudes of the current moments $C_\alpha^{\mathbf{J}}$ for all multi-indices α whose order is below a certain limit, and the time-domain shape of the current excitation h_j evaluated at the discrete time-points t_j. From these parameters, the multipole expansion can be seen as a function mapping the parameters $\mathbf{x}$ to a predicted field $\widetilde{\mathbf{E}}_i(\mathbf{x})$. The inverse problem can thus be expressed as the minimization problem

$$\text{minimize}_{\mathbf{x}} \sum_i \|\mathbf{E}_i - \widetilde{\mathbf{E}}_i(\mathbf{x})\|_p^p \tag{1}$$

where the integer p is the norm order.

In this work, the measurements $\mathbf{E}_i$ have been simulated by a time-domain COMSOL simulation of an impulse radiating antenna excited by the second-order derivative of a gaussian pulse. The geometry of the problem is presented in Fig. 1. For simplicity, the matching impedances where ignored. Next, the parameter vector $\mathbf{x}$ is found by solving the unconstrained problem posed in Eq. 1 using the BFGS algorithm.

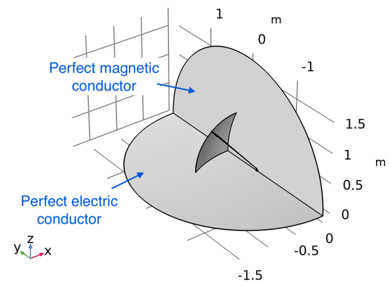

Figure 1. Geometry of the COMSOL simulation domain.

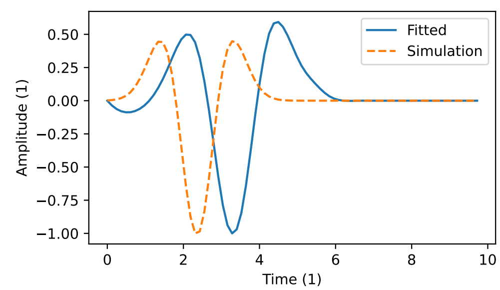

Figure 2. Time-domain shape of the current excitation fed to the COMSOL simulation (dotted line) and reconstructed by the model (solid line).

Over a full solid angle, the proposed method allows to explain over 80 % of the signal energy, thanks to a fifth order multipole expansion. Moreover, the used excitation is successfully recovered by the algorithm, albeit with some deformation and delay (see Fig. 2). Compared to traditional methods, both the advantages and disadvantages of the proposed approach lie in its reliance on the data and its "gray-box" modeling approach: indeed, its suffers from a slow convergence, but on the other hand, it is by design faithful to the measurements.

REFERENCES

[1] O. Mikheev, S. Podosenov, K. Sakharov, A. Sokolov, Y. Svekis, and V. Turkin, "New method for calculating pulse radiation from an antenna with a reflector," *IEEE Transactions on Electromagnetic Compatibility*, vol. 39, no. 1, pp. 48–54, Feb. 1997.

[2] A. Shlivinski and E. Heyman, "Time-domain near-field analysis of short-pulse antennas I. Spherical wave (multipole) expansion," *IEEE Transactions on Antennas and Propagation*, vol. 47, no. 2, pp. 271–279, Feb. 1999.

GLOBALEM 2022 - Laser generated EMP at LMJ-PETAL facility

EMP mitigation and equipment protection

B. Etchessahar, S. Coudert, J. Lagarde
CEA, CESTA,
F-33116 Le Barp, France
bertrand.etchessahar@cea.fr

S. Bazzoli, S. Darbon, M. Briat, C. Rubbelynk, O. Dubos
CEA, DIF, Bruyères-le-Châtel
91297 Arpajon Cedex, France

M. Bardon
CELIA (University of Bordeaux, CNRS, CEA)
Talence, France

N. Rameau, T. Gontier
CEA, Le Ripault,
BP16 - 37260 Monts, France

Abstract — Electromagnetic pulses (EMP) present a serious threat for operation of high-power, high-energy laser facilities. Here, we present the strategy implemented to manage these risks on the LMJ-PETAL large-scale facility that combines high-energy nanosecond laser beams and high-power picosecond beam. It is based on a dual approach: mitigation of the EMP emission and protecting the vulnerable devices. On one hand, the EMP emission is mitigated with a resistive and inductive target holder designed to reduce the current discharge. It has been tested and validated in experiments showing the efficiency of this device in the kJ/ps laser power range, with a reduction by a factor of 3 on the emitted EMP. On the other hand, the protection of the vulnerable equipment of the facility also rests on in the classical ElectroMagnetic Compatibility (EMC) technics: shielding of the devices, shielding and filtering of the cables. We present here the example of the innovative protection of the LMJ-PETAL VISAR (Velocity Interferometry System for Any Reflector) diagnostic, based on a Radiation-Absorbent Material (RAM) that was designed by simulation and qualification experiments.

Key words: EMP, Laser, EMC, mitigation, protection

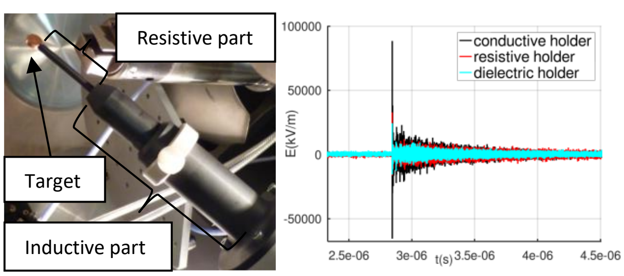

Figure 1. a) The mitigation device under test at CEA, DIF, Equinox facility. b) Time domain measurement of the EMP at CEA, CESTA, LMJ-PETAL facility.

The PETAL project has been performed by the CEA ("maître d'oeuvre") under the financial auspices of the New Aquitaine Region in France ("maître d'ouvrage", project owner), the French Government and the European Union and the scientific support from the Institute of Lasers and Plasmas. The Laser MegaJoule facility (LMJ) is a key component of CEA/DAM Simulation Program.

I. INTRODUCTION

The LMJ-PETAL nanosecond laser beams (300 kJ/3 ns in 2022) and picosecond beam (400 J/0.6 ps in 2022) are able to generate MV/m EMP in the GHz range inside the interaction chamber. This giant EMP may produce equipment failures and damages, and spurious signals in diagnostics. A dual approach, based on mitigation of the EMP emission and protection of the equipment, keeps the facility safe face to this threat and prepares it to the future energy upgrade of the LMJ and PETAL beams.

II. MITIGATION DEVICE

A. Main idea of the mitigation strategy

The main mechanism of the EMP generation is the induction of a discharge current through the target holder by the charge ejection from the laser-target interaction [1]. Our new resistive and inductive target holder (fig. 1a) reduces this return current, leading to a mitigation of the emitted EMP [2].

B. Recent developments on the mitigation device

A new resistive material (compound of polymer matrix and carbon nanotubes, made by mixing and injection molding) has been developed to play the role of the resistive part of the mitigation device. It has been successfully tested on several LMJ-PETAL shots in 2022 (fig. 1b).

III. EQUIPMENT PROTECTION

A. Key principles of the device protection

The susceptibility threshold of the most critical electrical devices of the facility has been deduced from experimental studies conducted with a high field pulsed generator. In order to keep the EM constraint under these thresholds, the vulnerable devices are set in Fadaray cages and cables are shielded or filtered.

B. Example of the VISAR diagnostic protection

The analysis table of the VISAR needs to be closed to the interaction chamber and bound to it through a metallic tubing for laser safety. A RAM has been added in the tubing and successfully mitigates the pulse propagation to the diagnostic shielded room.

REFERENCES

[1] F. Consoli *et al.*, High Power Laser Sci. Eng. 8, e22 (2020)
[2] M. Bardon *et al.*, Phys. Rev. Res. 2, 033502 (2020)

IEMI Detection

Setting up relevant detection threshold

Ribière-Tharaud N., Joly J.-C., Laparro C.
CEA, DAM, GRAMAT
F-46500 Gramat, France
nicolas.ribiere-tharaud@cea.fr
Schutz M., Lenoir B.,
Inoveos
F-19100 Brive-la-Gaillarde, France

Abstract— This paper presents the work carried out in order to set up the detection threshold (DT) of an Intentional Electromagnetic Interference (IEMI) detector developed with cost and performance requirements for the protection of civilian critical infrastructures (CCI). Considering actual electromagnetic environments (EME), the chosen DT has to ensure efficient detection and to avoid multiple false alarms.
(key words) Critical Infrastructure, IEMI, Vulnerability, Detection, Threshold detection level, Protection.

I. INTRODUCTION

Several research projects have been funded to improve the security of CCI considering events such as terrorist attacks, natural events and others. These projects raised the need of monitoring solutions involving several kinds of sensors and among them IEMI detectors have been studied [1][2]. Some have also been developed and tested in other frameworks, such as the TotEM^{TM} [3] and the EMPRIMUS [4] detectors. The prototype presented in [5] is a compact IEMI sensor with good abilities dedicated to signal discrimination but at low cost in order to facilitate wide deployment on CCI. This paper aims at describing the whole process established to take into account the electromagnetic environments (EME) and to reduce the false alarm rate.

II. DETECTION SYSTEM

The considered detection system includes four high dynamic range RF receiving channels combined to protection components in order to resist to high-level electromagnetic fields. Each channel covers one part of the detector whole frequency range (0.1 – 8GHz). Received signal on each channel is sent to a signal-processing unit. Signal processing allows recovering detected signal level (few V/m up to few 10thkV/m), repetition rate (mono pulse to ~100kHz), pulse width (1ns to 1ms), and impacted frequency channels.

III. SIGNAL DISCRIMINATION

Wide detection capabilities and resilience are mandatory detection system characteristics. However, in an increasingly saturated EME it is also required to be able to discriminate the variety of possible IEMI [6]. The signal discrimination is achieved through two complementary approaches:

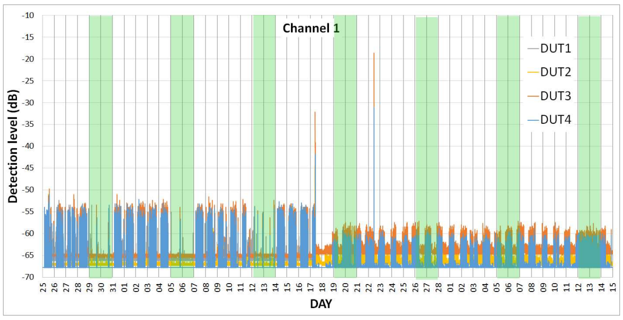

Figure 1. Detected EME in working area, 4 Detectors Under Test (DUT). Green frames highlight days off

1) EME characterization done by the detector itself. It consists in a specific detection mode where the electromagnetic field viewed from each detector channel is stored on long user-defined period (Fig. 1). A threshold can then be chosen at a level greater than the maximum electromagnetic field stored avoiding thus to trigger alarms related to the ambient electromagnetic field.

2) A rudimentary waveform analysis based on a set of criteria (electric field level, repetition rate, pulse duration, bandwidth). The detector is in the detection mode. In case of detected signal, an analysis relying on comparison of the measured signal characteristics to waveforms considered as unusual is achieved to trigger or not the alarm.
Both approaches have been assessed in laboratory and real conditions (several weeks, Fig. 1 and 2) to confirm the approaches relevance in terms of low false alarm rate and detector performances and repeatability.

Figure 2. Testing detector results dispersion

REFERENCES

[1] N. Ribière-Tharaud, and al., “PROGRESS project: Vulnerability and protection of GNSS ground-based infrastructures” EUROEM, London, 2016.
[2] J. F. Dawson, and al., “A Cost-Efficient System for Detecting an Intentional Electromagnetic Interference (IEMI) Attack”, International Symposium on Electromagnetic Compatibility (EMC Europe 2014), Sweden, September 2014
[3] D. Herke, L. Chatt, B. Petit and R. Hoad, “Lessons Learnt From IEMI Detector Deployments”, EUROEM, London, 2016
[4] Emprimus, LLC, www.emprimus.com
[5] N. Ribière-Tharaud, and al., “Affordable IEMI detection system for critical infrastructure protection”, AMEREM, Santa-Barbara, 2018
[6] A. Kreth, and al., “Characteristic HPEM Signals for the Detection of IEMI Threats”, Ultra-Wideband, Short-Pulse Electromagnetics, 10, Springer, 2014

On the use of the Gabor Transform to Study the Instability Growth Time in Vircators

Nouf AlEissaee(1), E. Neira(1), F. Vega(1), C. Kasmi(1)(2),
(1)Directed Energy Research Centre, Technology Innovation Institute, Abu Dhabi, United Arab Emirates
(2)Faculty of Electrical Engineering, Helmut Schmidt University, 22043 Hamburg, Germany
Masdar City, Abu Dhabi, United Arab Emirates
E-mail: Nouf.AlEissaee@tii.ae

Abstract—This paper proposes the use of the Gabor transform to determine the instability growth time in the signal produced by a Vircator. We'll describe the theory and parametrization of the Gabor transform and we'll apply it to a signal radiated by a vircator. The results will be compared with more traditional methods based on dimensional analysis and with other wavelet-based methods.
Keywords: Gabor transform, Instability growth time, Reflex triode

I. Introduction

In a High- power source, the instability growth time (T_{gt}) can be defined as the rate from the beginning of radiation (linear stage) to the non-linear saturation stage [1]. A preliminary estimate of the instability growth time is important when designing high-current generators, since the total beam duration must substantially exceed *T*. Otherwise, the generation simply will not have time to develop.

In this paper, we propose the use of the Gabor transform applied to the radiated electric field in order to estimate the instability growth time. This transform, named after Dennis Gabor, is a short-time Fourier transform representing a time function in time and frequency simultaneously. [2]

II. Methodology

We'll use the Discrete Gabor Transform (DGT) applying the methodology presented in [2]. In DGT, a Gaussian window will be multiplied by the function in time domain, and the resulting will be transformed using a classical Fast Fourier transform. The result will be plotted in a time-frequency diagram, where the magnitude of the frequency component will be expressed as a color code.

The DGT can be expressed by

$$s(t) = \sum_{m=-\infty}^{\infty} \sum_{n=-\infty}^{\infty} C_{m,n} h_{m,n}(t) \qquad (1)$$

where $C_{m,n}$ are the Gabor coefficients and $h_{m,n}(t)$ is the synthesis function, as in reference [2].

III. Experiment setup

The experimental setup is similar to the one presented in [4]. The radiated electric field *E(t)* was measured from a Reflex Triode and it's shown in Figure 1. The Gabor transform of *E(t)* is shown in Figure 2.

As it can be seen in Figure 2. there are two modes: parasitic mode and basic mode. The basic mode, containing most of the energy, occurs from 3.2 GHz to 3.4 GHz. The instability growth time can determined from the figure is around (~70 ns), which coincides with the theoretical results.

A Continuous Wavelet Transform (CWT) and Wavelet Synchrosqueezed Transform (WSST) were also computed. It was concluded that DGT is sharper and more precise than the other wavelets. Also, in DGT, the oscillation modes can be observed easily.

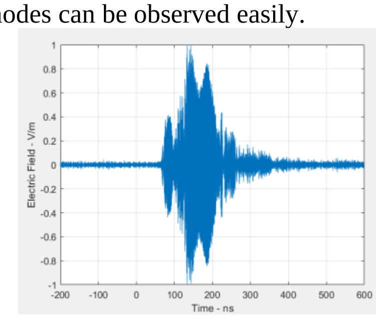

Figure 1. Normalized electric field

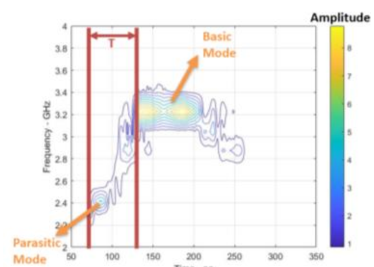

Figure 2. Gabor transform

REFERENCES

[1] H. Sze, D. Price, W.-yong Woo, D. Fittinghoff, and J. Benford, "Cavity Vircator amplifier - priming and phase locking of High Power Vircators," *SPIE Proceedings*, 1988.

[2] S. Qian and D. Chen, "Discrete Gabor transform," in IEEE Transactions on Signal Processing, vol. 41, no. 7, pp. 2429-2438, July 1993, doi: 10.1109/78.224251.

[3] L. Søndergaard, P., 2022. [online] Ltfat.org. Available at: <https://ltfat.org/doc/ltfat.pdf> [Accessed 14 June 2022].

[4] V. Baryshevsky, "Experimental Study of an Axial Vircator With Resonant Cavity," *IEEE Transactions*, vol. 43, no. 10, p. 3507.

Climate Change and its Impact on Lightning Protection Practices

HARTONO Zainal Abidin
Lightning Protection Consultant
Kuala Lumpur, Malaysia
zahartono@ieee.org; zahartono@gmail.com

Abstract—Climate change has resulted in more frequent thunderstorm occurrences in the temperate zones and in desert regions where lightning activity is lower compared to the equatorial regions. Buildings and structures that do not have effective lightning protection systems will be more impacted by lightning strikes than in the recent past. The IEC 62305 standard provides an effective lightning air terminal (i.e. lightning rod) placement method that can be applied on buildings with either simple or complex geometries. However, buildings that have been installed with non-conventional lightning protection systems, such as the Early Streamer Emission (ESE) air terminals, will experience more damages as these systems have already been proven as not effective for over 25 years.

Keywords – lightning protection; Collection Surface Method; lightning interception; air terminal; bypass; Early Streamer Emission.

I. INTRODUCTION

Climate change has resulted in more thunderstorms occurring in the temperate zones and even in desert regions. This has resulted in an increase in the occurrences of catastrophic flash floods, tornadoes, lightning, and wildfires in some countries.

Consequently, buildings and open spaces in those areas are now at higher risk of being struck by lightning if they are inadequately protected against this dangerous phenomenon. Fortunately, our understanding of lightning protection practices has been significantly improved by scientific research conducted around the world, particularly in areas with high lightning activity such as the tropical and equatorial regions.

Some of the results of these research activities have been incorporated into lightning protection standards such as the IEC 62305 which was published in 2006 by the International Electrotechnical Commission (IEC). The application of this standard in full can significantly improve the protection of buildings, structures and open spaces from lightning strikes.

II. THE IEC 62305 STANDARD

The IEC 62305 standard provides simple yet effective air terminal (i.e. lightning rod) placement methods that can be applied on any building or structure that are exposed to lightning. These methods have earlier been applied in some national lightning protection standards that have now been replaced by the IEC 62305, and in the current American standard NFPA780.

A. Air Terminal Placement Methods

The IEC 62305 mentioned three well established methods for designing air termination networks. They are:
(a) Protection Angle Method (G. Lussac, 19th century),
(b) Mesh Method (J. C. Maxwell, 19th century) and
(c) Rolling Sphere Method (T. Horvath, 1960).

The Rolling Sphere Method is suitable for identifying all the exposed building surfaces that are at risk of being struck by lightning. However, this method is unable to detect the high-risk locations where lightning has been frequently intercepted which resulted in *bypasses* (i.e. damages due to lightning strikes).

To overcome this detection problem, the IEC 62305 standard also provides a basic guide for the placement of air terminals to effectively intercept the lightning bolt. This guide is based on the latest air terminal placement method known as the Collection Surface Method (Hartono & Robiah, 1995, 2000) [1, 2].

B. The Collection Surface Method

This method was developed based on statistical analysis of observed bypasses on high-rise buildings in the very high lightning activity zone found in Kuala Lumpur and Singapore. It is based on the Rolling Sphere Method but instead of focusing on the surface of the imaginary sphere, the Collection Surface Method focused on the center of the sphere as it is rolled over the surface of the building.

The center of the sphere will generate an imaginary surface for every point on the physical surface of the building and the size of the imaginary surface correspond to the risk of that point being struck by lightning. It was found that corners, exposed points and edges have higher collection surfaces than flat surfaces. This method was proved to be able to predict the effective positions of the air terminals by lightning experts from Australia. [3]

The method was first applied in the revised Australian standard, AS1768, in 2003 [4]:

Field data of damage caused by lightning flashes terminating on structures identify the parts that are vulnerable to strikes. The most vulnerable, associated with over 90% of observed lightning damage, are nearly always located on upper parts of structure, such as—
(a) pointed apex roofs, spires and protrusions;
(b) gable roof ridge ends; and
(c) outer roof corners.

The Collection Surface Method was later applied in the IEC 62305 [5] after it was examined by the IEC Technical Committee No. 81:

Air-termination components installed on a structure shall be located at corners, exposed points and edges (especially on the upper level of any facades) …

Following the publication of the IEC 62305, Czech [6] and German [7] lightning experts developed software based on the Collection Surface Method that can predict the lightning strike location on any complex shaped building. They also suggest that applying the method in full compliance with the standard can provide up to 98% lightning interception efficiency.

III. COMMON ERRORS IN AIR TERMINAL PLACEMENTS

Air terminals that have been positioned not in full compliance with the IEC 62305 standard have repeatedly failed to intercept the lightning stroke, and this led to the occurrences of bypasses [8]. More than 90% of buildings in Malaysia have been installed with conventional air terminals that were not positioned according to the standard.

The reasons given for these failures are that the engineers who designed the air termination systems falsely believed that air terminals, conventional or non-conventional, can attract lightning and so the air terminals can be positioned anywhere on the exposed surface. This is partly due to the false belief being published in a book and taught in various local universities [9]. Consequently, some of them failed to understand the basis for air terminal placement according to the standard. Furthermore, most of them do not have any access to the past and/or present lightning protection standards for their study and reference.

Figure 1. Example of an air terminal (arrowed) incorrectly positioned away from the ridge end of the roof where a bypass (circled) had occurred.

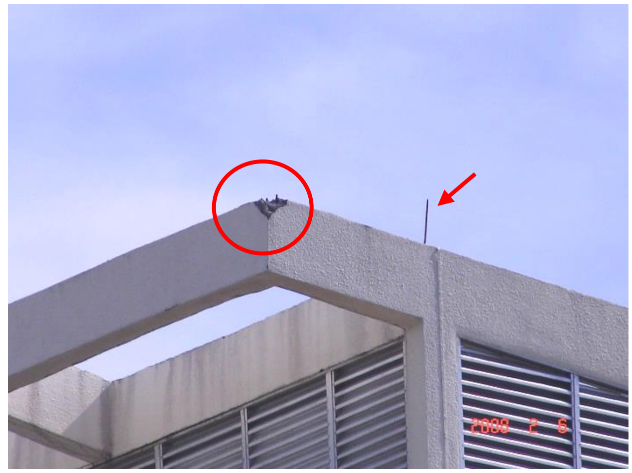

Figure 2. Example of an air terminal incorrectly positioned away from the outer corner of the roof where a bypass had occurred.

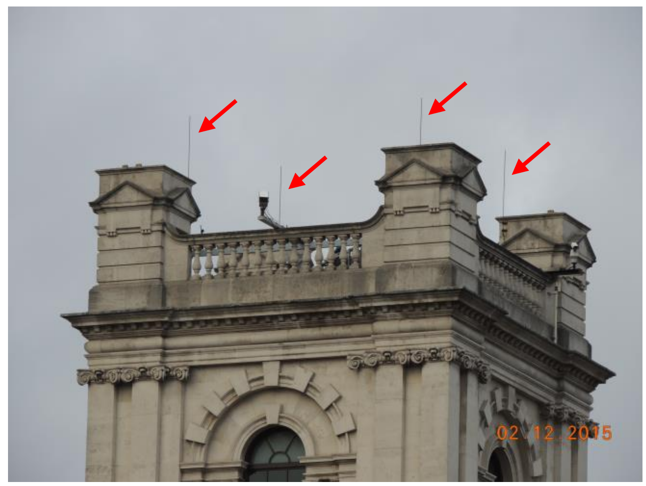

Figure 3. Example of air terminals incorrectly positioned at the inner corners instead of the outer corners of the roof.

Figure 4. Example of a major bypass on an unprotected part of a roof firewall.

Figure 5. Example of a minor bypass on a roof firewall installed with an air terminal positioned not in accordance with the IEC 62305 standard. If the air terminal had been positioned at the end of the firewall, the bypass could have been prevented.

IV. ALTERNATIVE FORMS OF CONVENTIONAL AIR TERMINALS

In some countries, the conventional lightning rod is synonymous with the cylindrical shaped metallic conductor with a pointed or blunt tip which is screwed onto a metallic base plate which is then affixed to the roof tile or surface. The lightning rod is connected to adjacent rods by installing a metallic tape through the base plate.

However, there are alternative forms of air terminals where the rod and tape are replaced by a cylindrical metallic conductor which can be cut and bend into the required length and shape according to the usage. They can be fixed to the horizontal or vertical surface of the building using simple brackets. Hence these alternative air terminals are more economical to manufacture, store and easier to install.

Figure 6. An example of a continuous solid cylindrical conductor applied as an air terminal on the ridge end of the roof.

Figure 7. Another example of a continuous solid cylindrical conductor applied as an air terminal on the ridge end of the roof.

Figure 8. An example of a continuous solid cylindrical conductor applied at the outer corner of the roof.

Figure 9. An example of a continuous solid cylindrical conductor suspended horizontally above the roof to better intercept the lightning bolt.

Figure 10. An example of a continuous solid cylindrical conductor suspended high above the roof on masts to protect vulnerable rooftop equipment.

V. NON-CONVENTIONAL AIR TERMINALS

These are air terminals that are claimed to have extra-ordinary large protection zones by their proponents (i.e. inventors, manufacturers, vendors, dubious academics). They claimed that these air terminals can either attract or repel the lightning bolts, but their claims have never been proven scientifically since their invention. As such, the proponents claimed that only one air terminal is generally sufficient to protect the whole high-rise building or a group of closely built smaller buildings and structures.

The use of these air terminals has already been rejected by the scientific community since the 1980s but generic versions of them have repeatedly been invented since then by opportunistic inventors. For example, the radioactive air terminals were initially invented in the early 1970s, but their claims have been scientifically disproved a few years later. However, the non-radioactive versions of the air terminals were re-invented by the same inventors and renamed the early streamer emission (ESE) air terminals in the late 1980s. Like the radioactive air terminals, the ESE air terminals were claimed to provide a protection radius of between 50 to 100 m. However, studies show that such claims were baseless and can endanger the buildings and people who use them. [10 - 26]

The ESE air terminals seemed to have become the dominant non-conventional air terminals sold in the world market. However, many high-rise buildings in lightning prone countries that use the ESE air terminals have been struck by lightning, some repeatedly, resulting in numerous bypasses.

In Malaysia, many high-rise buildings displayed multiple bypasses after being installed with one or more ESE air terminals. While most bypasses occurred at the perimeter of the roof within the claimed protection zone, more and more bypasses were seen to have occurred very close to the ESE air terminals themselves, some within ten meters.

A. *Close Proximity Bypasses*

The incidences of bypasses well within the claimed protection zone of the ESE air terminals have risen in tandem with the increase in the number of high-rise buildings using them.

Figure 12. A high-rise building photographed with a bypass about 25 m from an ESE air terminal.

Figure 13. Close-up photograph of the bypass and the ESE air terminal.

Figure 14. Photograph of the same building with a new bypass taken 5 years later. The old bypass has been repaired.

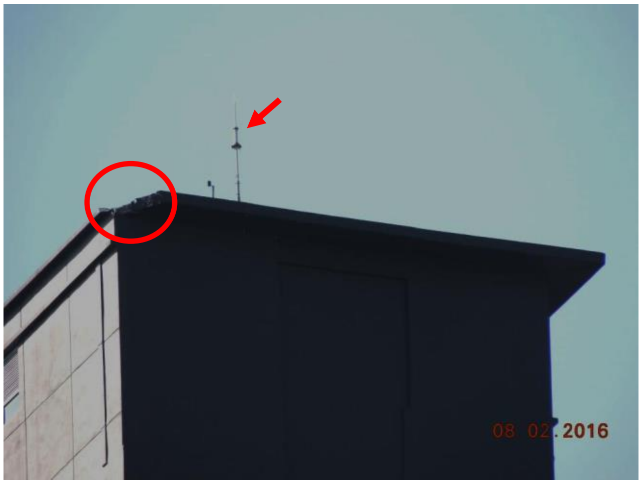

Figure 15. Close-up photograph of the new bypass which is located less than 10 m from the ESE air terminal.

Figure 16. Close-up photograph of an ESE air terminal surrounded by 3 nearby bypasses.

B. Bypasses to more than one ESE Air Terminals

Some buildings were installed with additional ESE air terminals after they have been struck by lightning repeatedly. However, these actions were a failure because the bypasses continued to occur even after the additional air terminals have been installed.

Figure 17. A building photographed with two ESE air terminals.

Figure 18. The same building photographed with a bypass about 5 years later.

In one case study that spanned several years, a high-rise apartment building was installed with an ESE air terminal was repeatedly struck by lightning. This continued even after the height of the air terminal was increased. After two additional ESE air terminals were added, more bypasses still occurred as the building continued to be struck by lightning [27].

C. Close Proximity Bypass in France

In 2009, the stone cross on a 25 m high bell tower in the town of Sigolsheim was damaged by a direct lightning strike [28]. The stone cross was situated on a ridge end of the roof and a mere 7 m from an ESE air terminal which was installed on the opposite end. This is clear evidence that the ESE air terminal cannot attract lightning better than a stone cross and that its claimed protection zone is false.

Figure 19. The bell tower showing the remnants of the damaged stone cross (left) and the ESE air terminal (right) about 7 m away. (Picture courtesy of Dernières Nouvelles d'Alsace)

VI. CONCLUSION

Climate change is expected to bring more violent thunderstorms to many parts of the world and with them more lightning flashes. Buildings and structures that have already been installed with conventional lightning protection systems that fully complied with the IEC 62305 standard are well protected from the deleterious effects of lightning. However, those that have been installed with non-compliant conventional systems or with the non-conventional systems are potentially at much higher risk of being struck and damaged by multiple lightning bolts. This is evidenced from the hundreds of ESE installed buildings that have been struck by lightning repeatedly in Malaysia.

To mitigate this impending problem, the relevant authorities should enforce the IEC 62305 standard on all existing and future buildings and structures. Non-compliant conventional lightning protection systems should be improved until they fully comply with the provisions of the standard while non-conventional systems should be completely replaced with conventional ones.

Engineers tasked with designing lightning air termination systems must ensure that they are fully competent to understand the physics of lightning as well as the provisions of the IEC 62305 standard to ensure the safety of the buildings and the people who use them. Universities that offer lightning protection courses must ensure that their lecturers are well qualified to do so and that their curriculum and research activities are not detrimental to public safety.

REFERENCES

[1] Hartono, Z. A., and Robiah, I., "A Method of Identifying the Lightning Strike Location on a Structure", International Conference on Electromagnetic Compatibility, Kuala Lumpur, April 1995.

[2] Hartono, Z. A., and Robiah, I., "The Collection Surface Concept as a Reliable Method for Predicting the Lightning Strike Location", 25th International Conference on Lightning Protection, Rhodes – Greece, September 2000

[3] Darveniza, M., "A Modification to the Rolling Sphere Method for Positioning Air Terminals for Lightning Protection of Buildings", 25th International Conference on Lightning Protection, Rhodes – Greece, September 2000

[4] Australian/New Zealand Standard, Lightning Protection, AS/NZS 1768, 2003, pg. 32.

[5] International Standard, IEC 62305-3, First edition 2006-1, Protection against lightning - Part 3: Physical damage to structures and life hazard, pg. 31

[6] Dudas, J. and Dudas, M., "Software for Lightning Protection System Diagnosis according to IEC 62305", 29th International Conference on Lightning Protection, Uppsala, Sweden, June 2008.

[7] Kern, A., et al "Probability of Lightning Strikes to Air Terminations of Structures using the Electro-Geometrical Model Theory and the Statistics of Lightning Current Parameters", 30th International Conference on Lightning Protection, Cagliary, Italy, June 2010.

[8] Hartono, Z. A., and Robiah, I., "Misconceptions about Lightning and its relation to Air Terminal Design Errors", CIGRE C4 Colloquium on Lightning and Power Systems, Kuala Lumpur, Malaysia, May 2010.

[9] Ahmad, H. "*Kilat dan Perlindungan* (Lightning and Protection)", Universiti Teknologi Malaysia Press, 1998.

[10] Darveniza, M., Mackerras, D., and Liew, A. C., "Review of Claimed Enhanced Lightning Protection of Buildings by Early Streamer Emission Air Terminals", IEE Proceedings – Science Measurement Technology, Vol. 44, No. 1, January 1997.

[11] Bryan, J. L., Biermann, R. G., and Erickson, G. A., "Report of the Third Party Independent Evaluation Panel on the Early Streamer Emission Lightning Protection Technology", NFPA Standards Council, September 1999.

[12]. Hartono, Z. A., and Robiah, I., "A Study of Non-Conventional Air Terminals and Stricken Points in a High Thunderstorm Region", 25th International Conference on Lightning Protection, Rhodes – Greece, September 2000.

[13] Hartono, Z. A., Robiah, I. and Darveniza, M., "A Database of Lightning Damage caused by Bypasses of Air terminals on Buildings in Kuala Lumpur, Malaysia", 6th International Symposium on Lightning Protection (VI SIPDA), Santos, Brazil, November 2001.

[14] Mousa, A. M., "Validity of the Collection Volume Method/Field Intensification Method for the Placement of Lightning Rods on Buildings", 26th International Conference on Lightning Protection, Krakow – Poland, September 2002.

[15] Uman, M. A. and Rakov, V. A., "A Critical Review of Non-conventional Approaches to Lightning Protection", Bulletin of the American Meteorological Society, December 2002.

[16] Rison, W. "Experimental Validation of Conventional and Non-Conventional Lightning Protection Systems", International Conference on Atmospheric Electricity, Toulouse, France, July 2003.

[17] Rakov, V. A. and Uman, M. A. "Lightning: Physics and Effects", Cambridge University Press, August 2003, pp. 609.

[18] Hartono, Z. A., and Robiah, I., "A Review of Studies on Early Streamer Emission and Charge Transfer System conducted in Malaysia", 17th International Zurich Symposium on Electromagnetic Compatibility (EMC Zurich), Singapore, February 2006.

[19] Hartono, Z. A., and Robiah, I., "Conventional and Un-conventional Lightning Air Terminals: An Update", Journal of the Association of Consulting Engineers Malaysia, June 2007.

[20] Hartono, Z. A., and Robiah, I., "Performance of Non-standard Lightning Air Terminals: Re-visited", 29th International Conference on Lightning Protection (ICLP), Uppsala, Sweden, June 2008.

[21] Cooray, V. "Non-conventional Lightning Protection Systems", 30th International Conference on Lightning Protection (ICLP), Cagliari, Italy, September 2010.

[22] Cooray, V., edited by, "Lightning Protection", The Institution of Engineering and Technology, 2010, pp. 239.

[23] Cooray, V. on behalf of CIGRE WGC4.405 Lightning Interception "Non Conventional Lightning Protection Systems", WG C4.405 Report, Electra No. 258, October 2011.

[24] Hartono, Z. A., and Robiah, I., "Close Proximity Bypasses to Collection Volume and Early Streamer Emission Air Terminals", Asia Pacific International Conference on Lightning, Chengdu, PR of China, November 2011.

[25] Hartono, Z. A., and Robiah, I., "Lightning Protection for the Holy Mosque and the Jamarat Bridge in Makkah", 32nd International Conference on Lightning Protection (ICLP), Shanghai, PR of China, October 2014

[26] Hartono, Z. A., and Robiah, I., "The ESE and CVM Air Terminals: A 25 Year Photographic Record of Chronic Failures", Asia Pacific International Conference on Lightning, Krabi, Thailand, May 2017.

[27] Hartono, Z. A., "Clear Evidence of Lightning Strikes to a Building Installed with Multiple ESE Air Terminals", ICLP-SIPDA, Sri Lanka, September 2021.

[28] Sigolsheim: Le clocher endommagé par la foudre (The Bell Tower Damaged by Lightning), Les Dernières Nouvelles d'Alsace, May 2009.

Circuit Model of Multiconductor Lines Excited by an Incident Plane Wave

Moustafa Raya, Sergey V. Tkachenko and Ralf Vick
Chair for Electromagnetic Compatibility
Otto von Guericke University Magdeburg
Magdeburg, Germany
moustafa.raya@ovgu.de

Abstract—This work presents a circuit model for multiconductor lines excited by an incident plane wave suitable for SPICE simulations. Multiconductor lines are divided into segments and represented as LC components and controlled sources appropriate for circuit solvers. The advantage of the presented model is that EMC engineers can calculate field coupling on conductors directly in circuit simulators without using field simulation programs. The developed model can be used directly in the frequency domain or in the time domain containing nonlinear elements without the need for an inverse Fourier transform.

Keywords- Circuit model; multiconductor lines; field coupling

I. INTRODUCTION

The analysis of field coupling on transmission lines (TLs) is considered one of the most important topics in the EMC world. However, there has always been an interest in developing circuit models of TLs for SPICE simulation. Full-wave simulations quickly reach their limits, especially when simulating large cable lengths. An ideal solution would be to simulate the field coupling on TLs directly in circuit solvers without requiring a higher computational effort. This problem is addressed in this paper by presenting a lumped circuit model for TLs that can be directly integrated into the SPICE environment. The model accounts for the field coupling of a plane wave without the need for field simulations.

II. CIRCUIT MODEL

Agrawal *et al.* presented the field coupling on n-conductor lines as follows [1]:

$$\frac{d\mathbf{V}^{s}(z)}{dz} + j\omega\mathbf{L}'.\mathbf{I}(z) = \mathbf{V}'_{\tan}(z) \quad (1)$$

$$\frac{d\mathbf{I}(z)}{dz} + j\omega\mathbf{C}'.\mathbf{V}^{s}(z) = 0. \quad (2)$$

The $n\times n$ matrices $\mathbf{L}'$ and $\mathbf{C}'$ are the inductance and the capacitance of the lines per unit length (p.u.l.). The $n\times 1$ vectors $\mathbf{I}(z)$ and $\mathbf{V}^{s}(z)$ are the total current and the scattered voltage. The p.u.l. voltage induced by the tangential electric field on the conductors is represented by the $n\times 1$ vector $\mathbf{V}'_{\tan}(z)$ and is given for the i-th conductor above a ground plane by $V'_{\tan,i}(z) = E_z^{in}(h_i, z) + E_z^{re}(h_i, z)$, where h_i is the height of the i-th conductor above the ground. An equivalent circuit can be interpreted from (1) and (2) as LC components with the voltage source $\mathbf{V}'_{\tan}(z)$ to represent the field coupling. A time domain solution for $V'_{\tan,i}(z)$ was found as follows:

$$V_{tan,i}^{k} = \Gamma_i . \frac{dE_0(t - T_{i,k})}{dt}, \quad (1)$$

where k is the order of the section at the i-th conductor. The element Γ_i is proportional to the angle of incidence of the wave θ and h_i. This solution can be easily interpreted as a circuit model in SPICE, where the time shift of $E_0(t)$ can be realized by a matched TL and the time derivation by calculating the current of a 1F capacitor for a defined voltage source. Three conductors of $2\,m$ length with a height $h_1 = 10\,mm$, $h_2 = 20\,mm$ and $h_3 = 40\,mm$ are shown in Fig. 1. The diameters are $d_1 = 1\,mm$, $d_2 = 0.5\,mm$, and $d_3 = 2\,mm$. The element D_1 is a diode of type MBR0520L. The loads are set to $R_{1-6} = 75\,\Omega$.

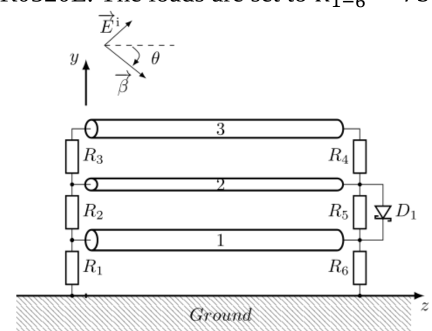

Figure 1. Three wires over a ground plane.

An incident plane wave was excited with an angle $\theta = 45°$ and an electric field strength of $100\,V/m$. It has a trapezoidal time function with rise, fall and hold times of $2\,ns$, $3\,ns$ and $10\,ns$, respectively. The induced voltage across D_1 is compared to CST simulations in Fig. 2.

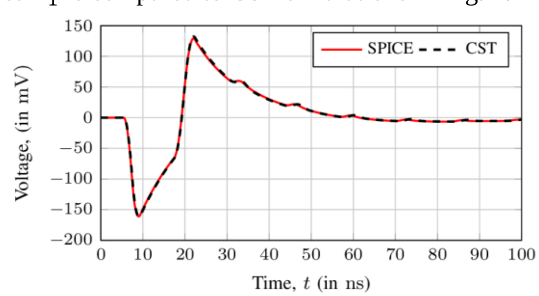

Figure 2. Voltage response across D_1.

REFERENCES

[1] A. Agrawal, H. Price, and S. Gurbaxani, “Transient response of multiconductor transmission lines excited by a nonuniform electromagnetic field,” in 1980 *Antennas and Propagation Society*, June 1980, pp. 432–435

Method of Modal Parameters for the Wire Segments with Symmetrical Geometry and the Regge Method

S.V. Tkachenko, F. Middelstaedt , M. Raya and R. Vick
Otto-von-Guericke University, Magdeburg, Germany
e-mail: sergey.tkachenko@ovgu.de

Abstract**—** By earlier developed Method of Modal Parameters (MoMP) we have shown that for the single and double wire segments with symmetrical geometry the response functions for lumped voltage excitation can be calculated with good accuracy using only diagonal elements of corresponding infinite modal matrices. This gives a possibility to apply the Regge method early used for the circular wire.

Keywords- thin wires; helix; common mode; differential mode; Regge theory

I. INTRODUCTION

Analytical methods for calculating the effect of EM fields on thin wires - the Method of Modal Parameters (MoMP) was developed earlier [1]. In this method the system of exact Mixed Potential Integral Equations (MPIE), describing induced current and potential along the line, can be reduced to matrix equations with modal parameters: infinite matrixes of inductance and capacitance. These parameter matrixes are calculated by Fourier transformation of the kernels of the first and the second of MPIE, correspondingly. The solution of this system with further inverse Fourier transformation yields induced current and potentials. For the finite system of wires with symmetrical geometry - circular wire and its symmetrical combinations all modal parameter matrix become diagonal and the solution is reduced to a single sum. This gives a possibility to consider an excitation of such systems [3] by a lumped voltage source using so named Regge method.

II. RESULTS

In this work, we consider single and double finite wires with symmetrical geometry: straight wire, circular wire and helix wire, which are important for EMC practice. For such geometries corresponding MPIE systems are reduced to the separate uncoupled MPIE for differential and common current modes. For each mode we have solved these equations by the MoMP. Due to the fact, that the kernels of the MPIE for such systems of wires depend on the difference of arguments, during the calculation of corresponding matrix elements one can carried out a single integration instead of double one in the general case of arbitrary wires, which essentially reduce time of calculation. Moreover, we have found that to describe the current induced by a lumped voltage source in these thin symmetrical wires, it is sufficient to take into account only the diagonal terms of the corresponding matrices of modal parameters, i.e., the solution is approximately reduced to a single summation, as in the case of a circular wire (see Fig. 2). This circumstance gives a possibility to apply Regge method [2] for the summation of the series. In this method, the summation index m is considered as a complex variable and the Fourier series is represented as an integral

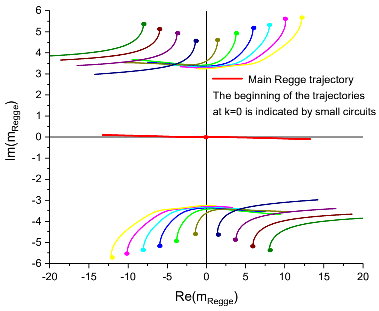

Figure 1. Regge trajectories $m_\alpha(k)$,for the differential current mode in straight wire pair, $0 \le k \le 4.1$, a=1mm,L=10m and d=1m.

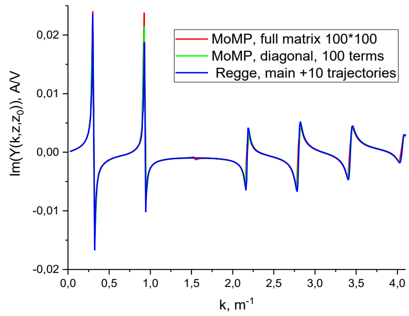

Figure 2. Comparison of the admittance functions obtained by the full matrix MoMP, the MoMP diagonal terms and by the Regge method. The source is at z_0=4m and receiver is at z=5 m

in the complex plane of the parameter m. The integral is defined by the zeros of the diagonal modal impedance per-unit length in the complex plane of the parameter m, which zeros define the so called Regge poles. The positions of the poles on the complex plane depend on the frequency and form so called Regge trajectories (see Fig.1). Our approach reduced summation over m, which require several hundred terms, to summation over Regges poles, which requires about ten terms (see Fig.2).

REFERENCES

[1] S.V. Tkachenko, F. Middelstaedt and R.Vick, "The Method of Modal Parameters for the Wire Segments With Symmetrical Geometry and Singularity Expansion Method," in *IEEE Letters on EMC Practice and Applications*, vol. 4, pp. 2-6, March 2022.
[2] T.Regge, " Introduction to complex orbital momenta", Il Nuovo Cimento, VOL. XIV, N. 5 Dec. 1959, pp. 951-976.
[3] S.V. Tkachenko, F. Middelstaedt and R.Vick, "The Regge Method for a Vertical Half-Circular Loop above Conducting Ground", GLOBALEM 2022

E1 HEMP Exposure of Ungrounded Shielded Cables

Edward B Savage
Metatech Corporation
Goleta, California, USA
savagee@cox.net

William A Radasky
Metatech Corporation
Goleta, California, USA
wradasky@aol.com

Abstract—It is a good idea to use shielded cables (or conduit) for wiring that could get exposed to E1 HEMP, such as power substation yard cables, with the shields grounded at both ends (preferable using 360° bonds to the metal enclosures [1]. However sometimes grounding occurs only at one end. Such open-ended shielded cables are discussed here, and a very simple model is presented. Experimental results will also be shown in the full presentation.

Keywords- shielded cables; shield grounding; E1 HEMP

I. BACKGROUND

Sometimes E1 HEMP is a concern but high frequency effects are not fully appreciated. For example, sometimes open-ended shields are used for substation yard cables, as represented in Fig. 1. One reason for this is to avoid ground potentials driving high currents along the length of the shield. However, we will show this is bad for E1 HEMP. This issue was demonstrated to us when we tested an assembled shielded serial cable and found essentially no shielding. Opening one connector, we saw it was not grounded – with a ground added the shielding improved greatly. In this paper we only consider a fast pulse (E1).

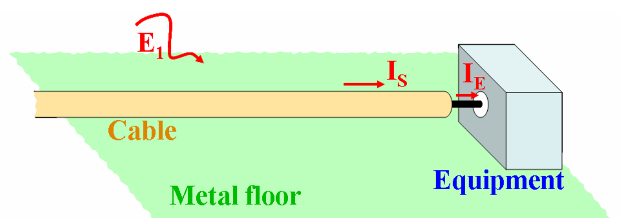

Figure 1. Example of E1 HEMP coupling to an ungrounded shielded cable.

II. MODEL DEVELOPMENT

Our concern is the current on the core wires entering the equipment (I_E in the figure). To start to model this, consider Fig. 2, where the drive is backwards – we drive a current on the unshielded part of the cable and look at the currents that get onto the shield and onto the core wire. Here we have three transmission lines, indicated by the three numbered currents - #2 is a coaxial line, the other two are lines-above-a-ground-plane.

An approximation to this is shown in Fig. 3, where all the transmission lines are made to be coaxial. Here we assume the shield is infinitely thin. In this case the E and B fields associated with the I_3 signal propagate unmodified into the two separate lines on the right. Thus the lines can be drawn as the two-wire transmission lines in Fig. 4, and the lines are governed by:

$$\begin{aligned} I_3 &= I_2 = I_1 \\ Z_3 &= Z_2 + Z_1 \\ V_3 &= V_2 + V_1 \end{aligned} \tag{1}$$

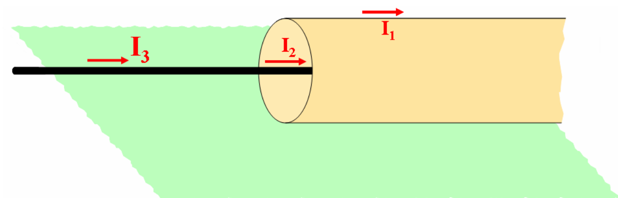

Figure 2. Current (I_3) being driven into an ungrounded shielded cable – resulting in currents I_1 and I_2.

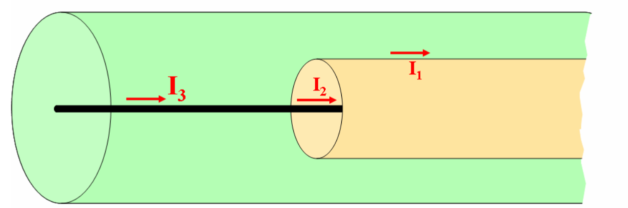

Figure 3. Simpler model of the setup in Fig. 2.

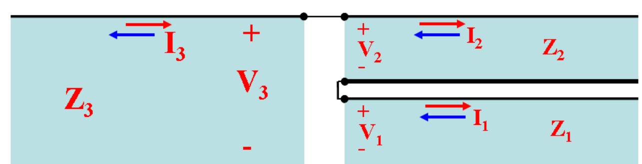

Figure 4. Two-wire transmission line equivalent of the coaxial transmission line setup of Fig. 3. (Ignore the blue arrows until they are discussed.)

III. OPEN-END MODEL

We can then model the case in Fig. 1 by driving I_1 instead, getting the currents shown by blue arrows in Fig. 4. Letting “x” show the separation of Z_3 into Z_1 and Z_2:

$$\begin{aligned} Z_1 &= x\, Z_3 \\ Z_2 &= (1-x)\, Z_3 \end{aligned} \tag{2}$$

we can solve the transmission line problem to get:

$$\begin{aligned} V_3 &= V_1 \\ I_3 &= x\, I_1 \end{aligned} \tag{3}$$

That is, the full voltage on the driven shield is transferred to the core wire, and the fraction “x” of the current transfers. Thus, if tens of dB shielding are desired, then an open-ended shielded cable will not provide it. Test results will also be presented.

REFERENCES

[1] MIL-STD-188-125-1, “Department of Defense Interface Standard, High-Altitude Electromagnetic Pulse (HEMP) Protection for Ground-Based C4I Facilities Performing Critical, Time-Urgent Missions, Part 1, Fixed Facilities”, 7 April 2005.

Time Domain Measurement of IEMI Shielding Effectiveness of Wire Meshes

Edward B Savage
Metatech Corporation
Goleta, California, USA
savagee@cox.net

William A Radasky
Metatech Corporation
Goleta, California, USA
wradasky@aol.com

Abstract—In this paper we report on time domain measurements of the shielding effectiveness of wire mesh, for fast pulses, as would be appropriate for IEMI (intentional electromagnetic interference).

Keywords- IEMI, wire mesh, shielding effectiveness.

I. INTRODUCTION

For an enclosure, such as a room, metal sheet provides excellent EM (electromagnetic) shielding effectiveness (SE). However, metal mesh might be used instead, such as for lower weight or ventilation, (such as is common for "screen" rooms). We are interested in the basic SE for the material, such as would be seen for a plane wave incident on an infinite sheet. A formula for this (for square mesh openings) is [1]:

$$SE = 103.5 - 20\log_{10}(d_{mm}\ f_{MHz})\quad (dB)\,. \qquad (1)$$

where d_{mm} is the mesh spacing and f_{MHz} is the frequency. (In the time domain this corresponds to a scaled time derivative. (This formula will have some lower and upper frequency limits, not given here.) Our measurements will check this formula.

II. MEASUREMENT APPROACH

For practical reasons (such as limiting sample size and emissions) typical the SE is measured in a setup such as shown in Fig. 1. A screen room is divided into two rooms, with a mesh sample covering a window in the room partition. One room transmits an EM signal, and the other room measures what leaks through the mesh. Usually this is done in the frequency domain. There are complications with this approach, however, such as reflections and diffraction. We can avoid these two issues by using the time domain. Reflections and diffraction have additional path lengths, and so time delays – we use the measured signal only up to the time where corruption from these delayed effects can arrive. With this approach, the partition wall is not needed – the leakage around the screen edge, delayed from extra path length, is also ignored.

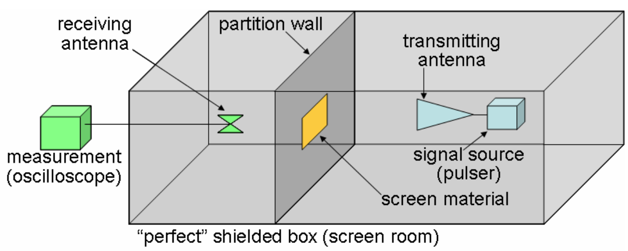

Figure 1. Example of a screen SE measurement setup.

III. SAMPLE RESULTS

Measurements were made samples of various mesh sizes – Fig. 2 shows the ½ inch mesh. Fig. 3 shows measured signals for the samples. The red line is without any mesh, and the black line is with a very fine copper mesh (100 wires per inch) – with very good SE. Diffraction effects cannot come in until the time marked "edge". Fig. 4 shows a fit of:

$$SE = 99.7 - 20\log_{10}(d_{mm}\ f_{MHz})\quad (dB)\,. \qquad (2)$$

compared to the measurements for the 1 inch mesh – good agreement, a constant 3.8 dB poorer SE than Eq. 1. The presentation will also show results for variations, such as rotated and tilted meshes, and use of two meshes.

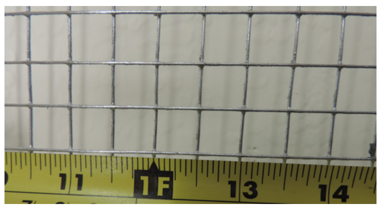

Figure 2. Sample of a wire mesh (with 1/2" spacing).

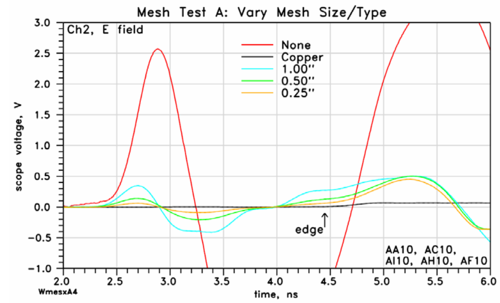

Figure 3. Measured waveforms for various mesh samples.

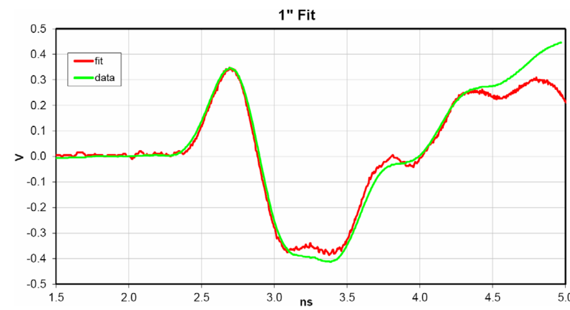

Figure 4. Sample waveform measurement and fit.

REFERENCES

[1] Donald R. J. White, *Shielding Design, Methodology and Procedures*, Don White Consultants, 1986, 1st ed., page 4.18.

Development of Standing Wave Oscillator-Fed Antenna Array for Compact HPEM Applications

Zahra Esmati, Isaac J Cann and J Scott Tyo
Electrical and Computer Systems Engineering Department
Monash University
Clayton VIC Australia
tyo@ieee.org

John E Fletcher
School of Electrical Engineering & Telecommunications
UNSW Sydney
Sydney NSW Australia

Abstract—We are developing the capability to produce compact HPEM source systems for the generation and radiation of mesoband pulses in the UHF and low microwave frequencies. Our system is based on a compact standing wave oscillator (SWO) microwave source that feeds a linear array of electrically small antennas (ESAs). We have studied the performance of the system as a function of switching parameters in the SWO and are working on the development of methods to design and implement dense arrays of ESAs for power sharing.

Keywords-HPEM Sources, antenna arrays

I. INTRODUCTION

Mesoband HPEM sources operate with moderate bandwidths, typically in frequencies from around 100 MHz to 10 GHz. These sources are generally composed of a capacitive energy storate, a weakly resonant pulse forming network (PFN), and a radiating system. Often more than one of these sub-components are integrated into a single structure. For example, our system uses a standing wave oscillator where a quarter-wave section of coxial transmission line is used as the energy store, and this element also serves as the PFN by operating as a quarter-wave transmission line oscillator that is shorted at one end in a spark gap and feeds a high impedance antenna at the other end. A schematic of our system is shown in Figure 1, and a representative system has been reported on previously [1].

II. Performance of SWO

The SWO operates by charging the center conductor of a low-impedance (~4 Ω) coaxial line to high voltage. The high voltage initiates a self-breakdown, and this breakdown induces a damped sinusoidal oscillation at the center frequency with period that corresponds to twice the round trip time of the coaxial section. Some energy couples out at each reflection from the load end, resulting in a damped sinusoidal waveform with bandwidth typically on the order of 3 – 15%, depending on the nature of the antenna and the loss in the switch [2].

Because the discharge is initiated by the random event of switch closure, the radiated waveform depends on several factors including the precise location of the spark, the exact charge voltage, the conductive-phase rise time of the spark, and the on-state resistance. Usually it is impossible to measure any of these directly. Here we use a computational model to show how varying these parameters affects the bandwidth, duration, and magnitude of the radiated field. We attempt to use this model to estimate the SWO parameters for real shots measured from an experimental system.

III. Antenna Array Design

We are currently working on strategies to improve our ability to control the coupling of energy from the corporate waveguide feed onto the individual elements of a coaxial array of ESAs. Our current work is focusing on the use of a Huygens-like probe that has both an electric and magnetic dipole moment, allowing the excitation of waves traveling in only one direction [3] and providing precise control of the coupling cross section.

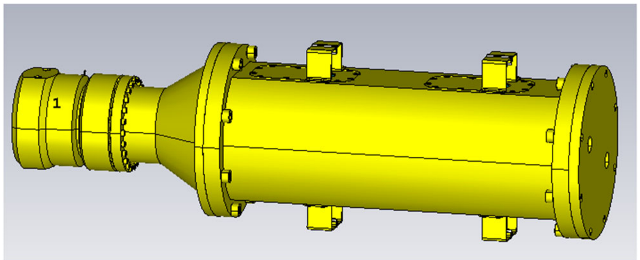

Figure 1. Solid model of an SWO-fed, 4-element coaxial array of ESAs from [1].

REFERENCES

[1] Z. Esmati, *et al*, "Development of an Equivalent Circuit Model for the Design of Arrays of Electrically Small Antennas," in *IEEE Trans. Antennas and Propagation*, doi: 10.1109/TAP.2022.3161326. (Article pre-print service)

[2] M. M. H. Armanious, *et al.,* "Interaction between geometric parameters and output waveforms in high-power quarter-wave oscillator," *IEEE Trans. Plasma Sci*., **38**, 1124 – 1131, 2010.

[3] D. Yi, *et al.,* "Regulating the Direction That Power Flows in Microwave Transmission Line Systems With Huygens Sources," *IEEE Trans. Antennas and Propagation*, **69** 594-599 (2021)

On the use of Doubly Conformal Electrodes in Vacuum Diodes for High Power Microwave Applications

E. Neira [(1)], F. Vega [(1)], C. Kasmi [(1)(2)],
[(1)] Directed Energy Research Centre, Technology Innovation Institute, Abu Dhabi, United Arab Emirates
[(2)] Faculty of Electrical Engineering, Helmut Schmidt University, 22043 Hamburg, Germany
ernesto.neira@tii.ae

Abstract— This paper evaluates the use of double conformal electrodes in Vacuum Diodes for High-Power Microwave applications. It was found that having both conformal cathode and anode, produces a more uniform electric field distribution, resulting in higher emitted current. This is illustrated by comparing the beam current emitted by a traditional planar geometry and the proposed double conformal geometry. The results were obtained by particle in cell simulation.

Keywords- Conformal Electrodes, High Power Microwaves sources, Field emission.

I. CONFORMAL VS PLANAR ELECTRODES

In a vacuum diode, parameters such as the emitted current, the electron diffusion and the beam current density distribution [1] have a large impact on the performance of quality of the beam. Moreover, those parameters are highly influenced by the electrostatic field, defined by the boundary conditions imposed by the surface of the electrodes.

It has been demonstrated that Conformal Electrodes produces uniform electric field distribution over the emitting surface [2]. This characteristic allows increasing the effective emitting cathode surface and the uniformity of the current distribution. Another advantage is the capacity to reduce the electron diffusion resulting in the improvement of the beam efficiency.

As example, Figure 1 compares the electric field of the diode presented in [3] with a proposed conformal diode designed to have an equivalent emitting area and gap. Magnitude of the electric field is shown using colormap, direction using arrows.

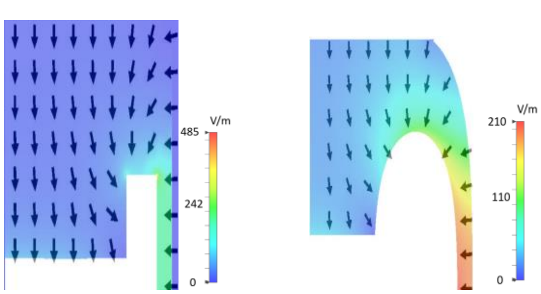

Figure 1. Electric field for planar [2] (left-hand) and conformal electrode (right-hand)

II. RESULTING BEAM

The planar diode reported in [3] produced a peak diode current of 21 kA, with a diffusion of 30 %, for an effective current of 14.7 kA. This geometry was simulated in CST-Particles in cell simulations with Explosive Electron Emission, obtaining a current of 22.5kA. The electron diffusion obtained from the simulation was 38% resulting on a beam current of 14 kA.

The same kind of simulation was performed on a conformal diode, obtaining a current equal to 26.3kA. The electron diffusion was 22 %, resulting on a higher beam current of 20.5 kA.

Simulations were performed for a double exponential signal of 290 kV peak. The diodes charge distribution is shown in Fig. 2. For the planar diode, charge concentrates in the border and center, being this the reason for the high electron diffusion. Whereas for the conformal, the charge presents high uniformity.

III. CONCLUSIONS

This example illustrates that diodes with double conformal electrodes improve the concentration of electrons in the beam when compared to planar profiles. This type of geometry is a promising idea that might be considered in HPM. In future works, electrodes will be experimentally compared in terms of effective emission area.

REFERENCES

[1] V. G. Baryshevsky et al., “Generation of High-Current Electron Beams in Diodes With Large-Area Explosive Emission Cathodes,” IEEE Trans. Plasma Sci., vol. 44, no. 7, pp. 1103–1111, Jul. 2016, doi: 10.1109/TPS.2016.2572043.
[2] R. Schinzinger, and P. A. A. Laura, “Conformal Mapping, Methods and applications”, Dover publications, Inc. New York, 2000
[3] E. H. Choi, M. C. Choi, Y. Jung, M. W. Choug, J. J. Ko, Y. Seo, G. Cho, H. S. Uhm, and H. Suk, “High-power microwave generation from an axially extracted virtual cathode oscillator,” IEEE Transactions on Plasma Science, vol. 28, no. 6, pp. 2128–2134, Dec 2000.

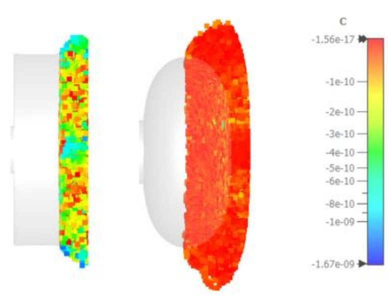

Figure 2. Charge distribution in the diodes. Left hand: planar diode. Right hand: conformal electrodes.

Magnetic Field Pattern Effects on Surface Impedance for Late-Time HEMP and Geomagnetic Disturbances

James Gilbert
Metatech Corporation
Goleta, California, United States of America
quantmec@charter.net

Abstract—In this presentation, we discuss the effect of the magnetic field pattern on the electric fields. Earlier calculations calculated the electric field from the local magnetic field using a one-dimensional multilayer conductivity calculation. Newer calculations use a multi-dimensional calculation including both horizontal and vertical variations of conductivity. To quantify the effect of two-dimensional variations in the magnetic field, we separate the magnetic field into irrotational and divergence-free portions and show that they have the opposite effect when the skin depth becomes longer than the characteristic length over which the magnetic field varies.

Keywords-Late time HEMP, Geomagnetic Disturbance, Surface Impedance,

I. INTRODUCTION

In this presentation we will examine an arbitrary surface magnetic field at the upper surface of a uniformly conducting half space and look at solutions for the electric field on the same surface in the frequency domain by expanding the surface fields into modes and examining the electric field for each mode. The separation into modes can be done in various coordinate systems for the ease of calculation. We first examined this for sinusoidal variations along a single direction and noted that the result at low frequencies greatly depended on whether the variation was in the direction parallel or perpendicular to the magnetic field. To generalize this, we took the general form for the magnetic field variation and noted that the separation into TE and TM modes explained the different behavior of the surface impedance as the frequency varied.

II. TECHNIQUE

The decomposition of an arbitrary surface magnetic field into TE and TM modes may be done using the Helmholtz decomposition for suitably behaved field – the only TEM mode is a spatially uniform magnetic field which is inconsistent with a localized field. With z in the vertical direction and $\nabla_{\perp}$ the two-dimensional gradient operator on the surface, the magnetic field of a TE mode has

$$\nabla_{\perp} \times H_{\perp} = 0 \quad \nabla_{\perp} \cdot H_{\perp} \neq 0 \qquad H_z \neq 0 \quad (1)$$

and a TM mode has

$$\nabla_{\perp} \times H_{\perp} \neq 0 \quad \nabla_{\perp} \cdot H_{\perp} = 0 \qquad H_z = 0 \qquad (2)$$

The surface impedances of the two types of modes are identical at high frequencies and equal to the result for a uniform magnetic field

$$Z_{TE},\ Z_{TM} \rightarrow \sqrt{\frac{-i\mu_0\omega}{\sigma}} \qquad (3)$$

but separate when the planar skin depth is equal to the characteristic horizontal length of variation and at low frequencies the surface impedance for TE modes behaves as

$$Z_{TE} \rightarrow \frac{-i\mu_0\omega}{|k_{\perp}|} \qquad (4)$$

which is inductive and the surface impedance for TM modes behaves as

$$Z_{TM} \rightarrow \frac{|k_{\perp}|}{\sigma} \qquad (5)$$

which is purely resistive In these formulae, σ is the conductivity, μ_0 is the permeability of free space, ω is the angular frequency and

$$k_{\perp} = \sqrt{k_x^2 + k_y^2} \qquad (6)$$

is the transverse wave number of the mode (in this example in Cartesian geometry).

III. RESULTS

The surface magnetic field of Surface Burst EMP is TM by symmetry. E3A (Blast Wave MHD) and Sudden Storm Commencement GMD vary in time so rapidly that the pattern effect is small. E3B (Heave MHD) and Electrojet GMD are predominantly TE and the electric field is reduced by the pattern effect. We will show numerical calculations of the effect in the presentation.

Delia Luca, Remus Stanca, Farhad Zazai, Lars Ole Fichte
Faculty of Electrical Engineering
Helmut Schmidt University
Hamburg, Germany
mailto: lo.fichte@hsu-hh.de

Abstract— The bio-heat equation is the equation that governs the power equilibrium inside biological tissue by summing the power influxes into a given area and balancing it with losses by various effects. A simplified equation is thus the basis for every calculation of the specific absorbtion rate, and the heating of tissue by external electromagnetic fields. Here, we present an approach to solve the bio-heat equation in a hybrid analytical/ numerical way.

Keywords-component; bio-heat equation, SAR value, thermal effects of electromagnetic fields

I. INTRODUCTION

The subject of our study is represented by the influence of electromagnetic fields on human bodies, focusing on tissue and cell levels. Generally speaking, the main questions we intend to answer are:

- “How the heat distribution would look if, inside a radiated human tissue with an electromagnetic field, there are present some magnetic nanoparticles?”,
- “What would be the most effective arrangement of those nanoparticles so that a specific volume of tissue would achieve a desired temperature?”,
- “What should be the best frequency and amplitude of the electromagnetic wave that radiates the tissue so that it would reach a particular temperature?” and
- “How long would it take for a volume of tissue to get heated up to a specific temperature?”.

Answering these questions would be a good and solid starting point for the field of medical treatments based on electromagnetic stimulation of specific parts of the body previously “filled” with magnetic nanoparticles. It is a known fact that the proteins’ chain brakes when a cell reaches 42°C, so having a more accurate idea of how the heat distributes inside the tissue depending on the magnetite disposal would be helpful in order to better control the exact ill part of the tissue that should be destroyed. It also reaches interest to study the effects of magnetic nanoparticles presence even at a deeper level, respectively at cell layer, and to determine the ratio between the cell volume and the magnetite volume for an efficient and expected result in terms of area/ number of cells which get to such a temperature that negatively affect them.

II. APPLICATION TO KNOWN SCENARIOS

Our work has involved exemplary cases for heat equation, namely a comparison between the analytical and numerical solution for different scenarios, having the goal to prove that the results are the same.

A scenario that might simulate the post-effects of a tissue block, filled with magnetite, radiated by an electromagnetic field can be modeled in the software Comsol based on heat transfer module. The magnetic nanoparticles can be considered heat point sources with a temperature of 42°C, and the tissue can be designed as a 3D irregular geometric body with a normal initial temperature of 37°C. The boundary conditions would also be set to 37°C as no condition form the exterior environment should be considered in this point.

A more complex study case involves both bioheat transfer and electromagnetic waves modules from Comsol, without considering the magnetic nanoparticles heat sources from the beginning. The electromagnetic radiation generates the heat source and, depending on the geometry, dielectric and magnetic properties assigned for each domain (tissue, magnetite), the heat distribution is obtained. Moving forward to the cell layer, the geometry should be more detailed, adding more domains (nucleus, cytoplasm, membrane, magnetite).

III. CONCLUSION

Concluding, the influence of an electromagnetic field on a biological organism is a full potential subject which has to be accurately studied in order to get the answers for the proposed questions that we have mentioned in the introduction. This would lead to a bigger image of what might be done in the medical treatments' field that have the goal of destroying the ill cells and protect the healthy ones.

Use of C-UAS System and Its EM Effect Analysis

Tae Heon Jang
RF Application Technology Center
Korea Testing Laboratory (KTL)
Ansan-si, Gyeonggi-do, Korea
thjang@ktl.re.kr

Jeong Ju Bang
Aerospace EM Technology Center
Korea Testing Laboratory (KTL)
Jinju-si, Gyeongsangnam-do, Korea
jjbang@ktl.re.kr

Jeong Min Kim
Aerospace EM Technology Center
Korea Testing Laboratory (KTL)
Jinju-si, Gyeongsangnam-do, Korea
jmkim@ktl.re.kr

Abstract—Counter UAS(C-UAS) system is protection system for infrastructure against UAS threats. Most of C-UAS systems use radar and RF jammer for detection and neutralization of UAS respectively. C-UAS system is installing in critical facilities such like airport, nuclear power plant and energy infrastructures in many countries for security against UAS threats. However these EM sources may affect to the existing critical system, subsystem or equipment around them. It needs to assess EM vulnerability before installation of them for safety in the aspect of EMC. This paper investigates how to assess EM vulnerability according to IEC standards and others and proposes the necessity of a new standard to deal with it.

Keywords- C-UAS, EM, Vulnerability, Assessment

I. INTRODUCTION

UAS is considered a threat when its operation has, or indicates, the potential to harm life, information, operations, environment and/or property. Counter UAS system refers to a set of technological tools to monitor, detect, identify, record and enable response to unauthorized UAS activities; C-UAS may also include countermeasures capable to neutralize, or limit, potential risks. Different types of deployment can be considered: C-UAS system placed in fixed positions, mounted on vehicles or drones, or portable. Most of C-UAS systems use radar and RF jammer for detection and neutralization of UAS. C-UAS system is installing in critical facilities such like airport and nuclear power plant for security against UAS threats. However these EM or HPEM source may affect to the existing critical system, subsystem or equipment around them. It needs to assess EM vulnerability before installation of them for safety in the aspect of EMC. This paper investigated IEC standards and other standards on the assessment of EM vulnerability in civil critical infrastructures due to EM or HPEM sources.

II. USE of COUNTER UAS SYSTEM

Figure 1 shows examples of C-UAS introduced at infrastructures. Some of C-UAS use radars for detecting UAS and RF jammer for neutralizing UAS. In future, C-UAS system may introduce HPEM sources to counter the threat of UAS swams. The use of C-UAS system render that HPEM compatibility is getting more important in the existing system.

(a) C-UAS for nuclear power plant

(b) C-UAS for airport

Figure 1. Examples of C-UAS system used at infrastructures.

III. EM EFFECT ANALYSIS AND ASSESSMENT

IEC/TS 61000-5-9 discusses methods for the assessment of systems to the effects of HPEM.

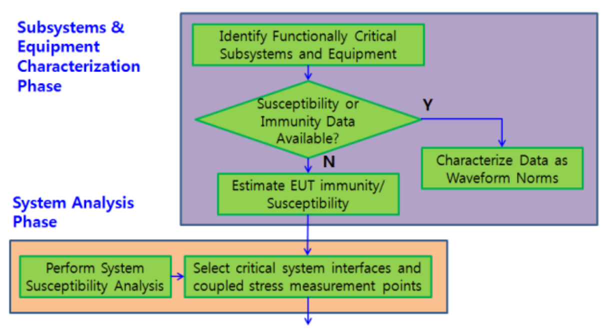

Figure 2. Assessment methodology flow chart in IEC 61000-5-9

From ITU-T K.81, Vulnerability level (VL) of a system for infrastructure can be derived from equation (1).

III. CONCLUSION

The near use of HPEM sources will drive IEC TC77 SC C to establish the method of analysis and assessment for HPEM vulnerability, hazard and risk.

REFERENCES

[1] IEC/TS 61000-5-9, System-level susceptibility assessments for HEMP and HPEM, August 2009
[2] ITU-T K.81, High-power electromagnetic immunity guide for telecommunication systems, June 2016

Study of Post Breakdown Arc Resistance in Argon and Nitrogen Gas-filled Spark Gap Switch

Antaryami Mohanta, J. J. Pantoja, A. R. Baba, M. Alkaabi, A. Alebri, F. Vega, G. Matras, S. Al Marzooqi, A. Alteneiji, A. Dubey, S. AlMazrouei, R. Al Ameri, and C. Kasmi
Directed Energy Research Center,
Technology Innovation Institute (TII),
Abu Dhabi, UAE
Antaryami.Mohanta@tii.ae

Abstract— The amplitude, rise time, and shot-to-shot stability of the pulses produced by spark gap switches are dependent on the transient impedance of the plasma channel formed between the electrodes. Thus, optimization in the design of a gas-filled spark gap switch requires a detailed investigation of the time-dependent arc resistance. In this paper, we'll investigate the post break down characteristics in argon, and nitrogen gas-filled spark gap switches at different pressures and applied voltages. Special attention will be given to the Joule heating of the plasma channel formed between the electrodes, as this leads to a reduction in the arc resistance. Optical emission spectroscopy technique is proposed to characterize the plasma and to monitor its constituents at different conditions.

Keywords-Arc resistance; Gas-filled spark gap switch; Optical emission spectroscopy; Plasma channel; Streamer

I. INTRODUCTION

Gas-filled spark gap switches, which are based on gas breakdown and streamer formation between the electrodes, have been the main component of various pulsed power systems and machines such as linear transformer drivers (LTDs), Marx generators for Z-pinches, apparatuses for the generation of ultrawideband electromagnetic impulses, and generators of high-voltage impulses for biomedical and environmental applications [1]. The influence of different parameters on the operational performances of various gas-filled spark gap switches having different topologies has been considered [2]. Time-dependent arc resistance is an important parameter that significantly influences the amplitude, rise time, and shot-to-shot stability of the switched pulse. In this study, argon and nitrogen gases are used in the gas-filled spark gap switches, and post breakdown arc resistance was evaluated at different pressures and applied voltages. Optical emission spectroscopy (OES) is proposed to be used to characterize the plasma and to monitor the constituents of plasma.

II. EXPERIMENTAL SETUP

We'll use the experimental setup similar to reported in [1]. The spark gap electrodes are detailed in Fig. 1. The arc resistance will be determined from the current/voltage waveforms. The electrodes will be assembled in a gas cell which comprises several transparent windows that facilitate conducting plasma diagnostics. The characteristics of the plasma at different pressures and gas types can be studied using optical emission spectroscopy.

Figure 1. Spark gap electrodes designed to be used in a further laser triggering experiment. (a) the electrodes with axial holes through which the laser will be coupled to the interelectrode channel. (b) electrodes without the hole. Both cases will be analyzed.

Electric field distributions for electrode profiles of Fig. 1 are obtained by simulation using COMSOL Multiphysics software at different gap distances and applied voltages. For electrodes without an axial hole, the electric field is maximum at the center of the spark gap. However, for electrodes with the axial hole, the electric field distribution shows a dip at the center of the gap at gap distances below 3 mm. Such differences in the electric field distribution within the gap could have a significant impact on the arc resistance, which is evaluated from the experimentally measured current/voltage waveforms. The arc resistance is associated with the electrical conductivity of the plasma and therefore with the Joule heating. The evolution of plasma emission characteristics obtained by optical emission spectroscopy can be correlated to the arc resistance at different conditions.

REFERENCES

[1] Y. Yao, I. V. Timoshkin, S. J. MacGregor, M. P. Wilson, M. J. Given, and T. Wang, "Postbreakdown transient characteristics of a gas-filled plasma closing switch," IEEE Trans. Plasma Sci., Vol. 49, pp. 942–951 (2021).

[2] G. Schaefer, M. Kristiansen, and A. H. Guenther, "Gas discharge closing switches," Springer Science+Business Media New York 1990.

A Time-Reversal Cavity for Electromagnetic Waves in Transmission Line Networks with Arbitrary Topology

Zhaoyang Wang
Imperial College London (ICL)
London, United Kingdom

Hamidreza Karami
Elias Le Boudec
Farhad Rachidi
École Polytechnique Fédérale de Lausanne (EPFL)
Lausanne, Switzerland

Marcos Rubinstein
University of Applied Sciences of Western Switzerland (HES-SO)
Yverdon-les-Bains, Switzerland

***Abstract*—This paper describes the realization of a time-reversal cavity for electromagnetic waves in transmission line networks. A frequency-domain analysis of the two-stage wave processes that pertain to the time-reversal cavity is presented for a multi-terminal and multi-node transmission line network characterized by arbitrary topology.**

***Index Terms*—Electromagnetic waves; time reversal; time-reversal cavity; transmission lines**

I. Introduction

Recently, it was demonstrated in [1] that a matched transmission line network composed of coaxial cables can be considered as an exact one-dimensional (1-D) time-reversal cavity [2]–[5]. Specifically, by back-injecting, at each line terminal, the time-reversed voltage or current measured as a response to an initial source excitation, a time-reversed copy of the voltage or current distribution in the forward-propagation stage can be reproduced [1].

In [1], the time-reversal cavity was explored in the time domain marking reference to a network of three transmission lines connected to a single node. Also, it is indicated in [1] that the realization of the time-reversal cavity remains established despite the increasing topological complexity of transmission line networks. In this regard, the present paper is focused on generalizing the concept and properties of the time-reversal cavity to a multi-terminal and multi-node transmission line network characterized by arbitrary topology.

II. Frequency-Domain Analysis of a Time-Reversal Cavity in Transmission Line Networks with Arbitrary Topology

Consider the scenario of an inhomogeneous transmission-line network excited by a lumped series voltage source. The voltages and currents acquired in the forward- and backward-propagation stages are formulated analytically first using the frequency domain solutions. Furthermore, the converging and diverging components of the backward-propagating voltage are identified, and the time-reversed relation between the forward-propagating voltage and the converging component of the backward-propagating wave is inferred through a frequency spectral analysis. Then, the so-called interfering effect of the diverging component is comparatively investigated with respect to its counterpart in the time domain (e.g., [1]). Finally, the study discusses the implementation and effectiveness of an active time-reversal sink in the frequency domain to compensate for the effect of the diverging component.

References

[1] Z. Wang, F. Rachidi, M. Paolone, M. Rubinstein, and R. Razzaghi, "A Closed Time-Reversal Cavity for Electromagnetic Waves in Transmission Line Networks," *IEEE Trans. Antennas Propag.*, vol. 69, no. 3, pp. 1621–1630, Mar. 2021.
[2] D. Cassereau and M. Fink, "Time-Reversal of Ultrasonic Fields - Part III: Theory of the Closed Time-Reversal Cavity," *IEEE Trans. Ultrason. Ferroelectr. Freq. Control*, vol. 39, no. 5, pp. 579–592, Sep. 1992.
[3] D. Cassereau and M. Fink, "Theoretical Modelisation of Time-Reversal Cavities, Application to Self-Focussing in Inhomogeneous Media," *Acoust. Imaging*, vol. 19, pp. 141–147, 1992.
[4] R. Carminati, R. Pierrat, J. de Rosny, and M. Fink, "Theory of the Time Reversal Cavity for Electromagnetic Fields," *Opt. Lett.*, vol. 32, no. 21, p. 3107, 2007.
[5] J. De Rosny and M. Fink, "Overcoming the Diffraction Limit in Wave Physics Using a Time-Reversal Mirror and a Novel Acoustic Sink," *Phys. Rev. Lett.*, vol. 89, no. 12, pp. 124301-1–124301-4, Sep. 2002.

High Power CW Laser-induced Thermal Effects on an Electronic Device

L. Al Shehhi, A. Mohanta, S. Al Marzooqi, A. Alteneiji, S. Almazrouei, S. Al Hosani, A. Dubey, A. Al Blooshi, G. Matras, and C. Kasmi
Directed Energy Research Center,
Technology Innovation Institute,
Abu Dhabi, United Arab Emirates
Layla.Alshehhi@tii.ae

Abstract—Unmanned aerial vehicles (UAVs) have been considered for different military and civilian applications due to their wide range of functionalities. The most important component of an UAV is the flight computer and the associated electronics. High-energy laser systems used for counter-drone technology can induce faults in the electronic circuits, which depend on many parameters including the circuit technology and the laser characteristics. High-power laser-induced thermal effects can be vulnerable to different electronic components and therefore the performance of the electronic devices. In this study, thermal effects on the performance of a Raspberry pi are investigated.

Keywords-Raspberry pi; Laser-induced thermal effects; Data acquisition; Counter-drone technology; UAV

I. INTRODUCTION

Unmanned aerial vehicles (UAVs) are widely used for military and civilian applications including real-time monitoring, providing wireless coverage, remote sensing, search and rescue, delivery of goods, security and surveillance, precision agriculture, and civil infrastructure inspection [1]. To counter the performance of the UAVs, several counter-drone technologies such as radio frequency jammers, global positioning system (GPS) spoofers, high power microwave (HPM) devices, nets and guns, high-energy lasers, etc. have been developed. An UAV is a complex system composed of several sub-modules, such as the UAV airframe, the flight computer, the payload, the mission/payload controller, the base station, and the communication infrastructure [2]. The heart of the UAV is the flight computer and associated electronics, which are vulnerable to the directed energy systems. Directed energy systems composed of high-energy lasers can destroy UAVs by heating, melting, burning, and/or evaporation. Electronic components can also be damaged/neutralized due to overheating without experiencing even melting. In this paper, a Raspberry Pi is considered as an equipment under test (EUT), which is irradiated by a high-power continuous wave (CW) laser, and its performances such as central processing unit (CPU) temperature, random-access memory (RAM) usage, CPU clock frequency, and CPU load are actively monitored. The CPU temperature was primarily considered to observe the thermal effects induced in EUT. Components of the EUT is globally heated by the laser beam and the EUT performances are evaluated.

II. EXPERIMENT

A CW infrared fiber laser coupled to a short-range telescope as shown in Fig. 1(a) was used. The EUT along with its cover as shown in Fig. 1(b) was placed in an experimental chamber. The front surface of the EUT cover was exposed to the laser beam operating at 10% of its maximum power (6 kW). The beam diameter was kept sufficiently large to irradiate a wide area of the EUT and to avoid melting of the EUT cover. An external SSD storage device was used to save the data.

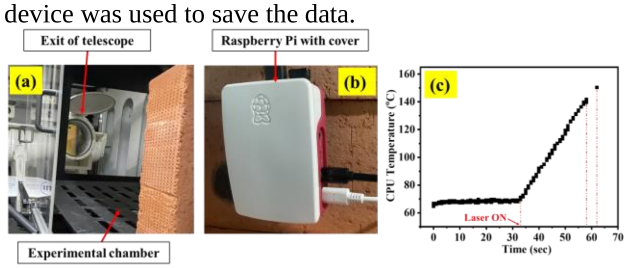

Fig. 1 (a)-(b) Experimental apparatus. (c) CPU temperature with time before and after laser irradiation.

III. DISCUSSION

The CPU temperature, RAM usage, CPU clock frequency, and CPU load were actively monitored at different times before and after the laser irradiation. The CPU temperature is found to increase after the start of the laser irradiation as shown in Fig. 1 (c). At higher CPU temperatures, the data acquisition rate was found to be decreased. At about 141^{o} C, EUT stopped saving the data and was shut down at about 150^{o} C. Further investigation will be made by irradiating the laser beam locally on individual electronic components of the EUT to identify its most vulnerable element. This study can be extended to other electronic devices and will be helpful to design an appropriate protective case for electronic devices that can prevent laser-induced thermal effects. Furthermore, this will also provide information about the required laser power level to induce desired thermal effects to neutralize the electronics of UAVs involved in malicious activities.

REFERENCES

[1] H. Shakhatreh, A. H. Sawalmeh, A. Al-Fuqaha, Z. Dou, E. Almaita, I. Khalil, N. S. Othman, A. Khreishah, and M. Guizani, “Unmanned aerial vehicles: A survey on civil applications and key research challenges” IEEE Access, vol. 7, pp. 48572 – 48634 (2019).
[2] E. Pastor, J. Lopez, and P. Royo, “A hardware/software architecture for UAV payload and mission control hardware/software architecture” IEEE Aerospace and Electronic Systems Magazine, vol. 22, pp. 3–8 (2007).

Measurement and Signal Processing of Radiated Fields of HPEM Sources

Edrees Almansoori(1), John Pantoja(1), Luciano Prado(1), Alexandra Gurinovich(2), and Felix Vega(1)
(1) Technology Innovation Institute, Abu Dhabi, UAE, e-mail: edrees.almansoori@tii.ae
(2) Belarus State University, Minsk, Belarus; e-mail: gur@inp.bsu.by

Abstract— In this abstract, we present the results of measuring electric field strength of HPEM systems. Measuring chain components will be discussed. Signal processing algorithms and the ed electromagnetic fields produced by HPEM sources are shown. Two designs based on derivative and replicative sensors are presented with examples.

Keywords: high power electromagnetics, HPEM, d-dot, sensors.

I. INTRODUCTION

With the dynamic development of high-power electromagnetic (HPEM) sources and interest in intentional electromagnetic interference (IEMI) in the last decades, specialized measurement systems able to characterize pulsed radiated signals in the order of nanoseconds, and electric fields of hundreds of kilovolts/meter are required. Commercial solutions are currently available with specialized instruments and sensors; however, different factors in the experimental setup can affect the validity of measurements. Signal detection, synchronization, attenuation, and transmission to the recording device should be done with minimal and controlled distortion. In addition, characterization and correction factors of each element in the measuring chain must be applied [1].

Measurements systems and sensors for HPEM and IEMI should be able to measure different types of IEMI threats, including electromagnetic pulses (EMP), ultrawideband pulses (UWB), and high-power microwaves (HPM). Each type of source also presents different operation modes, including single pulse, burst, or repetitive pulses. Therefore, for proper characterization, expert interpretation and processing of the retrieved waveforms must be done to determine the actual parameters according to the nature of the signal [2].

In this presentation, we discuss in detail the measurement and signal processing of the radiated electric field of HPEM sources using two different measurement chains based on a derivative sensor (D-dot) [3] and a replicative sensor (horn antenna). The impact and limitations of the measurement components are analyzed. Also, the inherent variability of HPEM sources is observed in the experimental results, indicating that statistical analysis is required in the characterization of these kinds of signals. For illustration, Fig. 1 presents two of the signals under study, radiated by a pulsed magnetron and switched-oscillator systems [4].

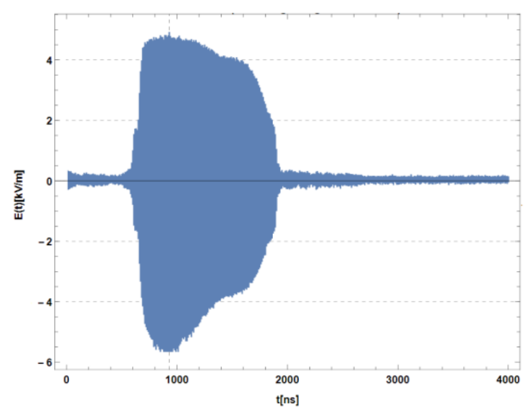

(a)

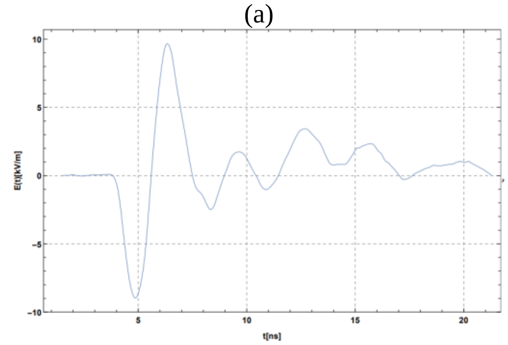

(b)

Figure 1 Reconstructed E-field radiated by: (a) pulsed-magnetron system; (b) a switched-oscillator system.

REFERENCES

[1] W. Reed, “EMP Sensor Application Guide”, electronic file available at https://www.prodyntech.com/wp-content/uploads/2013/10/EMP-SENSOR-APP-GUIDE-ANNOT.pdf.

[2] J. Jakubowski, M. Kuchta, R. Kubacki, “D-Dot Sensor Response Improvement in the Evaluation of High-Power Microwave Pulses”, *Electronics*, 10, 123, 2021, electronic file available at https://doi.org/10.3390/electronics10020123

[3] C. Baum, E. Breen, J. Giles, J. O’Neil, G. Sower, “Sensors for Electromagnetic Pulse Measurements Both Inside and Away from Nuclear Source Regions,” *Sensor and’ Simulation Notes*, Note 239, 1978.

[4] F. Vega, N. Mora, F. Rachidi, N. Peña and F. Roman, "Design of a switched oscillator for IEMI susceptibility testing," 2013 *IEEE International Symposium on Electromagnetic Compatibility*, 2013, pp. 423-427, doi: 10.1109/ISEMC.2013.6670450

Design of a Unmaned Aereal Vehicle for Synthetic Apertures Radar Applications

Jarrah Alhammadi(1), John Pantojaa(1), Felix Vega(1), Chaouki Kasmi(1), Jamal Zeddoug(2), John Mempin(2), Igor Campos(2), and Anouar Dhouibi(2).
(1) Directed Energy Research Center, Technology Innovation Institute, Abu Dhabi, United Arab Emirates
(2) Autonomous Robotics Research Center, Technology Innovation Institute, Abu Dhabi, United Arab Emirates
Jarrah.alhammadi@tii.ae

Abstract— This paper describes the design and final integration of an Unmanned Aerial Vehicle to be used as a platform for a Synthetic Aperture Radar. There are many advantages to using UAVs for synthetic apertures radar surveys, including cost reduction and flexible data acquisition through linear, helical, and elliptical. Compared with satellites or airplanes, this reduces operation complexity and flying time. The paper presents the general requirements of the platform and some examples of the images acquired with the final design.

Keywords- drone, synthetic apertures radar, UAVs

I. INTRODUCTION

Nowadays, drones play a significant role in many fields of industry, having an excellent financial return because of their flexibility and multipurpose uses. This paper shows the design process of a new UAV specifically adapted to the SAR (Synthetic Aperture Radar) system RD350 from Radaz (https://www.radaz.com.br). The SAR has three- band operations P, L, C (horizontal and vertical) and can produce polarimetric and interferometry SAR images from linear, helical, and elliptical flights at low flight altitudes of 120 m [1].

Fig. 1 shows a block diagram describing the UAV and its integration with the SAR system.

The general requirements of the platform are: 20 minutes of flight autonomy, 5 kg minimum payload, 15 W power supply for SAR power consumption, and wireless data transfer from flight segment to ground station.

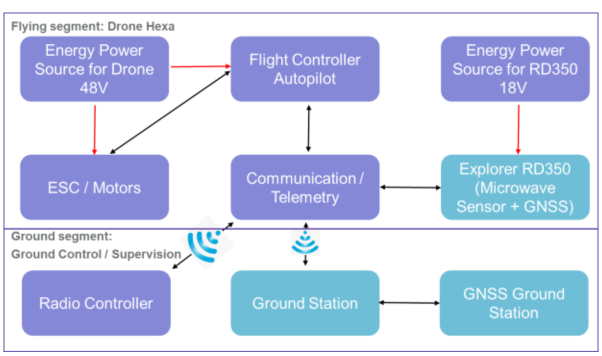

Figure 1. Block diagram of the drone-borne SAR system.

II. TEST

The system, shown in Fig. 2, was tested in realistic conditions in a rural area around the city of Abu Dhabi, UAE. A multiband system detects various objects and details within the area of interest without comprising the resolution. The three frequency bands of the system were used to clearly identify the crops, trees, and structures. The P and L-band pictures also revealed hidden objects at a depth of 1 m.

Figure 2. Microwave sensor Cabinet of Explorer RD350.

Figure 2. Drone-borne SAR during survey in a rual area in Abu Dhabi, UAE

REFERENCES

[1]L. Moreira et al., "A Drone-borne Multiband DInSAR: Results and Applications," 2019 IEEE Radar Conference (RadarConf), 2019, pp. 1-6, doi: 10.1109/RADAR.2019.8835653.

Multi-kW Class CW Laser-induced Damage Assessment of Metals and Carbon Fiber in a Mobile Research Laboratory

Ali Al Blooshi, Amit Dubey, Layla Al Shehhi, Guillaume Matras, Antaryami Mohanta,
Shaikha Al Marzooqi, Aaesha Alteneiji, Bader Al Ali, Chaouki Kasmi
Directed Energy Research Center
Technology Innovation Institute
Abu Dhabi, United Arab Emirates
Ali.AlBlooshi@tii.ae

***Abstract*—**

A multi-kW class laser mobile research laboratory (LMRL) capable of facilitating indoor and outdoor research activities is used to assess high-power continuous wave (CW) laser-induced damage to metals and carbon fiber. A short-range telescope system coupled with the laser was used to focus the beam onto the samples and the experiment was conducted in an indoor environment. The drilling process was monitored by high-speed imaging, which provides information about the interaction time required to damage the target. The laser power, beam diameter, laser exposure time, etc. were varied and the target damage assessment was carried out.

Keywords: Multi-kW class CW laser, Fiber laser, Metals, Carbon fiber, Laser exposure time.

I. INTRODUCTION

Direct energy system for counter-drone technologies have been paid increasing attention to damage/ neutralize the unmanned aerial vehicles (UAVs) involved in potentially harmful activities. Several industrial-grade laser systems have been developed for materials processing, which can be used as directed energy systems for countermeasure in a mobile platform [1]. The availability of high-power commercial fiber lasers opens an opportunity to develop a multi-kW class laser-based demonstrator in a mobile platform due to flexible beam delivery, low maintenance cost, high efficiency, and compact size [2]. A mobile platform can also facilitate research activities both in an indoor and outdoor environment.

In this work, we have used a multi-kW class laser mobile research laboratory (LMRL) to perform high-power laser damage assessments experiment in the indoor environment. Aluminum, steel, and carbon fibers are exposed to the high-power laser at a fixed distance, and the drilling process is monitored by a high-speed camera. The high-speed images are analyzed, and the damage/drilling time is obtained at different laser powers, beam diameters, and laser exposure times.

II. MULTI-KW CLASS LASER MOBILE RESEARCH LABORATORY (LMRL)

A. Components of LMRL

The key components of the LMRL shown in Fig.1 are a 6 kW CW fiber laser source (λ = 1080 nm), telescopes with a range covering from 3 to 2000 m, laser range finder, short and long-range video systems, and high-speed cameras equipped with a 20-foot standard container with the desert compatible environment.

Fig. 1. Photo of LMRL (telescope and container).

B. Experiment Set-up

The effect of laser irradiation on the static targets (aluminum, ABS plastic, and carbon fibers) kept at fixed distance was investigated. The laser powers used were varied from 1 to 6 kW, beam diameters were varied from 10 to 50 mm, and material thickness was 2 mm for aluminum, 1.5 mm for ABS and 3 mm for carbon fiber.

From the experiment results, it is feasible to study the vulnerability effects on different materials. The dependence of beam diameter and power radiation on the time needed to penetrate different materials can be assessed.

REFERENCES

[1] Stefan Ruppik, Frank Becker, Frank-peter Grundmann, Wolfram Rath, Ulrich Hefter, "High-power disk and fiber lasers: a performance comparison", *SPIE Digital Library,* volume: 8235, pages: 149-163, Feb 9, 2012. Accessed: Jun. 6, 2022. DOI:10.1117/12.913286.

[2] E. A. ShcherbakovV. V. FominA. A. Abramov "Industrial Grade 100 kW Power CW Fiber Laser," DOI: 10.1364/ASSL.2013.ATh4A.2.

Simulation supporting certification

IEMI and NEMP applications

Joly J.-C., Adam J.-P., Ribière-Tharaud N.
CEA, DAM, GRAMAT
F-46500 Gramat, France
Jean-christophe.joly@cea.fr

Abstract - To protect against Intentional Electromagnetic Interferences and Nuclear ElectroMagnetic Pulse, many armament programs rely on numerical simulations to estimate the electromagnetic constraints on the targets.
These numerical simulations can be performed at different stages of a project:

- in the conception phase,
- to optimize architectures and EM protections in terms of cost or performance,
- for retrofitting,
- or even in the test or acceptance phase.

In any case, the confidence in the numerical simulation is a critical point. Can we even reach a sufficient level of quality to consider that numerical simulation enables a credible certification approach? In that way, standards already exist for general industrial applications. Here, this paper presents a methodology associated with a checklist for the most specific IEMI and NEMP applications. Many practical examples will illustrate this approach.
(key words) Numerical simulation, certification, IEMI, NEMP, standard

I. METHODOLOGY AND BASIC PRINCIPLES

At the request of the DGA (Procurement Agency of French Armed Forces), CEA-Gramat proposed an approach to ensure the quality of the numerical simulation process, with the objective of moving towards certification.
This so-called “simulation for certification” approach answers the question: “What are the quality guarantees of a numerical simulation result? What are the criteria, the procedures, the verifications, that the Forces are likely to request in order to get the assurance that the numerical simulation is used appropriately, is robust and reliable?
The diagram below illustrates the proposition with a 3 stages pyramid of quality levels.

Criteria lower down in the hierarchy must be satisfied before simulation quality can attend to criteria higher up
In that way, the most complete requirement corresponds successively to respect of levels 1, 2 and 3.

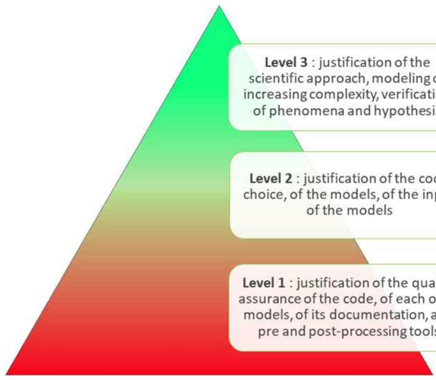

Figure 1. 3 stages pyramid of quality level

II. EXAMPES

Based on the diagram in Fig 1, examples will be given for each stage of quality criteria.
Level 1: example of the code quality assurance

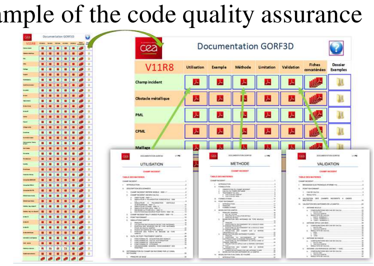

Level 2: example of a code choice justification: DFDT for NEMP, MoM for a narrow band IEMI ; thin slot model for faradization defects …

Level 3: example of minimal number of sensors for EM zone characterization, and best coupling incidence analysis with an inverse method, genetic algorithms for optimization…

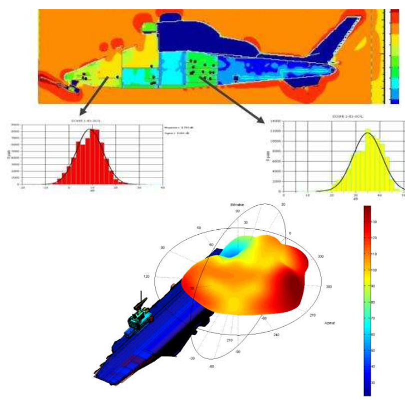

Acknowledgements : this research was supported by DGA - procurement agency of French Ministry of Armed Forces

Design of X-band Absorbers for Simultaneous Attenuation of Impinging Waves at Grazing Angles

V. Mishra(1), D. Brizi(1), V. Violi(1,2), M. AlMansoori(3,4),
A. Banelli(3), F. Vega(3), and A. Monorchio(1)

(1)Dipartimento di Ingegneria dell'Informazione, Università di Pisa - Pisa, Italy
(2) Dipartimento di Ingegneria dell'Informazione, delle Infrastrutture e dell'Energia Sostenibile, Università degli Studi Mediterranea di Reggio Calabria, 89124 Reggio Calabria, Italy
(3)Directed Energy Research Centre, Technology Innovation Institute, Abu Dhabi, United Arab Emirates
(4)Faculty of Electrical Engineering, Helmut Schmidt University, 22043 Hamburg, Germany
varsha.mishra@ing.unipi.it

Abstract—In this paper, classical resistive FSS absorbers are studied against the capability to simultaneously reduce the coupling level related to grazing angles impinging waves, travelling on their surface. The operative frequency band spans from 6 to 14 GHz (i.e., X-band). In order to evaluate the attenuation along the waves propagation direction, parallel to the absorber plane, the transmission coefficient (S21) of the transverse EM wave is evaluated by using the waveguide method through accurate full wave simulations. The transverse attenuation level can be used as a further metric, beside absorption, to adopt the most suited solution for coupling reduction in a given application.

Microwave absorbers, frequency-selective surfaces, electromagnetic interferences, coupling reduction, waveguide.

I. INTRODUCTION

The demand of microwave absorbers (MAs) is increasing as the fabrication of electromagnetic (EM) based devices, such as microwave integrated circuits (MICs), is raising as well. In these cases, analysis of surface wave attenuation in the transverse wave is also important for the interference problem [1].

In this work, we evaluate the behavior of two different resistive FSS absorbers against impinging waves at grazing angles. This capability can be combined, together with absorption, to develop the most suited solution to reduce electromagnetic coupling in a given application.

II. PRELIMINARY RESULTS

The transmission coefficient (S_{21}) of the transverse EM wave is analyzed in the first dominant mode of a parallel plate waveguide. The simulation of the waveguide is carried out in a full-wave environment with the dimension of (Width × Height × Length) 70mm × 17.5mm × 206mm. The boundary conditions are applied by giving PMC and PEC at the sidewalls and the top-bottom walls of the waveguide, respectively.

In Fig. 1(a), we reported the absorption level of the two resistive FSS absorbers; as evident, they present a similar absorbing behavior in the X-band. Beside, Fig. 1(b) shows also the attenuation retrieved with the waveguide method for grazing angles impinging waves. As evident, the patch FSS shape behaves better than the simple cross in this sense; therefore it presents more advantages, since it can combine absorption and attenuation for impinging waves at grazing angles.

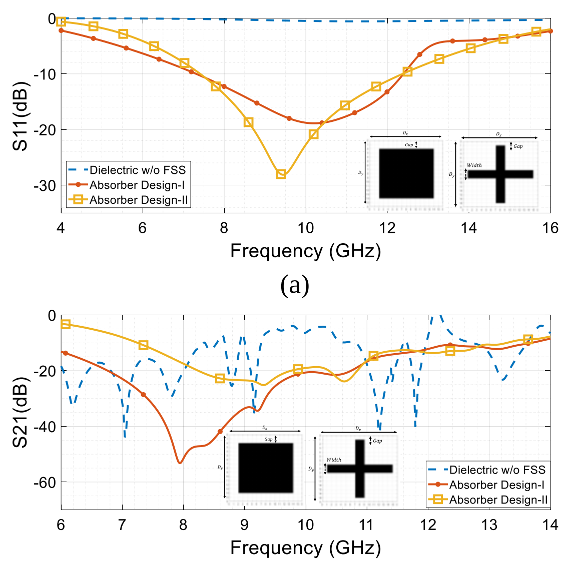

(a)

(b)

Figure 1. Reflection coefficient of Lossy dielectric without FSS, Absorber Design-I and II (a). Attenuation level for grazing angles incidence obtained through waveguide full-wave simulation, design I and II (b).

REFERENCES

[1] V. Mishra, F. Costa and A. Monorchio, "Surface Wave Attenuation in Multilayer Structures With Lossy Media and Impedance Surfaces," in IEEE Access, vol. 9, pp. 130627-130637, 2021.

Performance Evaluation of Ultra-Wideband Vivaldi Antennas for GPR Systems

A. Rangel [(1)], C. Pedraza [(1)], F. Ruiz [(1)], A. Fracica [(1)], S. Montana [(1)], J. Pantoja[(2)], A. Banelli[(2)], E. Almansoori[(2)] F. Vega [(2)], C. Kasmi

(1) Dept. of Electrical and Electronic Engineering, Universidad Nacional de Colombia, Bogota, Colombia

(2) Directed Energy Research Center, Technology Innovation Institute, Abu Dhabi, United Arab Emirates

jarangelr@unal.edu.co, edruiza@unal.edu.co, capedrazab@unal.edu.co, ffracica@unal.edu.co, tmontana@unal.edu.co, felix.vega@tii.ae

***Abstract*—**. This paper focuses on the evaluating the performance of different Ultra-Wideband Vivaldi antennas for GPR systems, in the context of detection of landmines and IEDs. The antennas will be first characterized in anechoic environment, and furthermore will be installed in a 2D scanning GPR. Different survey mechanisms will be tested, including down looking GPR and forward-looking GPR. The tests will be performed over real soil containing surrogate targets and clutter.

Keywords: improvised explosive devices, Ground Penetrating Radar, Ultra-Wideband Antenna, Vivaldi Antenna

I. INTRODUCTION

Ground Penetrating Radar (GPR) systems have become an efficient solution for landmine detection, as they are able to detect both metallic and non-metallic buried targets such as improvised explosive devices (IEDs). In the last decades, different techniques have been proposed to improve the performance of GPR systems to detect IEDs [1, 2].

Depending on the antenna position, GPR systems can be classified according to the angle of illumination with respect to the soil in Forward-looking GPR systems (FLGPR) [3] and Down-looking GPR systems (DLGPR). In the first one, the transmitting antenna illuminates the soil under a given angle of incidence, trying to minimize the reflection coming back from the air-soil interface. FLGPR systems require a high dynamic range at the receiver to achieve enough sensitivity to detect the buried targets. In the Down-looking GPR systems, the incident wave hits normally the ground interface [3]. In this case, the clutter effect is greater due to the reflection of the electromagnetic waves in the ground.

In the use of GPR for assessment, the way the measurements are taken is another important parameter that the user has control over. The method used for data acquisition can be modified to affect specific outcomes. For example, enhance the result image or to measure properties such as speed of propagation in the host medium.

GPR survey methods can be classified as the common offset (CO), common source (CS), and the common receiver (CR) surveys [3]. The CO survey is the most commonly used, where a fixed distance is maintained between the transmitting and receiving antennas. The CS and CR improved the signal-to-noise ratio and achieved a greater depth of penetration.

This contribution is focused on the analysis of different types of UWB Vivaldi antennas implemented in a 2D portable platform–based GPR, including commercial and custom-designed Vivaldi antennas.

In addition to characterizing the antennas, the purpose is to assess the effect of the angle of illumination (DL-GPR, FL-GPR) together with the variations of the types of surveys on the impact of the detection capabilities of the GPR system.

The tests will be performed over two types of real soil: high-humidity content soil and dry sandy soil. In both cases, surrogate targets and clutter will be included.

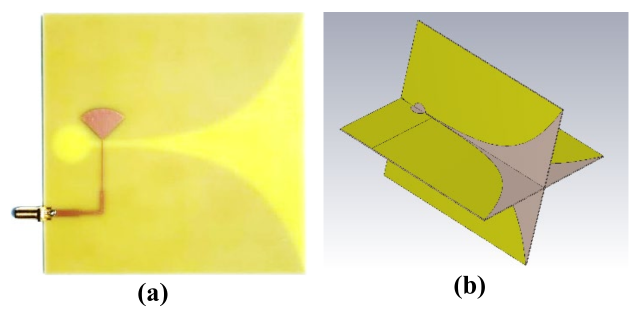

Figure 1 Example of a Vivaldi antennas evaluated. (a) Realized single-polarization Vivaldi operating between 0.8 and 3.5 GHz, notice the feeding transmission line. (b) 3D model of dual polarization Vivaldi antenna operating between 0.65 to 4.1GHz.

REFERENCES

[1] S. Gutierrez, "Application of Time-Frequency Transformations in Polarimetric Ultra- Wideband MIMO-GPR signals for Detection of Colombian Improvised Explosive Devices," 2020.

[2] D. J. Daniels, ''A review of GPR for landmine detection,'' Sens. Imag., Int.J., vol. 7, no. 3, pp. 90–123, Sep. 2006.

[3] A. H. Trang and H. G. Irion, ''Simulation of close-in and stand-off mine detection,'' in Proc. IEEE Int. Geosci. Remote Sens. Symp, pp. 1132–1134, Dec. 1997.

On the Modeling of the Initial Stage of the Electric Explosion Process of a Wire Array

Ali Alhammadi[1,2], Evgeny Gurnevich[1], John J. Pantoja[2], Asilah Almesmari[2], Felix Vega [2], and Chaouki Kasmi[2]
(1) Belarus State University, Minsk, Belarus
(2) Technology Innovation Institute, Abu Dhabi, United Arab Emirates
ali.alhammadi@tii.ae

Abstract—The paper presents a model for the exploding wire array process in Copper. It uses a circuit model that couples the basic LRC circuit equations with zero-dimensional thermodynamic calculations that track the effect of heating on the heat capacity and resistance of the wire.

Keywords-Exploding wire, electric explosion, copper, resistivity, heat capacity

I. INTRODUCTION

Exploding Wire Array (EWA) are fast switches used in pulse power applications [1]. A typical testing circuit to characterize EWAs is shown in Fig. 1.

The proposed RLC circuit equations couple the thermodynamic calculations that track the effect of heating on the heat capacity and resistance of the wire [2]. The model considers EWA's physical parameters, such as the length, cross-section, and the number of wires, to shape the output pulse current amplitude and waveform. The breakdown of electric strength must be able to match the generated voltage for the full EWA circuit.

The study focuses on Exploding Wire Arrays manufactured in copper, following the Zero-dimension method used in [1].

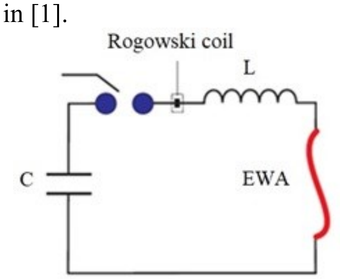

Figure 1. Exploding-wire array testing circuit

II. THEORETICAL METHOD

The model determines the current as a function of the time in an exploding cooper wire array, when the energy stored in a capacitor bank (C) is discharged into the wire array through a series inductance, as shown in Fig. 1.

This can be calculated using:

$$\frac{dI}{dt} = -\frac{R}{L}I - \frac{I}{LC}q$$

where: I, R, q are current, resistance, charge in the circuit of Fig. 1, and L, C are inductance and capacitor. The effect of heating on the heat capacity of copper is calculated based on the data provided in [2]. The current as a function of the time to be calculated.

$$\Delta H(t) = \frac{1}{m}\int_0^t R_{wire}(t)I(t)^2 dt$$

where ΔH is the heat generated per unit mass of the wire, m is the mass, and t is the time. For illustration, Fig. 2 shows the current calculated for an EWA with 28 wires, 0.1 mm diameter, C= 6.60 μF, charging voltage 60 kV, and L= 3.90 μH. The figure shows the calculated current assuming time dependent parameters (with parameters) and parameter independent of the time (without parameters) up to the liquid phase. A similar process was developed to study the response of Aluminum and Tungsten wires.

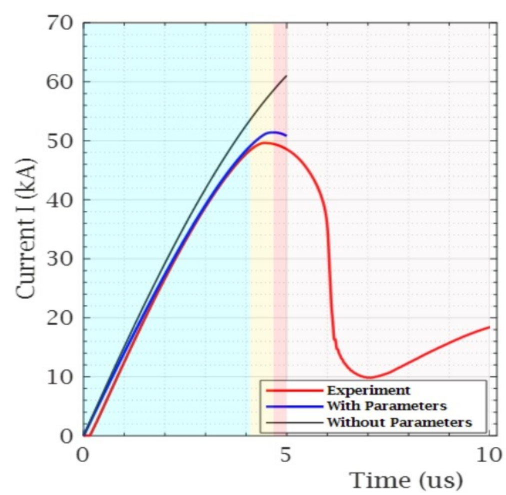

Figure 2. Comparison of experimental and calculated results. In light blue is highlighted the solid phase, in yellow is the melting phase, and in light red is the liquid phase.

REFERENCES

[1] A. Alhammadi, E. Gurnevich, C. Kasmi, F. Vega, and J. Pantoja "Resistivity of copper at the initial stage of an electric explosion process." 3rd URSI Atlantic / Asia-Pacific Radio Science Meeting, Gran Canaria, Spain, May 29 – June 3, 2022.
[2] Berning P. R., Coppinger M. J. CCDC Army Research Laboratory Aberdeen Proving Ground United States. An Exploding-Wire Circuit Model. 2020
[3] Mesyats G. A. Pulsed power / G. A. Mesyats, New York: Kluwer Academic/Plenum Publishers, 2005. 568 c.

GMD Impacts on High Voltage Power Grids – Lessons Learned

William A. Radasky
Metatech Corporation
Goleta, California, USA
wradasky@aol.com

James L. Gilbert
Metatech Corporation
Goleta, California, USA
quantmec@charter.net

Abstract—Over the past 33 years a great deal has been learned about how geomagnetic disturbances (GMDs) affect high voltage power grids. Many researchers have analyzed the nature of the many large and small geomagnetic storms that have occurred since the infamous Quebec power grid failure in March 1989, and have evaluated through both analysis and data reviews how power grids have been affected. This paper will review some of the major accomplishments over the past 33 years in our understanding. Of course the problem is not completely solved, as we do not know what the Sun will do in the future, nor have we been successful in applying protection techniques on a large scale to vulnerable power grids.

Keywords- Geomagnetic storms, GMDs, high-voltage power grids

I. BACKGROUND

This paper reviews (over the past 33 years) the study of geomagnetic storms and their impacts on high-voltage transmission grids. Discussion of some early papers and references will be part of the presentation. Much of the interest in geomagnetic storms was motivated due to the voltage collapse of the transmission grid in Quebec, Canada, due to the sudden onset of a significant geomagnetic storm on March 13, 1989. Since measurements of the magnetic field that initiated the grid collapse were available near the power grid itself and the power grid operators had timed data regarding the operation of the grid itself, it is clear that the voltage collapse occurred over a period of only 92 seconds [1].

II. TOPICS TO BE DISCUSSED

1. Evaluation of the need for faster magnetometer measurements
2. The need for time-domain modeling techniques
3. Graphical display of measured and calculated fields and induced currents
4. Evaluation of deep earth conductivity profiles
5. Modeling of large grids and end-to-end validation
6. Relationship of induced currents and the voltage level of power grids
7. Impacts due to different types of geomagnetic storms
8. Vector behavior of the "incident" magnetic fields
9. Edge of the grid, the ocean effect and line length considerations

II. EXAMPLE RESULTS

Two examples of important developments are illustrated below. Each of the topics and their importance will be discussed during the presentation. Figure 1 illustrates ground contours of the measured magnetic fields with the available 1-minute data. Note the rapid changes with time.

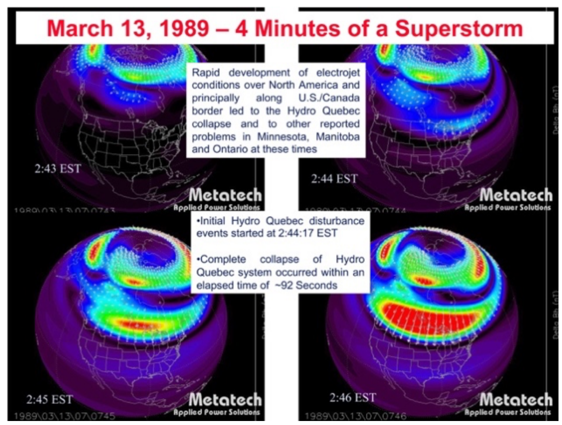

Figure 1. Graphical frames of the March 13, 1989 Quebec electrojet storm (magnitude of measured B-fields is shown) [2].

Figure 2 illustrates the variation of the direction of the measured horizontal B-field with time during a large GMD event in Scandinavia in 1991.

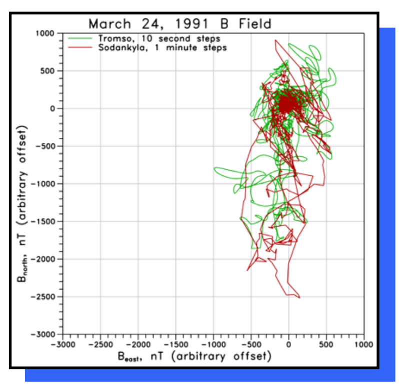

Figure 2. Measurements of the B-field vector with time [1].

REFERENCES

[1] "Understanding of geomagnetic storm environment for high voltage power grids," CIGRE Technical Brochure 780, October 2019.

[2] J. Kappenman, "Geomagnetic Storms and Their Impacts on the U.S. Power Grid,", Oak Ridge National Laboratories, Meta-R319, January 2010.

GLOBALEM 2022-The JOLT System: A Retrospective

Jane Lehr and Edl Schamiloglu
Department of Electrical & Computer Engineering
University of New Mexico
Albuquerque New Mexico USA
jmlehr@unm.edu

Abstract— Early in the last century, a realized, ultrawideband radiating system was described to the world in a Special Issue of the Proceedings of the IEEE dedicated to the applications of compact pulsed power technology. The Guest Editor of that Special Issue was Edl Schamiloglu, our Summa Foundation President, and Jane Lehr was the Technical Director for the pulsed power system and co-author of the article [**1,2**]. Dr. David Giri was instrumental in the development of that groundbreaking system – known as JOLT - and a co-inventor of the critical system component known as the impulse radiating antenna (IRA). The foundational research, development of the system, and anecdotes will be discussed.

Keywords- Impulse radiating antenna, radiating systems, ultrawideband

I. INTRODUCTION (HEADING 1)

In his memoir, *My Journey with Carl*, Dave Giri wrote, "***Hyperband Systems*:** Carl wrote a concept paper on radiating impulse-like waveforms (100's of ps wide) in 1989. He helped me to implement the concept that resulted, in 1994, of a highly successful prototype IRA. This work was sponsored under SBIR Phase I and II contract awards from the Air Force Research Laboratory, Kirtland AFB, NM. Since completing that pioneering work, many UWB systems that I and others have built are finding applications in military and civilian sectors." In our judgement, this synopsis is insufficient to describe the rich history and the continuing legacy of impulse radiating antennas and the JOLT system.

Transient high power electromagnetic systems generally consist of a pulsed, high peak power source and an antenna capable of radiating a substantial fraction of its spectral content. The category known as ultrawideband (UWB) or more recently "hyperband" sources provides a radiated electromagnetic environment with a fairly flat spectral content over one to two decades – generally from tens of megahertz to several gigahertz. Such systems have found both military and civilian applications [3], but we contend the impact of JOLT is most significant on the approach to integrated design now called *systems thinking.*

For example, the IRA I – also known as the Prototype IRA – was differentially fed from the source by a center-tapped pulse transformer [4,5]. The IRA I, developed and fielded in 1994, used a high-pressure hydrogen switch, a focusing lens, and a four-arm TEM horn to produce an extremely powerful hyperband pulse from a 3.66-m (12 foot) reflector. With a charge of only 60 kV, this system generated a transient signal with a peak electric field of 4.6 kV/m at a 200 Hz repetition rate. The IRA I system was retrofitted with a 2 m reflector and designated the IRA II [6,7]. The source was modified to provide a peak voltage 75 kV and pulse repetition rate of 400 Hz. The radiated spectrum of the 2 m IRA was measured to be flat in the frequency range 200 MHz to 3 GHz with a band ratio of 10. IRA antennas are known as balanced sources.

JOLT was conceived as a deployable system so that the footprint was confined by the size of the truck bed. After a very short consideration, it was concluded that an unbalanced source was needed for packaging as well as the difficulty in making a balun at the required design voltage. Noting the symmetry, the half-IRA [8] over a symmetry plane was conceived so that the high-voltage signal could feed the antenna directly with a coaxial source line. This system architecture makes the high-voltage design more tractable but lacks the uniformly symmetric field pattern of a full parabolic antenna [9]. JOLT is powered by a very compact and highly efficient 1.6-MV resonant transformer that is connected, via an integrated transfer capacitor and an oil peaking switch, into an 85- half-IRA. This unique system delivered a tightly focused radiated field with a FWHM on the order of 100 ps and a field-range product of approximately 5.3 MV at 200 Hz [10,11].

REFERENCES

[1] E. Schamiloglu, Special Issue of the Proceedings of IEEE on Pulsed Power and its Applications, vol. 92, 2004.

[2] D.V. Giri, *My Journey with Carl*, p. 6.

[3] D.V. Giri and F.M. Tesche, I*EEE Trans. Electromagn. Compat.*, vol. 46, pp. 323–329, Aug. 2004.

[4] C.E. Baum, "in Proc. URSI General Assembly, Maastricht, The Netherlands, 2002.

[5] J. Bohl et al., in Proc. AMEREM, June 2002.

[6] D. Giri, et al., IEEE Trans.Plas.Sci, vol. 25, 1997.

[7] W.D. Prather, "The 6 IRA," in Proc. Nat. Radio Science Meeting, Boulder, CO, Jan. 2001.

[8] L.H. Bowen, et al, "A prototype high-voltage UWB transmitter," SSN 473, Summa Foundation, Mar. 2003.

[9] C.E. Baum, SSN 378, 1995.

[10] C.E. Baum et al., SSN 480, 2003.

[11] W.D. Prather, et al, IEEE Trans EMC, Vol. 46, 2004.

On the Influence of Luminous-and-Grounded Channel on the Radiated Electric Fields at Close Distance in Rocket-Triggered Lightning

Quanxin Li[1,2], Jinliang He[1], Jianguo Wang[2], Marcos Rubinstein[3], and Farhad Rachidi[4]
1 State Key Laboratory of Power System, Department of Electrical Engineering, Tsinghua University, Beijing 100084, China
2 School of Electrical Engineering and Automation, Wuhan University, Wuhan 430072, China
3 University of Applied Sciences of Western Switzerland (HES-SO), 1400 Yverdon-les-Bains, Switzerland
4 Electromagnetic Compatibility Laboratory, Swiss Federal Institute of Technology (EPFL), 1015 Lausanne, Switzerland

Abstract— An analysis on the influence of the luminous-and-grounded channel on the radiated electric fields at close distance range in rocket-triggered lightning is presented. The presence of the luminous-and-grounded channel is found to play an important role in the fine structure of the electric fields associated with M-components.

Keywords**:** initial height; return-stroke; M-component model of charge transfer; electric fields

I. INTRODUCTION

The rocket-triggered lightning technique, usually performed by launching a rocket dragging a copper wire, is an effective way to better understand the lightning physics and effects (e.g., [1]-[2]). The trajectory of the copper wire is characterized by a noticeable luminous-and-grounded channel above the ground [3]. Considering e triggering wire as a grounded tall structure, the phenomenology of rocket-triggered lightning is to some extent similar to a natural upward lightning flash.

Following the procedure presented in [4], the classical guided-wave M-component model from [5] was extended to take into account the presence of a tall tower in [6]. Compared to return strokes, M-components exhibit noticeable differences in terms of their current peak, their rise-time and the associated E-field waveforms.

II. RESULTS AND ANALYSIS

As shown in Fig.1, the computed electric field waveshapes at 100 m considering various heights of the luminous and grounded channel are significantly different in their initial negative part. As shown in Fig.2, the fields are significantly affected by reflections in the channel and the effect of the first reflection seen to be dominant over rest of the multiple reflections. One reflection represents the scenario that reflected current wave from the ground will directly go ahead along the channel with any reflections at the top of the luminous channel.

III. CONCLUSIONS

The presence of the luminous-and-grounded channel plays an important role in the wave shapes of the M-component electric fields at close distance. In addition, the study shows that reflections in the luminous-and-grounded channel lead to a smaller amplitude of the initial negative peak and the first of the multiple reflection plays a dominant role in this effect.

Financial supports from the NSF of China under Grant 51921005.

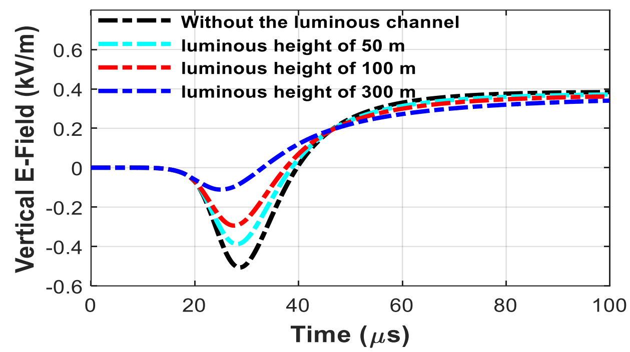

Figure 1. Electric fields of M-component mode of charge transfer at 100 m.

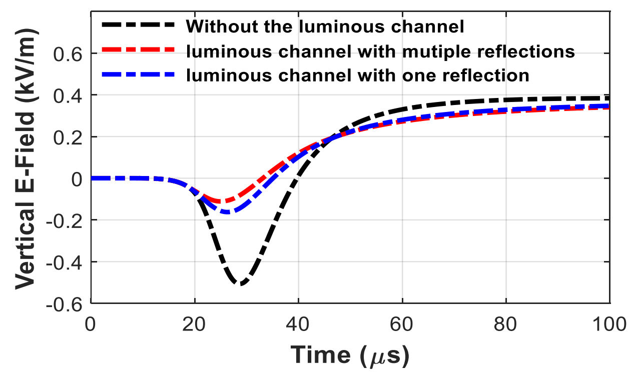

Figure 2. Influences of reflections inside the luminous-and-grounded channel on the electric fields of M-component mode of charge transfer (300 m distance).

REFERENCES

[1] Rubinstein, M., et al., Characterization of vertical electric fields 500 m and 30 m from triggered lightning. J. Geophys. Res., 100(D5), 8863–8872. 1995.
[2] Wang, J., et al., Multiple-Station measurements of a return-stroke electric field from rocket-triggered lightning at distances of 68–126 km, IEEE Trans. Electromagn. Compat, vol. 51(2), pp. 440-448, 2019.
[3] Winn, W. P., et al., Luminous pulses during triggered lightning, J. Geophys. Res., 117, D10204, 2012.
[4] Rachidi, F., et al., Effect of vertically extended strike object on the distribution of current along the lightning, channel, J. Geophys. Res., 107(D23), 4699, 2002.
[5] Rakov, V. A., et al., Mechanism of the lightning M-component. J. Geophys. Res., 100, 25, 701–25, 710, 1995.
[6] Li, Q., et al., An extension of the guided wave M-component model taking into account the presence of a tall strike object. J. Geophys. Res., 126, pp.1-15, 2021.

HPEM testing of critical systems using IEC recommendations at DERC

Nicolas Mora, Felix Vega, and Chaouki Kasmi
Directed Energy Research Center, Technology Innovation Institute, Abu Dhabi, United Arab Emirates
nicolas.mora@tii.ae

***Abstract*—This paper reviews the assessment techniques of the vulnerability of critical systems against IEMI according to the IEC 61000-4-36. To quantify their impact, the IEMI environments must be characterized, the susceptible components and subsystems should be identified, and the expected disturbances must be evaluated. We introduce several transportable sources at the HPEM laboratory of DERC**.

Keywords: HPEM testing, immunity testing

I. INTRODUCTION

Given its importance to society, international organizations and procurement agencies constantly assess the protection of military and civil infrastructures. The global HPEM risks of critical infrastructures are unclear, and at the moment, no normative standards enforce systems' safety qualifications against IEMI. However, important advances have been made in the last decades in the generation of recommendations and standards for testing the immunity of electronic systems and designing general protection strategies. The subcommittee SC77C of IEC has dedicated since 1992 lots of efforts to provide recommendations and protection guidelines for HEMP and, more recently, for HPEM and IEMI [1].

The recommendation IEC 61000-4-36 [2] can be used to define the test level conditions for the assessment of the immunity of equipment and systems. The strategy considers several sources that have been classified according to their far-voltage, band ratio, and other criteria like the required technical preparation of the attacker and the deployment scenarios. The current protection level due to the location of the equipment is evaluated based on previous studies of building attenuation.

II. HPEM testing capabilities at DERC

Figure 1 illustrates the HPEM sources under investigation at the Directed Energy Research Center of the Technology Innovation Institute. A state-of-the-art laboratory with exemplars of transportable HPEM sources, including hyperband, mesoband, and hypoband devices, is being used to test equipment according to the IEC recommendation.

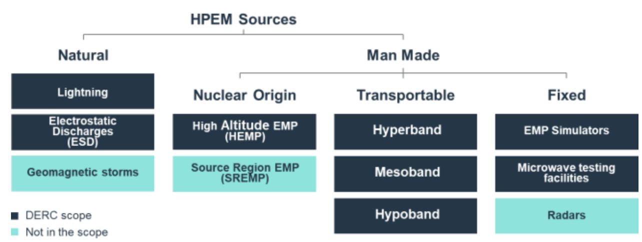

Figure 1. HPEM sources considered in the DERC roadmap

Figure 2 illustrates the EM environment of three types of sources available in the DERC lab.

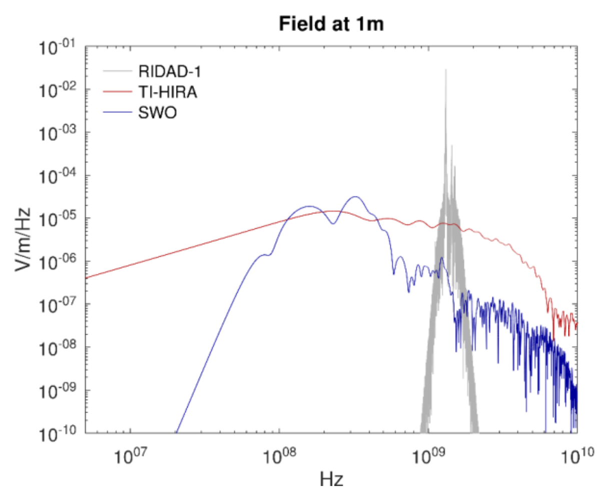

Figure 2. Examples of Hyper/Meso/Hypoband HPEM testing environments at DERC

REFERENCES

[1] W. Radasky, R. Hoad, "Recent Developments in High Power EM (HPEM) Standards With Emphasis on High Altitude Electromagnetic Pulse (HEMP) and Intentional Electromagnetic Interference (IEMI)," Letters on Electromagnetic Compatibility Practice and Applications, Vol. 2, No. 3, September 2020, pp. 62-66.

[2] IEC, "61000-4-36: Electromagnetic compatibility (EMC) –Part 4-36: Testing and measurement techniques – IEMI immunity test methods for equipment and systems," ed 2: IEC, 2020.

On the use of Convolutional Neural Networks to Classify Objects in GPR Scans

S. Abughazal[1], J. Pantoja[2], E. Almansoori[2], A. Almesmari[2], F. Vega[2], and C. Kasmi[2]

(1) Computer Vision, MBZUAI. Abu Dhabi, UAE

(2) Directed Energy Research Centre, TII. Abu Dhabi, UAE

sultan.abughazal@mbzuai.ac.ae

Abstract—This paper presents the experimental validation of a CNN architecture for the classification of buried objects scanned using Ground Penetrating Radar (GPR) scans. Moreover, it introduces a dataset called DERCGPR consisting of 200 GPR scans of 7 buried objects.

Keywords-GPR; CNN; Neural Network; Classification

I. INTRODUCTION

Ground Penetrating Radar (GPR) scans are commonly used to inspect shallow underground objects as a cost-effective, and non-destructive method of prospection [1]. Current applications of this technology require trained specialists to interpret GPR scans and identify buried objects. This leads to a time-consuming and costly process [2]. Section II of this paper summaries the process of data collection and post processing, while Section III shows the preliminary results.

II. METHOD

A. *GPR Data Collection and Postprocessing*

To collect the data, the GPR was installed on a 2-axis positioning system. Seven different objects buried underneath dry sand at depths between 5cm and 15cm were scanned. The hardware consisted of a NanoVNA connected to two Vivaldi antennas placed at 30cm above the surface. The VNA was set to emit a signal with frequency content between 700MHz and 3GHz every 1cm.

For every run, the A-scans were stacked to form the 2-dimentional B-scans on which the inverse fast Fourier transformation was applied row-wise (constant depth) using the PyTorch library. The real and imaginary parts of the result were summed and normalized across the whole dataset to preserve the small differences in signals reflecting from different materials. Finally, the row-wise mean was subtracted from every B-scan and negative values are eliminated by taking the absolute values.

B. *Neural Network Architecture*

The designed neural network begins with two convolutional layers, each one followed by one ReLU activation layer, see Figure 1 for reference. Only one average pooling step was added after the first convolutional layer. Following those feature extraction layers, two linear layers with sizes 400, and 100, respectively, were added as the classifier. For verification, the architecture was trained to classify GPR scans of 7 different classes of buried objects, leveraging every detail available in the acquired scans. A proprietary dataset of 1,390 training and 610 evaluation scans was used to train and test the devised model.

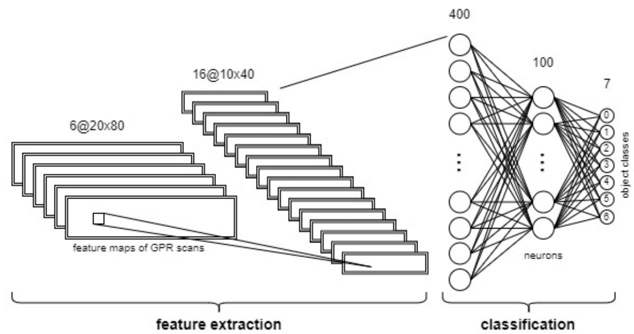

Figure 1: a diagram of the devised architecture for the classification task, showing the different types and sizes of layers.

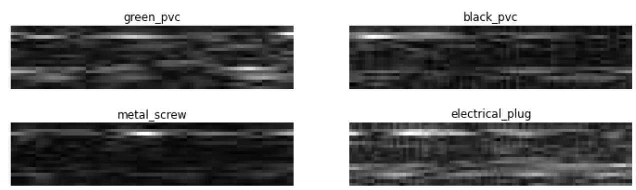

Figure 2: B-scans of different objects after applying inverse discrete Fourier transform, normalization and standardization.

III. CONCLUSION

The resulting GPR scans, shown in Fig. 2, are rich in information representing the different buried materials. It is unclear to the untrained eye what objects those scans represent. Meanwhile, a neural network can extract intricate features that are used to identify and classify the buried objects. The obtained performance in classifying GPR scans is quiet promising. Training a neural network to perform this classification task is potentially both a time and a cost saving approach. In the future, the built model would greatly benefit from more training examples and increased detail in the collected GPR measurements.

REFERENCES

[1] R. Parrillo and R. Roberts, "Bridge Deck Condition Assessment using Ground Penetrating Radar," January 2005.

[2] U. Ozkaya, F. Melgani, M. Bejiga, U. Özkaya and M. Donelli, "GPR B Scan Image Analysis with Deep Learning Methods," Measurement, vol. 165, p. 107770, March 2020.

Technology Innovation Institute
P.O Box 9639, Masdar City
Abu Dhabi, United Arab Emirates

tii.ae